

# UC San Diego

## UC San Diego Electronic Theses and Dissertations

**Title**

Oxygen transfer in the implant environment

**Permalink**

<https://escholarship.org/uc/item/77q112zw>

**Author**

Goor, Jared Braden

**Publication Date**

2007

Peer reviewed|Thesis/dissertation

UNIVERSITY OF CALIFORNIA, SAN DIEGO

## **Oxygen Transfer in the Implant Environment**

A dissertation submitted in partial satisfaction of the  
requirements for the degree Doctor of Philosophy

in

Bioengineering

by

Jared Braden Goor

Committee in charge:

Professor David A. Gough, Chair  
Professor Sungho Jin  
Professor Paul C. Johnson  
Professor Henry Powell  
Professor Geert Schmid-Schönbein

2007

Copyright

Jared Braden Goor, 2007

All rights reserved.

The dissertation of Jared Braden Goor is approved, and it is acceptable in quality and form for publication on microfilm:

---

---

---

---

---

Chair

University of California, San Diego

2007

For Joy, my family, and the lifelong friends I have made at UCSD

“When you do a demonstration, don’t use the word “because” but “so” instead. In other words, don’t start with the consequence to find the cause, but start from the cause to find the consequence.”

*-Michel Gondry, Director.*

“Good science requires identifying and limiting variables.”

*-S.M.J.*

## TABLE OF CONTENTS

<b>Signature Page</b>	.....	<b>iii</b>
<b>Dedication Page</b>	.....	<b>iv</b>
<b>Epigraph</b>	.....	<b>v</b>
<b>Table of Contents</b>	.....	<b>vi</b>
<b>List of Figures</b>	.....	<b>ix</b>
<b>List of Tables</b>	.....	<b>xii</b>
<b>List of Abbreviations</b>	.....	<b>xiii</b>
<b>Acknowledgements</b>	.....	<b>xv</b>
<b>Vita</b>	.....	<b>xviii</b>
<b>Abstract of the Dissertation</b>	.....	<b>xx</b>
<b>CHAPTER 1: Introduction</b>	.....	<b>1</b>
1.1	Relevance of the Dissertation .....	1
1.2	Oxygen Biosensors .....	2
1.3	Biomaterials and the Foreign Body Response .....	4
1.4	Humorals Markers of Inflammation .....	8
1.5	The Subcutaneous Environment and Window Chamber .....	9
1.6	Histological Techniques, Quantification .....	10
1.7	Scope of the Dissertation .....	11
1.8	Chapter Summaries .....	12
<b>CHAPTER 2: Biomaterials and Sensor Steady State Performance</b>	.....	<b>14</b>

2.1	Abstract.....	14
2.2	Introduction .....	15
2.3	Materials and Methods.....	15
2.4	Results and Discussion .....	26
2.5	Conclusion .....	41
<b>CHAPTER 3: Effects of Implantation on Sensor Performance .....</b>		<b>42</b>
3.1	Abstract.....	42
3.2	Introduction .....	42
3.3	Materials and Methods.....	43
3.4	Results.....	44
3.5	Conclusion .....	48
<b>CHAPTER 4: Biomaterials and the Sensor Dynamic Response to Single Oxygen Shifts .....</b>		<b>49</b>
4.1	Abstract.....	49
4.2	Introduction .....	50
4.3	Materials and Methods.....	51
4.4	Results and Discussion .....	55
4.5	Conclusion .....	70
<b>CHAPTER 5: Biomaterials and the Response to Hypoxia and Oxygen Challenges .....</b>		<b>72</b>
5.1	Abstract.....	72
5.2	Introduction .....	73
5.3	Materials and Methods.....	73
5.4	Results and Discussion .....	77
5.5	Conclusion .....	86
<b>CHAPTER 6: Quantitative Histological Analysis of Subcutaneous Tissue from Biomaterial Implantations.....</b>		<b>88</b>
6.1	Abstract.....	88
6.2	Introduction .....	89
6.3	Materials and Methods.....	90
6.4	Results.....	98
6.5	Conclusion .....	117

<b>CHAPTER 7: Quantitative Biocompatibility: Acute Phase Response Protein Assays in Rodent Models.....</b>	<b>119</b>
7.1 Abstract.....	119
7.2 Introduction .....	119
7.3 Materials and Methods.....	121
7.4 Results and Discussion .....	125
7.5 Conclusions .....	132
<b>CHAPTER 8: Conclusions of the Dissertation.....</b>	<b>133</b>
8.1 Conclusions .....	133
8.2 Future Directions.....	136
<b>APPENDIX A:Step Shift Curve Form Derivation .....</b>	<b>137</b>
<b>APPENDIX B: Time Constants from Discretely Sampled and Incomplete Curves, Application to Algorithms .....</b>	<b>139</b>
<b>APPENDIX C: 2-Dimensional Oxygen Diffusion Model of the Subcutaneous Tissue Surrounding a Sensor Array.....</b>	<b>143</b>
<b>APPENDIX D: Matlab and Mathematica Code for the Dissertation .....</b>	<b>154</b>
<b>REFERENCES .....</b>	<b>155</b>

## LIST OF FIGURES

<b>Figure 2.1</b> Design of the Planar Oxygen Sensor Array .....	16
<b>Figure 2.2</b> Design of the Sensor-Potentiostat Breakout Box .....	17
<b>Figure 2.3</b> The Sensor Signal Acquisition Pathway .....	19
<b>Figure 2.4</b> Membrane Encased Sensor Array .....	21
<b>Figure 2.5</b> Scanning Electron Images of the PDMS Membrane .....	21
<b>Figure 2.6</b> Window Chamber Assembly with a Mounted Sensor Array <sup>(84)</sup> ..	23
<b>Figure 2.7</b> Cross Section of a Dual Biomaterial Membrane (40x) .....	27
<b>Figure 2.8</b> Pre-Calibration of a Bare Sensor Array .....	28
<b>Figure 2.9</b> <i>In Vivo</i> Sensor Acquisition During Two Cycles of Oxygen Challenges.....	29
<b>Figure 2.10</b> Effect of Biomaterial Encapsulation on Baseline Sensor Signal Magnitudes .....	31
<b>Figure 2.11</b> The Gap Between PDMS and Cellulose Encased Sensor Signal Magnitudes at Baseline and Hypoxic Oxygen Levels, Days 7 and 14.....	32
<b>Figure 2.12</b> Effects of Biomaterials on Signals Normalized by Early <i>In-Vivo</i> Values .....	34
<b>Figure 2.13</b> Comparing Noise for Sensors Encased in Different Biomaterials at Baseline.....	36
<b>Figure 2.14</b> Noise During Hypoxic Challenges .....	37
<b>Figure 2.15</b> Slope of the Sensor Response to Oxygen: Sensitivity .....	39
<b>Figure 3.1</b> Comparing Pre-Implantation and Post-Explantation Array Calibrations.....	45
<b>Figure 4.1</b> Sensor Signals During an <i>In Vivo</i> Oxygen Challenge.....	56

<b>Figure 4.2</b> Comparing Raw Data and Fit Curves.....	57
<b>Figure 4.3</b> Delay in the Sensor Response and Vascular Proximity .....	59
<b>Figure 4.4</b> Time Constants and Vascular Proximity .....	60
<b>Figure 4.5</b> The Shift-Directional Ratio and Vascular Proximity .....	62
<b>Figure 4.6</b> Time Constant Changes from Day 7 to Day 14 .....	63
<b>Figure 4.7</b> Biomaterials, Time Constants, and Vascular Proximity.....	65
<b>Figure 4.8</b> Time Constants and the Initial Signal Drop <i>In Vivo</i> .....	66
<b>Figure 4.9</b> Biomaterials and Transient Initial Signal Magnitude.....	67
<b>Figure 5.1</b> <i>In Vitro</i> Calibration of a Bare Sensor Array: 3 Cycles of Hypoxic Challenges.....	74
<b>Figure 5.2</b> <i>In Vivo</i> Acquisitions of 16 Oxygen Sensors: 2 Cycles of Hypoxic Challenges.....	75
<b>Figure 5.3</b> Signal Magnitudes for 3 Cycles of <i>In Vitro</i> Oxygen Challenges.....	78
<b>Figure 5.4</b> Normalized Signal Magnitudes for 2 Cycles of <i>In Vivo</i> Oxygen Challenges.....	81
<b>Figure 5.5</b> Time Constants for Three Cycles of <i>In Vitro</i> Oxygen Challenges.....	83
<b>Figure 5.6</b> Time Constants for Two Cycles of <i>In Vivo</i> Oxygen Challenges.....	85
<b>Figure 6.1</b> The HistoQuant User Interface: Isolating Collagen in Masson's Trichrome Stained Liver Images.....	94
<b>Figure 6.2</b> Spatial Map of RGB Pixel Values: Isolating Erythrocytes in Masson's Trichrome Stained Subcutaneous Tissue Images.....	95
<b>Figure 6.3</b> Pseudo-Color Images and Histograms of the RGB Color Channels: Isolating Mast Cells in Giemsa Stained Subcutaneous Tissue Images .....	96

<b>Figure 6.4</b> Conversion Matrix for NTSC Color Space .....	96
<b>Figure 6.5</b> Tissue Ingrowth into Cellulose Implanted in Hamster Subcutaneous Tissue .....	101
<b>Figure 6.6</b> Isolating Mast Cells in Giemsa Stained Subcutaneous Tissue Images .....	104
<b>Figure 6.7</b> Isolating General Cell Nuclei in H&E Stained Subcutaneous Tissue Images.....	106
<b>Figure 6.8</b> Separation of Adjoined Features.....	107
<b>Figure 6.9</b> Dilation of Nuclei to Define Cell Boundaries .....	108
<b>Figure 6.10</b> Isolating Muscle Fibers in H&E Stained Subcutaneous Tissue Images.....	109
<b>Figure 6.11</b> Isolating Muscle Fibers in Giemsa Stained Subcutaneous Tissue Images.....	110
<b>Figure 6.12</b> In Phase Chrominance of Masson's Trichrome Stained Subcutaneous Tissue .....	111
<b>Figure 6.13</b> Isolating Erythrocytes in Masson's Trichrome Stained Subcutaneous Tissue Images.....	112
<b>Figure 6.14</b> Isolating Endothelial Cells in CD-31 Labeled Tumor Images.....	114
<b>Figure 7.1</b> Rat C-Reactive Protein Following Implantation of Biomaterials.....	129
<b>Figure 7.2</b> Rat Haptoglobin Following Implantation of Biomaterials.....	130
<b>Figure 7.3</b> Hamster Haptoglobin Following Window Chamber and Biomaterial Implantation .....	131
<b>Figure B.1</b> Curve Fitting Error and Sampling Frequency.....	141
<b>Figure B.2</b> Time Constant Calculation and Sampling Frequency .....	142
<b>Figure C.1</b> The Oxygen Diffusion Model User Interface: Spatial Vascular Map .....	145

<b>Figure C.2</b> 2-Dimensional Tissue Oxygen Maps.....	148
<b>Figure C.3</b> Mesh Solution for a Spatial Vascular Map .....	150
<b>Figure C.4</b> Topographical Tissue Oxygenation Map: Profile of Oxygen at the Sensor .....	151

## LIST OF TABLES

<b>Table 4.1</b> Oxygen Diffusion Constants for the Array Environment .....	69
<b>Table 5.1</b> Changes in Signal Magnitude <i>In Vitro</i> Following Hypoxic Exposure.....	77
<b>Table 5.2</b> Changes in Signal Magnitude <i>In Vivo</i> Following Hypoxic Exposure.....	80
<b>Table 5.3</b> Changes in Signal Magnitude <i>In Vitro</i> Between Cycles of Oxygen Challenges.....	80
<b>Table 5.4</b> Changes in Time Constants <i>In Vivo</i> Between Cycles of Oxygen Challenges.....	84
<b>Table 6.1</b> Measured Distances in Subcutaneous Tissue Explanted from Hamster Window Chambers with Active Oxygen Sensor Arrays.....	100
<b>Table 6.2</b> Filtration Parameters for Isolating Specific Tissue Features in Digital Images of Histological Sections.....	102
<b>Table 7.1</b> Variation of Serum Measurements: Different Test Sites, Animal Populations .....	128

## LIST OF ABBREVIATIONS AND SPECIFIC TERMS

<b>Biomaterials</b>			
APTES	3-aminopropyltriethoxysilane	CTMS	Chlorotrimethylsilane, a liftoff agent
Exclusion Size	Size of the smallest object that cannot pass through a membrane	Liftoff Agent	Prevents adherence of a curing polymer (ex: PDMS)
Microporous	Pores of micron scale. Ex: 10 $\mu$ m exclusion size.	NC	Cellulose abbreviation
PDMS	Polydimethylsiloxane	PTFE	Polytetrafluoroethylene (Teflon)
Pores, Trabecular	Pores created by meshed fibers	TFE	Tetrafluoroethylene, used as an expansion coolant
WC	Window Chamber		
<b>Sensor Static Performance and Acquisitions</b>			
NI-DAQ	National Instruments Data Acquisition Card	Noise	Variance or deviation of the signal relative to the signal magnitude
Sensitivity of the Sensor	The relationship between signal magnitude and exogenous oxygen, generally linear	Signal Magnitude	Potentiostat output potential, representing the oxygen reduction current of the sensor
<b>Sensor Dynamic Performance</b>			
Challenge/ Oxygen Challenge	Step shift in exogenous oxygen.	Exposure/ Hypoxic Exposure	A drop and return in the concentration of exogenous oxygen
SDR/ Shift-Directional Ratio	Ratio of the time constant for an upward step shift over an equally sized downward shift.	$\tau$ c/ Time Constant	Exponential term modifier for a step shift in concentration $C = C_0 - \Delta C * e^{(-\tau c * \Delta t)}$ .
<b>Programming and Imaging</b>			
CCD	Charge-Coupled Device: Electronic light sensing unit used in digital cameras	Color Space	System of encoding color for electronics and computation.

DSLR/ Dual SLR	Digital Single-Lens Reflex camera: Uses two CCDs for concurrent imaging and viewfinding	HQ/HistoQuant	Histology Quantification Software (by author)
I or IPC	In Phase Chrominance (NTSC channel)	IHC	Immunohistochemistry
Luminance	Grayscale NTSC channel	Q or QC	Quadrature Chrominance (NTSC channel)
RGB	RGB color space. Three 8-bit channels: Red (R), Green (G), Blue (B)	Y I Q	NTSC color channels, Y is luminance
<b>Serum Proteins</b>			
APR and APRPs	Acute Phase Response, APR Proteins	CRP	C-Reactive Protein
Hp	Haptoglobin		
<b>Oxygen Diffusion</b>			
$\alpha$	Solubility of a gas	Diffusion Equation	Equation C.1
DO <sub>2</sub>	Diffusion constant	$m$	Rate of consumption
PO <sub>2</sub>	Oxygen Tension/ Partial Pressure		

## ACKNOWLEDGEMENTS

I would not have made it through this without Joy and my family, old and new.

I'd like to thank my advisor Dr. Gough for encouraging me through a complex and fascinating project and my Committee for valuable feedback and philosophy.

I'd also like to thank a few faculty who have made extra time and energy for me.

- Dr. Peter Chen for mentorship and for fostering my proficiency in optics and interest in the microvasculature.
- Dr. Amy Tsai for continuous input and support.
- Dr. Andrew Mizisin for philosophical and practical advice on histology.

Several UCSD staff and professionals have also been also crucial to my success.

- Milan Makale for training in animal handling, surgery and sensor implantation.
- Isgard Hueck for establishing our histology protocols and managing the lab.
- Allen Barra and Cynthia Walser for invaluable window chamber technique.
- Ryan Anderson for training in photolithography and for being dedicated to his job.
- Barbara Schumacher for cryostat training and valuable feedback in cryosectioning.
- Joe Lin for his help with the biosensor design, aid at all stages of sensor use, and for taking the time to always give me the whole picture.
- Glysens for building the oxygen sensors and potentiostat.
- Rick Calou for his solidworks models.

- UCSD's Animal Care staff: Thanks to Lisa, Steve, and Mel in particular.
- Irene, Jeff, Christine, and my friends in the front offices.

I'd like to thank several graduate students, for lessons learned and time wasted.

- Nick Rahaghi for pushing the flow project, starting up the histological analysis programming project, and many, many nights of philosophical conversations.
- Lee Pang for aid in photolithography, microscopy, programming, and simple solutions to scientific and personal dilemmas.
- Edward Pang for constant support including invaluable beta testing of the HistoQuant programs.
- Lucas Kumosa for biomaterial micro-featuring, and for getting the dynamics portion of the sensor analysis off the ground.
- Scott Anderson for his Labview program with which all sensor data is acquired.
- Alex Hsaio for a summer of working on the diffusion modeling program.
- Chris Grilly for sharing equipment and checking in.
- Jane Frimodig, Shayda Moshirvaziri, and Adam Strobl. Go Biosensors.

I have also had the pleasure of interacting with many bright students and volunteers who always made a project go smoother.

- Jeremy Beer, Michael Lau, and Andrew Jang for the Sand Rat study as well as the rest of the Tortuosity project. To Michael and Andrew for the Histoquant project.
- Christine Lliang for being the calibration goddess and a patient trainer.
- Deepa Ravindrath for substantial help with the Acute Phase Proteins project.

- Jason Tongbai and Jon Kuo for help in electrical engineering and Cossacks.
- Lauren Westfall for histology and hamster handling.
- Patrick Giuliano for data mining and checking the animals so many times.
- Krystle Shoates for many, many calibrations and implanted sensor acquisitions.

Lastly, I've made some of the best friends of my life at UCSD. In no particular order, I am lucky to have met Lee and Lisa, Pat and Valerie, Chris and Devon, Joey, Joann and Francisco, Chris and Sarah, Pete and Karen, Susan, Alex, Ian, Ramses, and Jeff.

An online electronic lab notebook was provided for me by [E-nnovate.com](http://E-nnovate.com) saving me tremendous time and effort.

Figure 2.6 is a partial reprint from: Makale MT, Chen PC, and Gough DA. Variants of the tissue-sensor array window chamber. *Am J Physiol Heart Circ Physiol* 289: H57-65, 2005.

## VITA

2007	Ph.D., University of California, San Diego
2004	M.Sc., University of California, San Diego
2001	B.Sc. (Distinguished Honors) University of Virginia

## AWARDS

- 2005 UC Systemwide Bioengineering Symposium, Honorable Mention Poster
- 2004 UC Systemwide Bioengineering Symposium, "Best Poster" award
- 2004 Nominee for best abstract, 4<sup>th</sup> Diabetes Technology and Therapy Conference
- 2003 Nominee for best abstract, 3<sup>rd</sup> Diabetes Technology and Therapy Conference
- 2001 UVA Award for Excellence in Chemistry

## PUBLICATIONS

Makale MT and **Goor JB**, "A Window to Observe the Foreign Body Response Reaction to Glucose Sensors", Chapter from In Vivo Glucose Sensing edited by David Cunningham and Julie Stenken, John Wiley & Sons, Inc., Hoboken, NJ. In Publication.

## SELECTED ABSTRACTS AND PRESENTATIONS

**Goor JB** and Rahaghi FN, Makale MT, Gough DA, "Factors that confound the tissue glucose sensor response" Diabetes Technol Thep, San Francisco, CA 2005.

Makale MT, Lin JT, Chenault VM, Beer JB, Rahaghi FN, **Goor JB**, Gough DG, "Glucose Sensor Arrays in the Diabetic Sand Rat" Diabetes Technol Thep, San Francisco, CA 2005.

**Goor JB**, Rahaghi FN, Makale MT, Chen PC, Gough DA, "Study of Local Physiological Factors That Modify the Sensitivity of Implanted Tissue Glucose Sensors" Diabetes Technol Thep, San Francisco, CA 2004.

**Goor JB**, Rahaghi FN, Makale MT, Chen PC, Gough DA, "Indices and Endpoints for the Determination of Sensor Biocompatibility" 3rd Glucose Monitoring and Control Conference, La Jolla, CA 2004.

**Goor JB**, Rahaghi FN, Makale MT, Chen PC, Gough DA, "Window Chamber for the Study of Tissue Glucose Sensors" Diabetes Technol Thep, San Francisco, CA 2003.

**Goor JB**, Rahaghi FN, Harris TJ, Makale MT, Chen PC, Gough DA, “Impanted Oxygen Sensors and the Skinfold Window Chamber” 2nd Annual California Tissue Engineering Meeting, La Jolla, CA 2003.

### **TECHNICAL ACKNOWLEDGEMENTS**

Milan T. Makale, Peter C. Chen, and David A. Gough, *Variants of the tissue-sensor array window chamber*, Am J Physiol Heart Circ Physiol 289: H57-H65, 2005. Dissertation author provided experimental data, animal handling, and figures.

### **FIELDS OF STUDY**

2002-2007	Biosensors and Biomaterials under Dr. David Gough
2000-2001	Neurodegenerative Disease Origins under Dr. Patricia Trimmer

# **ABSTRACT OF THE DISSERTATION**

## **OXYGEN TRANSFER IN THE IMPLANT ENVIRONMENT**

by

Jared Braden Goor

Doctor of Philosophy in Bioengineering

University of California, San Diego, 2007

Professor David A Gough, Chair

Oxygen mass transfer in the subcutaneous tissue environment was studied using implanted oxygen sensors and quantitative histology. The impact of biomaterials on mass transfer was also observed through analysis of materials encased sensor performance and measurement of serum proteins. Dynamic sensor challenges were used to gain insight into the oxygen stasis mechanisms of subcutaneous tissue and to estimate diffusion of oxygen through the tissue and biomaterials.

Five hamsters were implanted with planar arrays consisting of 16 symmetrically distributed oxygen sensors. Each array was half encased by smooth PDMS and half by a microporous cellulose membrane. The sensor signals were measured over 14 days, including two sessions of hypoxic challenges. Steady state sensor signals normalized to pre-surgical calibrations demonstrated elevated signal magnitudes for PDMS encased

sensors, significant for the first 7 days ( $P < 0.015$ ). Noise levels for PDMS encased sensors were observed to be lower except during hypoxia when the trend was reversed. At the hypoxic levels observed, sensitivity of the sensors to oxygen remained linear.

*In vitro* and *in vivo*, cellulose encased sensors had smaller time constants, a measure of the sensor's ability to respond to change. However, time constants were more strongly dependent *in vivo* on the proximity of vasculature to the sensor, observed to be closer in tissues adjacent to cellulose. Comparison of the time constants for oxygen increases versus decreases demonstrated a tissue resistance to oxygen loss inversely dependent on tissue volume and thus likely vascular in origin. Diffusivity for the array environments was  $1.91 \pm 0.86 \times 10^{-5} \text{ cm}^2/\text{s}$  on average, with greater diffusion resistance in the cellulose membranes. *In vivo*, loss of sensor signal magnitude and gain in time constants following hypoxic challenge was independent of biomaterials, but dependent on the tissue response to the implant.

A method of analyzing digital images of histological sections using color and morphological filters was refined for the quantification and spatial mapping of specific tissue features with potential effect on oxygen diffusion. Haptoglobin measurements over 7 days following biomaterials implantation in hamsters showed that microporous polytetrafluoroethylene and cellulose in window chambers elicited elevated responses versus a control and versus a window chamber only implantation.

# **CHAPTER 1: Introduction**

## **1.1 Relevance of the Dissertation**

### **1.1.1 Need for Study of Tissue Mass Transfer**

Mass transfer is a crucial factor in tissue survival and metabolic processes, and for a growing number of implanted devices, it is required for device function. Devices such as encapsulated beta cells<sup>(26, 45, 80)</sup>, drug delivery devices, and biosensors<sup>(19)</sup>, measure, depend on, or intervene in local metabolism. These devices offer a new paradigm in the monitoring and treatment of disease through active chemical exchange with the tissue. Thus, an understanding of how mass transfer impacts the performance of these devices is important to their design and application.

Oxygen is an ideal analyte for initial mass transfer studies. It is a crucial tissue metabolite with high diffusivity and is useful as a co-analyte for the measurement of other important metabolites like glucose and lactate<sup>(11, 50, 84)</sup>. The electrochemical measurement of oxygen with implanted biosensors is an established practice.

### **1.1.2 Overview of the Dissertation Research**

This study uses subcutaneously implanted oxygen sensor arrays in the hamster window chamber to observe oxygen diffusion characteristics of the tissue environment. The effects of smooth and microporous biomaterial membranes are observed on the sensor's steady state and dynamic performance, as well as sensor performance following hypoxic exposure. A process for quantifying and spatially mapping histological features of tissue that are relevant to oxygen transfer is established, and a method of assessing the inflammation response to biomaterials with acute phase response proteins is explored.

This introduction describes the background and science of oxygen sensor arrays, window chambers, the foreign body response to micro-featured biomaterials, and oxygen diffusion in tissue. The goals of the dissertation are then asserted along with a brief discussion of the topics of study for each chapter.

## **1.2 Oxygen Biosensors**

### **1.2.1 Electrochemical Oxygen Sensors**

The electrochemical oxygen biosensors used in this dissertation employ a highly stable three electrode design<sup>(9, 81)</sup>. In this design, the three electrodes are connected to a potentiostat, an instrument that enforces a fixed 500mV potential between two of the electrodes, the platinum working electrode and the silver chloride reference, with the working electrode cathodic. The potential drives the reduction of oxygen on the working electrode but does not invite oxidation of interfering species such as peroxides<sup>(81)</sup>. The outer hydrophobic membrane also prevents access of other reducible, polar compounds to the electrode surface and reduces the effects of flow or motion in the external media. Oxygen reduction creates a current that passes through a conductive hydrogel medium - confined between the electrode surfaces and hydrophobic membrane- which current passes from the working to the counter electrode for measurement and amplification by the potentiostat. The current is amplified and converted by the potentiostat to a potential, referred to as the sensor signal. When transfer of oxygen to the sensor is limited by diffusion through the surrounding medium, the sensor signal is proportional to the local oxygen concentration. Signal acquisition is described in the Chapter 2 methods and diagrammed in Figure 2.3.

### 1.2.2 The Planar Oxygen Sensor Array

The planar sensor array design has been described previously<sup>(85, 86)</sup>. In brief, the array houses up to 18 electrochemical oxygen sensors distributed evenly over a circular ceramic face (Figure 2.1A). Working electrodes 125 $\mu$ m in diameter are segregated into four separate quadrants of the ceramic face, each with a single reference electrode. A sinuous counter electrode passes around the sensor, evenly separating each reference electrodes from its respective working electrodes. The electrode wires pass through the ceramic face to the rear, and run along a ceramic or plastic rectangular backing. Gold plating on the ends of the wires connects the array to a multi-channel potentiostat.

### 1.2.3 Sensor Arrays for Biomaterials Studies

The dissertation uses the sensor array described above with two modifications, a symmetric arrangement of sensors, and a secondary biomaterial membrane. For each array, two working sensors along the vertical midline are left inactive, and the remaining 16 are segregated into two symmetrical groups of 8 working sensors, one group on each side of the array (Figure 2.1A) with one counter and two reference electrodes per group. Each group of sensors will be encased in one of two different biomaterial membranes previously observed to elicit different responses from the tissue when implanted. The sensors are spaced such that the oxygen that reaches them will have passed through their respective biomaterial membrane directly from the tissue environment.

In this dissertation, implanted biomaterials encased sensor arrays and histology are used to determine differences in oxygen transfer to the sensors and in the tissue adjacent to the biomaterials, and to examine potential connections.

Subcutaneous tissue composition and vascular distribution at the millimeter scale is heterogenous<sup>(34, 57, 84, 130)</sup>. Taking measurements in multiple locations then allows the array to partially circumvent this heterogeneity. Studying the effects of two membranes

in one animal reduces the error introduced by the often significant variation between animal physiologies. Thus the biomaterial encased array both increases the number of experimental samples and improves control.

### **1.2.4 Implanted Sensor Performance**

Individual sensors *in vitro* have strong signals with fast, clean responses to changes in oxygen concentration. It has also been shown that differences in *in vitro* performance of the sensor per se before implantation and after explantation are statistically not significant, and that mass transfer resistance of the sensor's hydrophobic membrane are negligible compared to that of the tissue<sup>(85)</sup>. Thus, *in vivo*, the sensor's performance reflects the resistance to oxygen mass transfer of the biomaterial encasing and the tissue.

The sensor's steady state performance is defined by its signal magnitude, the measure of oxygen flux to the sensor. The sensor's dynamic performance involves its rate of response or signal delay after a change in oxygen. These characteristics reflect both the mean diffusional distance and the diffusion coefficient in the tissue.

## **1.3 Biomaterials and the Foreign Body Response**

### **1.3.1 The Tissue Response to Biomaterials**

#### **1.3.1.1 General Response and Inflammatory Cells**

Implantation of devices and materials subcutaneously elicits a foreign body response. Proteins adsorb to the material surface, followed by the recruitment and adherence of local and circulating cells<sup>(43, 105)</sup>. Local and recruited mast cells, critical effectors of inflammation, produce and release granules consisting of histamine, heparin, cytokines, and other chemicals as part of the local and vascular inflammation response<sup>(43,</sup>

<sup>92, 111</sup>). Inflammation of the tissue can cause vascular changes which increases the numbers of monocytes and other white blood cells<sup>(7, 43, 88)</sup>. Local and recruited phagocytic cells, notably macrophages, may attempt to break down and engulf the object, forming multinucleated giant cells and releasing degradative and other signaling agents when these attempts are not successful<sup>(6, 7)</sup>.

### **1.3.1.2 Formation of the Fibrous Capsule**

In the tissue, meshlike deposits of proteins such as fibrin encourage the proliferation and migration of several repair cells, notably fibroblasts and endothelial cells<sup>(43)</sup>. These cells begin depositing the loose connective tissue that will form the new tissue structure and be replaced during the remodeling phase of the response. Especially with increased inflammation<sup>(135)</sup>, mesh-like collagen III is deposited in far greater proportions than are found in normal tissue, for later replacement by tighter, more oriented collagen I.

The layer of cells, proteins, and fibers that forms around the implant, frequently referred to as the fibrous capsule, may impose resistance to oxygen mass transfer. Reducing or guiding non-specific protein adhesion and capsule formation has been the focus of much of biomaterials research<sup>(31, 104)</sup>. However, there has been limited research into the effect of the fibrous capsule on tissue diffusion<sup>(121, 140-142)</sup>.

### **1.3.2 Timeline of the Tissue Response**

The experiments in this dissertation haven been carried out over two weeks, which coincides with the peak of neovascularization, and active phagocytic cell recruitment and invasion<sup>(43)</sup>. Neovascularization in tissues implanted with microporous membranes has been observed by Padera to peak within 10-21 days following microporous biomaterial implantation<sup>(97)</sup>. With regard to cell recruitment, the invasion of neutrophils is expected to have been completed by two weeks, while active macrophages

and mast cells are expected to remain<sup>(13, 89)</sup>, continuing to affect tissue inflammation<sup>(44, 87)</sup>. Padera also observed cell invasion of micropores to peak between 7-21 days. Deposition of type III collagen and other fibers by migrating fibroblasts are expected to be in progress during this period<sup>(61, 135)</sup>, but remodeling of tissue may have only begun.

### **1.3.3 The Effects of Tissue Response on Oxygen Transfer**

The changes in tissue that affect oxygen mass transfer fall into two categories, factors that impact convective transfer and those that impact diffusive transfer.

Inflammation and its effect on vascular perfusion and leakiness can affect convection in the blood. Convection may also be affected by flow redistribution, the restructuring of existing vasculature, and development of new vasculature.

Development of the fibrous capsule and tissue growth can affect the impact of convection by changing the diffusional distance. Oxygen flux through the tissue is also affected by the solubility of the tissue to oxygen and the metabolic consumption of oxygen in the tissue.

### **1.3.4 Hypoxia and the Tissue Response: What is Not Covered**

Hypoxia is known to drive and modulate many components of the foreign body response, including phagocyte metabolism<sup>(29)</sup> and migration<sup>(10)</sup>, and vascular leakiness<sup>(78)</sup> and tortuosity<sup>(32, 77)</sup>. While hypoxia and oxygen levels in the tissue may greatly influence wound healing, this dissertation will not focus on the role of sensors in modulating tissue oxygenation. Smaller electrodes which consume less oxygen were chosen for these experiments to minimize the impact as much as possible without sacrificing signal sensitivity.

### 1.3.5 *In Vivo* Diffusion Studies

To date, a few careful studies of diffusion in the tissue have been carried out in an effort to understand how the encapsulation of biomaterials and the development of new tissue affect diffusion.

Sharkawy placed capsular tissues in dual-chambers and separately injected dyes into rats having different biomaterial implants, followed by timed explantation and cryo-sectioning of the tissue surrounding the implants<sup>(121-123)</sup>. These experiments allowed estimation of diffusion constants, vascular density and permeability, and response rates for different tissue structures surrounding smooth and porous implants, and found all were improved in tissues adjacent to microporous biomaterials. Wisniewski demonstrated that for subcutaneously implanted hollow poly(ether sulfone) and other microdialysis fibers, there was a significant effect of protein and cellular adsorption on glucose diffusion, though the effect was observed to be 3-5 times smaller than the diffusive resistance of the tissue<sup>(140)</sup>. Researchers have also studied the effects of encapsulation on the diffusion of antibiotics and other drugs from implanted polymer delivery devices, finding that encapsulation can significantly retard drug release from an implant<sup>(8, 17, 113, 114)</sup>.

These studies demonstrated that biomaterials, the foreign body response, and encapsulation may affect diffusion in the tissue environment.

### 1.3.6 Micro-Featuring and Oxygen Transfer

Micro-features have been shown to alter the orientation, kinetics, and metabolism of cells *in vitro*, a phenomena known as contact guidance<sup>(30, 33, 93, 117, 143)</sup>. *In vivo*, micro-features<sup>(13, 31)</sup> and trabecular micro-pores<sup>(19, 67, 68, 97, 136, 139)</sup>, have been observed to reduce the thickness of the fibrous capsule, reduce the formation of giant cells, alter collagen deposition, and to encourage tissue integration and neovascularization. Thus, the

application of micro-featured or microporous membranes are expected to alter the tissue in ways that should improve oxygen diffusion properties of the tissue.

This dissertation employs a smooth material, polydimethylsiloxane (PDMS), and a microporous biomaterial, cellulose, which have been previously observed to elicit structurally distinct tissue responses which may affect oxygen diffusion. These materials are easily available, workable, and well studied<sup>(14)</sup>. The micro-pore size of the membrane is 8 $\mu$ m, the pore size determined separately by Brauker and Padera to be optimal for neovascularization in the soft tissue<sup>(19, 97)</sup>, though smaller than the pore size implemented by Sharkawy.

This dissertation is part of a longer term goal to compare many polymers, including variations in micro-featuring and other surface modifications.

## **1.4 Humorals Markers of Inflammation**

As noted, biomaterials and the process of implanting them are known to elicit a systemic inflammation response. Inflammation causes fluid retention, changes in vascular perfusion and affects cellular recruitment<sup>(43)</sup>. The early stages of the response to the implant, the Acute Phase Response, includes elevation of a number of key blood serum proteins recruited from the liver and discussed at greater length in the introduction to Chapter 7. These acute phase response proteins (APRPs) may offer a unique method of quantifying the compatibility of biomaterials by correlation with the degree of inflammation they elicit.

## 1.5 The Subcutaneous Environment and Window Chamber

### 1.5.1 The Window Chamber: Hamster Skinfold Model

Transparent viewing windows for the study of subcutaneous tissues were originally developed for use in the rabbit ear<sup>(24, 36, 116)</sup>, for basic vascular study and the observation of tumor development. The chamber was adapted to the skinfold<sup>(138)</sup>, and then expanded to tumor and autologous transplantation studies in mice<sup>(3-5, 106)</sup>, and was later developed for the hamster<sup>(40)</sup>. The loose dorsal fold of the hamster proved an excellent medium for the study of microhemodynamics<sup>(18, 25, 65, 130)</sup>.

For the study of implanted biosensors, the hamster window chamber was modified, mounting a planar oxygen sensor array on one side of the dorsal fold and a glass viewing window on the opposite side<sup>(86)</sup>. The combination allows continuous nondestructive visualization of the tissue environment surrounding an active biosensor. This dissertation utilizes this modified hamster skinfold window chamber to mount the planar oxygen sensor array and the biomaterial membranes exposed to subcutaneous tissue.

The hamster window chamber preparation offers several advantages for *in vivo* biosensor studies. Besides the potential for visualization of the sensor environment, the chamber frame supports the tissue and reduces relative mechanical motion. This has the advantages of lessening potential non-biomaterials related inflammation and ensuring that the tissue and the biomaterial membrane of the sensor are in the same relative position for the duration the study. The consistent tissue-sensor spatial relationship improves confidence that changes in sensor performance are due to changes in the local tissue and makes it possible to correlate specific regions of explanted tissue histology to specific regions of the sensor array.

### **1.5.2 The Subcutaneous Environment**

The subcutaneous environment is frequently utilized as a location for sensors and other implanted devices, taking advantage of convenient fatty pockets. Implantation under the skin is less invasive and less risky than deeper or vascular implantations, and offers easier access for repeat surgeries or modifications. As well, the skin can easily be displaced without affecting gross function.

The hamster skinfold offers an excellent medium for biomaterials and biosensor studies. Window chamber surgeries can be used to easily and reproducibly expose dermal, fatty hypodermal, or muscular tissue. The reticular muscle of the hamster affords a manipulable muscular environment that is approximable to human skeletal muscle<sup>(62, 125)</sup>, and it is this environment on which the dissertation will focus.

## **1.6 Histological Techniques, Quantification**

Histological observations have long been a preferred method of analyzing the effects of biomaterials on tissue. High quality images of tissues offer a deeper understanding of their microscopic structure, and thus offer a basis of comparison between different interventions. In order to evaluate the effects of tissue structure and composition on diffusion, or to apply tissue observations to quantitative diffusion models, highly quantitative measurements of the histology are needed.

## 1.7 Scope of the Dissertation

Hypothesis: *Oxygen mass transfer to an implanted oxygen sensor is affected by the materials of the sensor membrane and their interaction with the tissue environment.*

- 1) Goal: To determine if biomaterials affect oxygen flux in the tissue environment.  
To determine if there are effects on
  - a. the magnitude and dynamics of oxygen flux,
  - b. magnitude and dynamics of oxygen flux following exposure to hypoxic challenges, and
  - c. the sensor itself
- 2) Goal: To determine if histological observations of the tissue adjacent to the sensor can be correlated to oxygen flux.
- 3) Goal: To establish methodology for digitizing histological images and quantitatively analyzing certain tissue features. To determine parameters for quantifying specific tissue features important to oxygen diffusion, including: microvessels, cell density, muscle fibers, collagen, and mast cells.
- 4) Goal: To determine the effects of implanted biomaterials and the implantation process on serum levels of certain acute phase response proteins.

## 1.8 Chapter Summaries

The chapters of the dissertation reflect the order of the dissertation goals. Each chapter is written in an article format.

In Chapter 2, the bulk of the experimental methods are described, with attention to the implementation of implanted oxygen sensor arrays, biomaterials, and animal subjects. This chapter focuses on the *in vivo* comparison of the signals for oxygen sensors encased in different biomaterials. Changes in signal magnitude and noise will be examined and compared to *in vitro* observations. Lastly, the curve of the *in vivo* sensor response to exogenous oxygen levels will be plotted and its form examined.

The oxygen sensitivity of sensor arrays are examined in Chapter 3, pre-implantation and post-explantation, to determine the effects, on the sensor itself, of implantation with different biomaterials.

In Chapter 4, the dynamics of implanted sensors in response to single shifts in inspired oxygen levels are observed, specifically the rate of response and delay in sensor response. The rate of response for increasing versus decreasing oxygen is compared. The relationship between sensor dynamics and sensor vascular access is observed, and the tissue oxygen diffusion constant is estimated. For each aspect of the study, the effects of the implanted biomaterials are compared.

Chapter 5 explores the response of implanted sensors to a series of oxygen challenges consisting of multiple shifts in exogenous oxygen concentration. The role of biomaterials and tissue on sensor signal magnitude and dynamics is analyzed.

In Chapter 6, a method of quantifying histological observations is established, with specific application to tissue features that are expected to affect tissue oxygen diffusion. A limited histological study of the tissue from the sensor-array-implanted animals is reported.

In Chapter 7, several biomaterials are compared in their effect on C-Reactive Protein and Haptoglobin serum concentrations following implantation. A novel quantitative serial blood collection method is described. Microporous materials and the window chamber itself are studied as potential sources of inflammation.

### **1.8.1 Appendices**

Appendix A describes the derivation of the curve fitting method used for analyzing sensor dynamics.

Appendix B describes a careful analysis of curve fitting and time constant calculation for incomplete and discretely samples signal curves. This section is intended for application to sensor control and predictive algorithms.

Appendix C is a model of oxygen diffusion in the subcutaneous tissue surrounding implanted sensors, using spatial maps of quantified histological features and several methods of solving the diffusion equation.

## CHAPTER 2: Biomaterials and Sensor Steady State Performance

### 2.1 Abstract

Five hamsters were implanted with planar arrays consisting of 16 symmetrically distributed oxygen sensors. Each array was half encased by smooth polymethyldisiloxane (PDMS) and half by a microporous cellulose membrane. The sensor signals were measured over 14 days, including two sessions of hypoxia. The calibrated sensor signals corresponded to initial oxygen partial pressures of 2.92%, increasing significantly by day 7. PDMS encased sensors had higher signal magnitudes than cellulose encased sensors during the first 7 days of implantation ( $P < 0.015$ ), indicating higher oxygen fluxes in these tissues. These differences were still observed after normalization for material diffusive resistance, and also after normalization for inherent differences in tissue structure, indicating that flux differences were due to the tissue response to the biomaterials.

Noise was determined by standard deviation of the steady state signal as a percent of signal magnitude. Average *in vivo* signal noise was  $1.73 \pm 2.19\%$  at 20.9% oxygen, 6.52% higher for sensors encased in cellulose than those in PDMS ( $P < 0.0075$ ). During hypoxia, all sensors' noise increased, and the noise of PDMS encased sensors surpassed that of cellulose encased sensors by 42.3%. This was in direct contrast to *in vitro* results, where cellulose encased sensors had greater noise regardless of exogenous oxygen.

A plot of sensor sensitivity to 10.0-20.9% exogenous oxygen was very linear *in vivo*, indicating that mass transfer to the sensor was diffusion limited and that hypoxia in this range did not affect the relationship between *in vivo* and exogenous oxygen.

## **2.2 Introduction**

This study examined the relationship between the tissue response to biomaterials and oxygen diffusion by employing an implanted planar oxygen sensor array consisting of 16 symmetrically distributed oxygen electrodes. Eight sensors on each side of the array were encased in two different adjacent biomaterial membranes to determine if the tissue response to the biomaterials would differentially affect oxygen transfer. Smooth, oxygen permeable PDMS and cellulose with an 8 $\mu$ m pore structure were chosen for this initial experimental series.

In this study, regular measurements of sensor magnitude were made during a 14 day implantation, comparing the output of sensors encased in each material. Additionally, the effect of the biomaterials on signal noise and the slope of sensor output versus inspired oxygen were observed.

## **2.3 Materials and Methods**

### **2.3.1 Preparation of the Sensor Arrays**

#### **2.3.1.1 Sensor Design and Modifications**

Four planar oxygen sensor arrays were acquired in dry state from Glysens (Sorrento Valley, CA). The basic design is described in Chapter 1 (Figure 2.1). Platinum working electrodes 125 $\mu$ m in diameter were chosen for this experiment to improve spatial sensitivity while providing sufficient signal amplification.

A breakout box for sensor connections to the potentiostat was designed specifically for this experiment. The circuitry connects each working electrode to its respective reference and counter electrode. Additionally, the box separates the 16 signals of the array into two sets of 8, corresponding to the biomaterial in which the sensors are

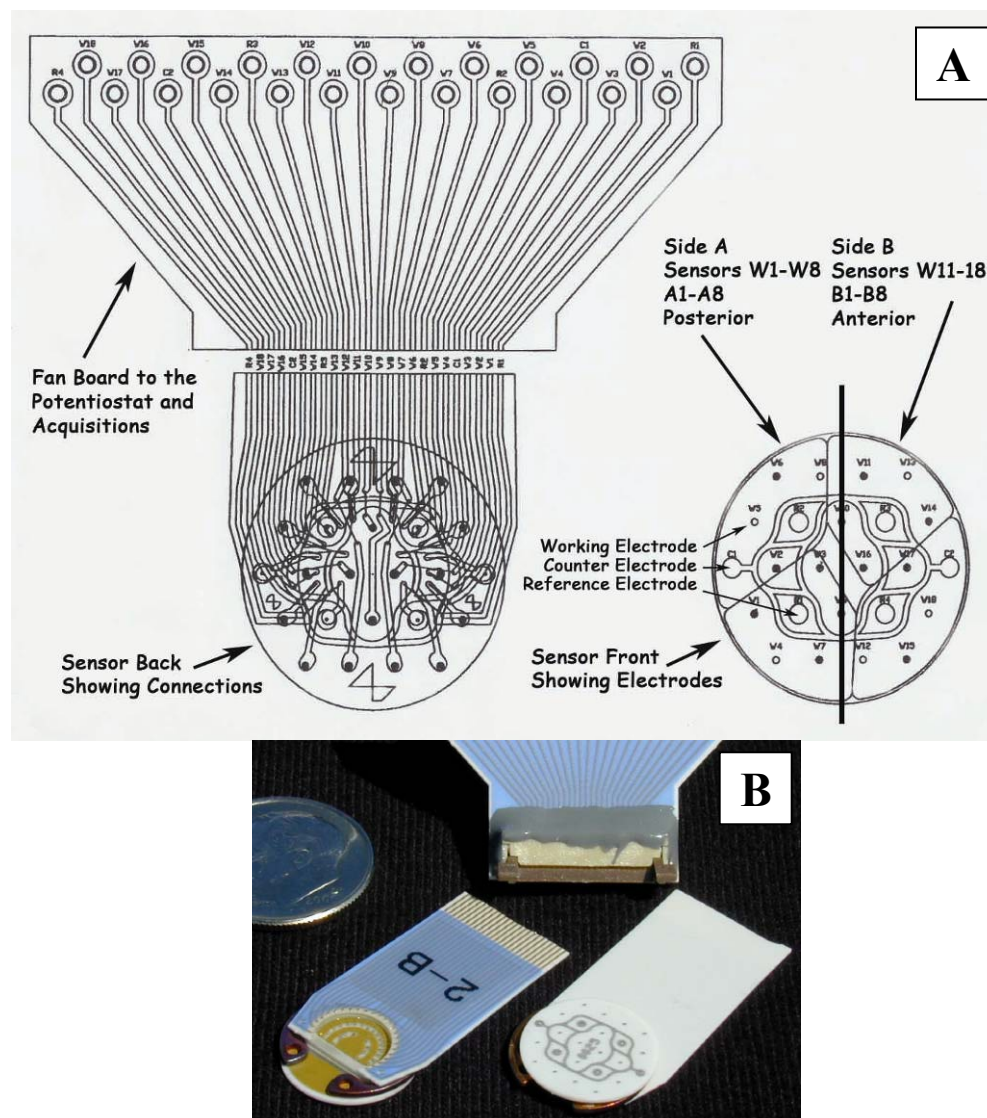


**Figure 2.1** Design of the Planar Oxygen Sensor Array

(A) shows the design of the planar array. The rear of the sensor is shown in order to diagram the wiring, while the front displays the different electrodes and their configuration. A vertical midline is drawn to demonstrate the symmetry of the working electrodes, and thinner lines define the quadrants, four groups of four working electrodes each connected to a single reference electrode. Either side of the midline is a group (side A or side B) of eight sensors which will correspond to one or the other biomaterial once the biomaterial membrane has been mounted. The fan board is shown to demonstrate how the wiring connects to the breakout box (Figure 2.2) before reaching the potentiostat. (B) is an image of a planar array showing the rear and front respectively. On the rear, the wiring feeds through the ceramic array to and along the blue sensor backing. At the top of the backing, the gold plated connections are the site of transfer information between the electrodes and the potentiostat. The retaining ring is also visible behind the array.

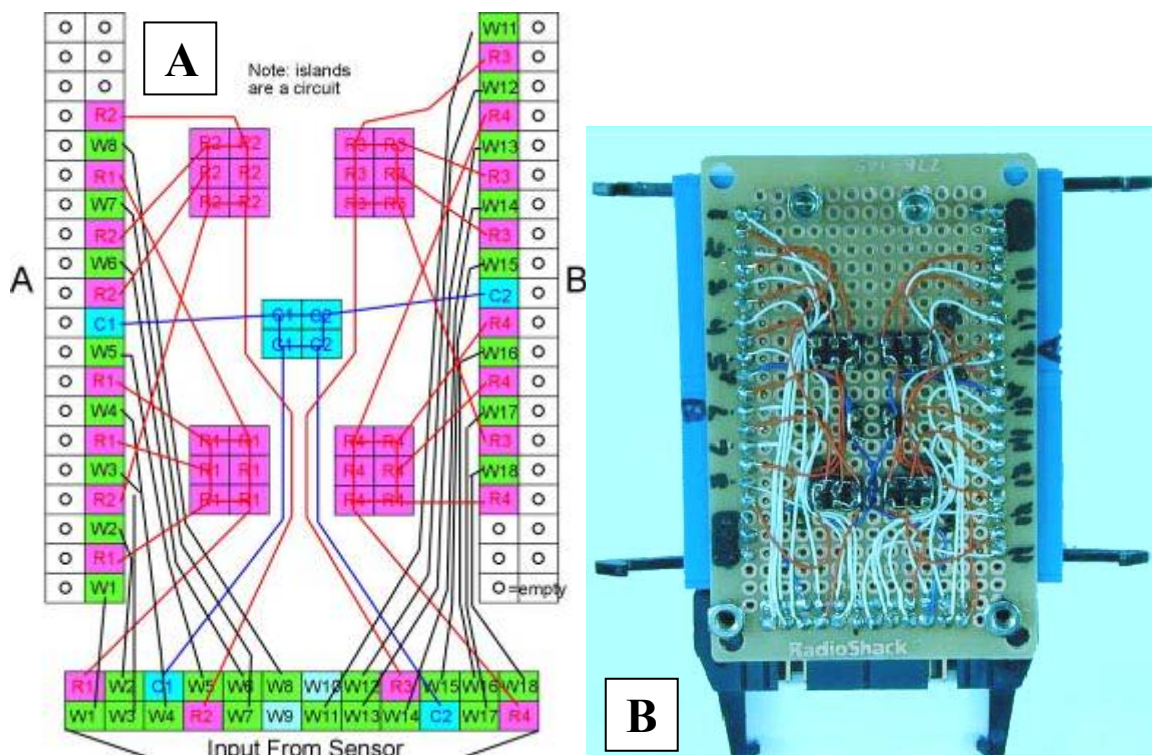


**Figure 2.2** Design of the Sensor-Potentiostat Breakout Box

(A) shows the design of the breakout box, where the incoming electrode signals from the sensor are divided into two groups, A and B, and sent to different potentiostat boards. The breakout box is the site where the reference and counter electrodes are pooled, represented here by the five islands in the middle of the box. (B) is an image of the underside of the breakout box, showing circuitry.

encased (Figure 2.2). The separation greatly simplified troubleshooting and data analysis.

### 2.3.1.2 Sensor Preparation and Pre-Implant Calibration

Prior to use, sensors were soaked in distilled water to remove excess salts, then soaked in Phosphate Buffer for 72+ hours to hydrate the internal conductive hydrogel layer to isotonicity with subcutaneous tissue. All sensor arrays were pre-calibrated prior to being encased in the biomaterials membranes.

Calibration is described in greater detail in Chapter 3, which discusses the differences between pre-implantation and post-explantation calibration sensitivity for the

arrays used in this experiment. In brief, the sensors were placed in a warm, moist gas chamber and subjected to gas mixtures with specified oxygen content. The resulting sensor responses were plotted against oxygen concentration to create a linear calibration standard for each electrode, referred to as the *in vitro* sensitivity of the sensor to oxygen.

### **2.3.1.3 Signal Acquisition**

The potentiostat converts the currents between each working electrode and the counter electrodes into output potentials that can be amplified by gain setting (Figure 2.3). The default gain setting was (1V/10nA), but in some cases, the initial values of an acquisition were taken at lower gain, then multiplied by a factor of 10 during the data workup, introducing negligible error. The resulting analog potentials are converted to digital using a NI-DAQ card (National Instruments) and recorded using an in-house program written in Labview software (v6.13, National Instruments).

## **2.3.2 Preparation of the Biomaterials**

### **2.3.2.1 Dual Biomaterial Membrane Fabrication**

Titanium window chambers (WCs) had excess metal oxide removed by polishing and ultrasonication with an oxide remover (Branson). WCs were vacuum dried and cleaned with anhydrous alcohol to remove all moisture prior to application of several layers of 3-aminopropyltriethoxysilane (APTES), 2% in acetone, which acts to prepare a surface for bonding to a hydrophobic substance<sup>(83)</sup>.

Whatman #2 microporous cellulose filters, 8 $\mu$ m exclusion size, were cut to 15mm half circles, then rinsed and ultrasonicated in distilled water followed by anhydrous alcohol to completely remove detritus, moisture, and loose fibers.

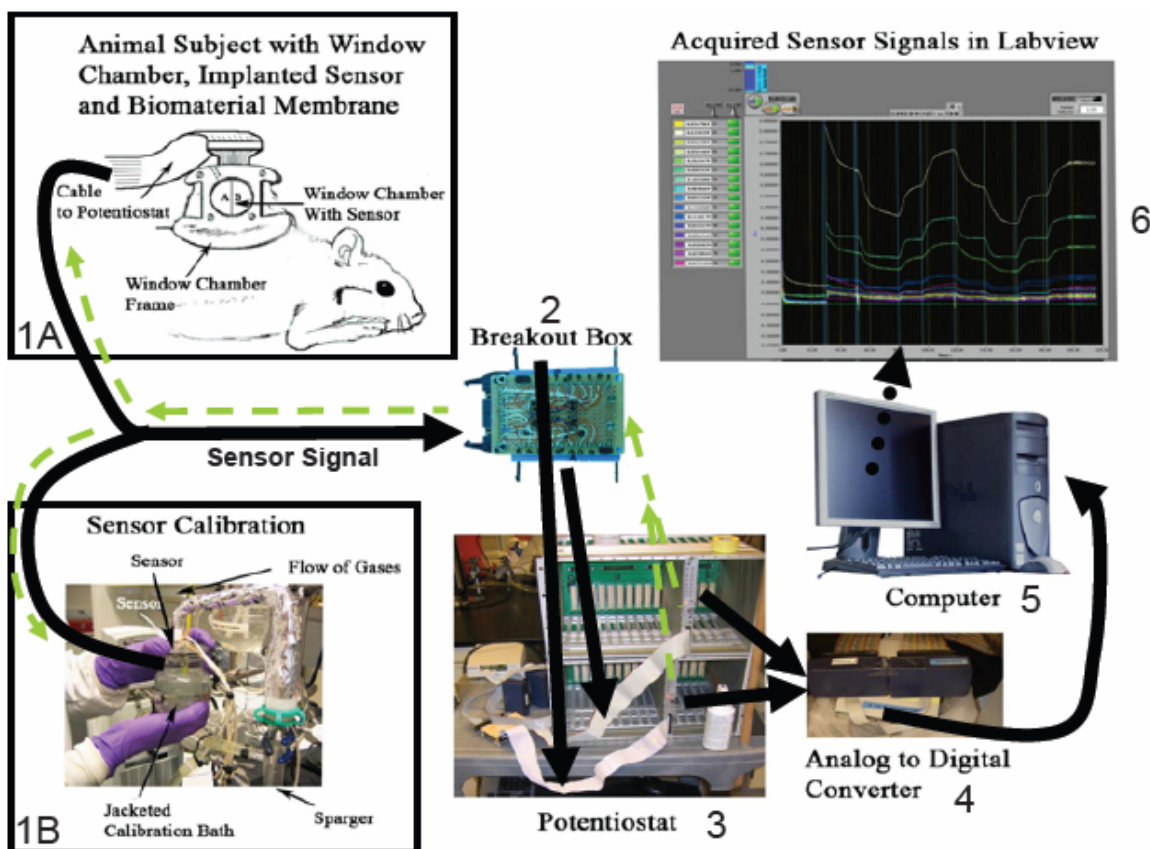


**Figure 2.3** The Sensor Signal Acquisition Pathway

The signal (dotted line) originates with the sensor array either *in vivo* (1A) or in the calibration flask (1B). The breakout box (2) separates the signals and sends them to the potentiostat boards (3) which pass them to the analog to digital converter (4) and finally to the computer (5), where the signals are displayed and recorded (6). The potentiostat (3) also returns feedback (dashed lined) to enforce the potential between the reference and working electrodes. The breakout box (2) connects each working electrode to its respective reference and counter electrodes back on the sensor array.

Sylgard 184 Encapsulating Polydimethylsiloxane (PDMS) (Dow Corning) was mixed at a 9:1 ratio of monomer to curing agent and degassed under vacuum. To ensure very even distribution of curing agent, a low speed rotary tool was employed.

Glass coverslips vapor deposited with Chlorotrimethylsilane (CTMS) liftoff agent<sup>(49)</sup> were mounted into the APTES coated titanium window chambers. WCs were then coated with PDMS and baked upright for 8 minutes at 65°C to initiate partial curing. The coverslips were removed, and the cellulose half circles were mounted, covering

exactly half of the chamber. The window chambers were placed between CTMS treated slides in a small press which was then used to level and compress the membranes to their minimum thickness. Another 20-40 minutes of heating finalized the PDMS curing. The final window chamber mounted membrane (Figure 2.4) was cleaned of particles and steam sterilized.

The dual material membranes each consisted of a 210 $\mu$ m thick disc 15mm in diameter, half cellulose and half PDMS. Both half circle sections are adhered to one another and to a thin layer of PDMS referred to as the backing in which the cellulose was embedded. Because the window chamber has a thin lip of metal against which the array sits, the PDMS backing filled this region as well.

#### **2.3.2.2 Microscopic Observations of the Membrane**

Membranes where the cellulose did not adhere to or was soaked through by the PDMS backing layer were discarded. Several membranes were cross-sectioned to assess PDMS penetration of the cellulose. A Philips XL30 electron microscope was used to obtain scanning electron microscopy images of the PDMS and verify its smoothness (Figure 2.5). Metal coating of the PDMS was not required, but care was taken to image regions of the PDMS before the scanning beam caused them to acquire charge.

#### **2.3.2.3 Sensor Calibration with Biomaterials**

Calibrations of sensors' sensitivity to oxygen were also performed for each sensor array with its dual biomaterial membrane. The values from the *in vitro* calibrations with the biomaterial membranes were used to normalize *in vivo* sensor responses, factoring out the effects of diffusion through the biomaterials.

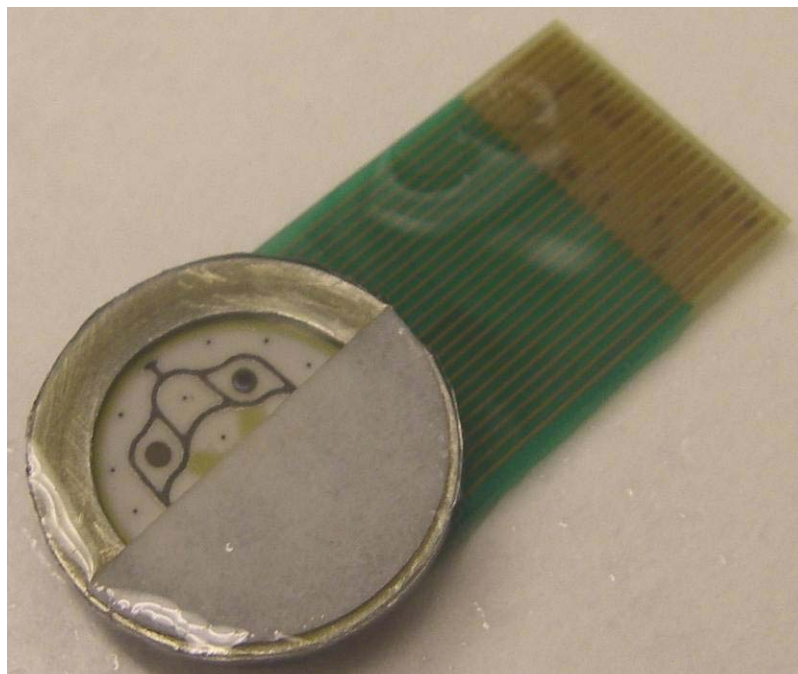


**Figure 2.4** Membrane Encased Sensor Array

The image shows a moist planar oxygen sensor array encased in the dual biomaterial membrane. The cellulose is mostly opaque, but the transparent PDMS allows the underlying electrode pattern to be seen. Each of the 8 small dots is a working electrode. The metal ring around the electrode pattern is the window chamber.

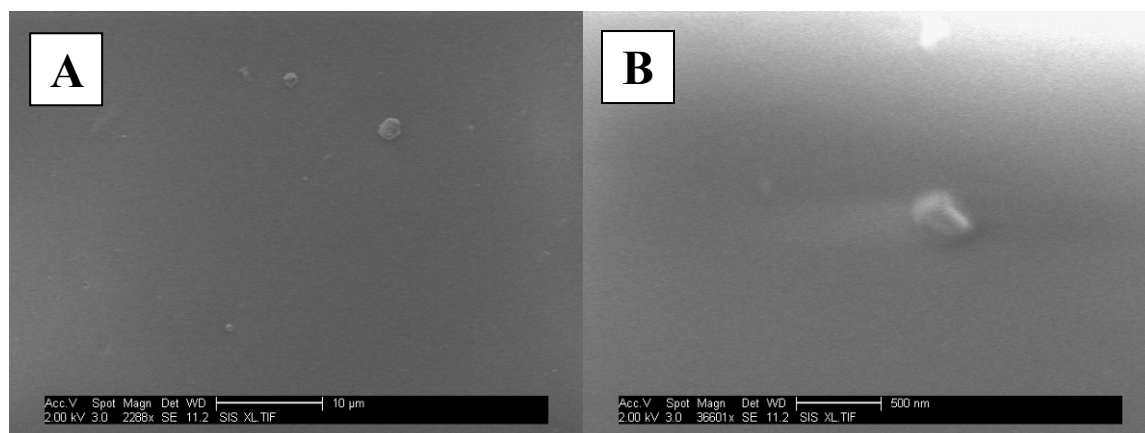


**Figure 2.5** Scanning Electron Images of the PDMS Membrane

(A) and (B) are scanning electron images of uncoated PDMS taken at 2288 and 36601X magnification respectively. Dust was not prevalent but was found to show contrast and to demonstrate the submicron smoothness of the material. The brightness in (B) is due to electron charging of the material. The large dust speck in (B) is  $\sim 250$ nm wide.

### **2.3.3 Preparation of the Window Chamber**

#### **2.3.3.1 Window Chamber Design and Fabrication**

Titanium window chambers and chamber frames were manufactured as previously reported<sup>(40, 86)</sup>. In brief, two frame halves are used to sandwich the rodent dorsal fold, which is then retained by four corner mounted bolts and multiple sutures. The frame supports the dorsal fold in a vertical position and houses the window chamber (WC). The thin, cylindrical WC mounts to the center of the frame and projects slightly inwards to create a seal with the tissue. A bracket is mounted to the top of the frame to protect the array's gold plated connector teeth from the animal.

Window chambers with deeper interiors (1.65mm) were used for this experiment, in order to incorporate the biomaterial membrane. The chamber interior was inwardly tapered to force the retaining ring against the sensor array and create a positive pressure seal between the hydrophobic membrane of the array and the biomaterials.

#### **2.3.3.2 Mounting the Sensor Array and Dual Biomaterial Membrane to the Window Chamber**

The sensor array was mounted into a window chamber already fitted with the dual biomaterial membrane (Figure 2.6). Sterile tape was used to build up the frame behind the sensor, and heavy suture was used to lash the array backing tightly to the frame. The mechanical restriction prevented torque between the sensor backing and the array, as well as relative movement between the sensor and the biomaterials. Finally, an impermeable plasticized disc was mounted behind the sensor to prevent damage and seal out air.

The center line of the material membrane was oriented normal to the animal's body, achieving symmetry and aligning the materials with potential motion of the retractor muscle. Anterior versus posterior placement of the biomaterials was randomized.

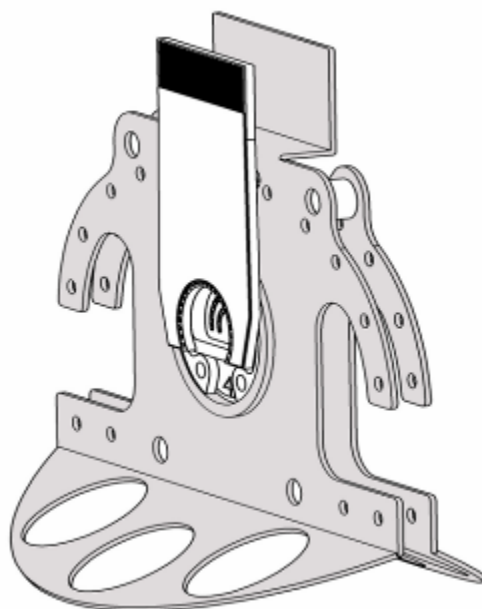


**Figure 2.6** Window Chamber Assembly with a Mounted Sensor Array<sup>(84)</sup>

The two gray halves of the frame sandwich the animal's dorsal fold keeping it upright and holding the white sensor, mounted in the window chamber, against the exposed tissue site. The four medium sized holes house bolts for structural support, while the small holes are for sutures to support the frame and reduced skin movement relative to the sensor. The largest holes are to reduce the frame weight.

## **2.3.4 Preparation of the Animal Subjects**

### **2.3.4.1 Animal Subjects**

Two litters of hamsters received at the same time were kept until they were 150-200g in weight and 4-6 months of age. The animals were fed Purina hamster chow ad libitum and regularly conditioned to sleeping in acrylic tubing, and to be accustomed to the sound and feel of compressed gases.

### **2.3.4.2 Mounting the Window Chamber to the Hamster Dorsal Fold**

The window chamber procedure is detailed elsewhere<sup>(86)</sup>, but is briefly described here with notes on modifications specific to this study.

Five hamsters were injected with 100 mg/kg of ketamine (Fort Dodge, Iowa) and 0.25 mg/kg of medetomidine (Domitor, Espoo, Finland) IP. The dorsal region was shaved, depilated, and sterilized, then drawn into the chamber frame. A round area of the dermis, just larger than the window chamber, was cut from the center on the animals left, posterior to the A0 and V0 vessels. The underlying retractor muscle was sectioned and turned outwards. The membrane and array were positioned against the exposed contralateral retractor muscle, using the outwardly folded muscle layer to create a fluid seal. Doubled sutures were passed through the frame and dorsal fold in around the frame periphery, ensuring minimal relative movement between the tissue and frame. Recovery was aided by IP injection of 500 µg/kg of Atipamezole HCl (Antisedan, Pfizer, Exton, PA), a medetomidine antagonist, and 3-15 µg/kg of Buprenorphine HCl analgesic (Buprenex, Reckitt Benckiser, Richmond, VA). A plasticized disc was sealed over the skin side of the chamber frame to prevent the animal from damaging its own tissue.

### **2.3.5 *In Vivo* Data Collection**

#### **2.3.5.1 Baseline *In Vivo* Acquisitions**

*In vivo* signal acquisition was performed by coaxing the hamsters into restrictive acrylic tubes with a narrow slit allowing the chamber frame and array to project<sup>(60)</sup>. The hamster and tube were placed in an acrylic box sealed with a removable rubber sheet.

On 4, 7, 11, and 14 days post-surgery, the signal was acquired with the animal breathing room air, 20.9%, oxygen. On medium gain, the potentiostat was activated, recording the initial drop of sensor signal until the signal was mostly resolved. Signal magnitudes for each electrode were calculated by averaging 1-3 minutes of the resolved signal at high gain. Noise was defined for simplicity as the standard deviation of the signal over this sample period as a percent of the magnitude (See Figure 4.2 for a visual).

### **2.3.5.2 Hypoxic Challenges**

On days 7 and 14 post-surgery, following acquisition of the baseline signal, the animals were put through a series of oxygen challenges. First, the animal's chamber and dorsal fold were wrapped in gas-impermeable plastic and sealed. Then, the rubber sheet was replaced and a certified 15.0% oxygen mixture was introduced through a cotton filled baffle at the animal's head. Once the signal was technically resolved, less than a 2.5% change over 5 minutes of acquisition, the oxygen mixture was changed to 10.0%, then back to 15.0%, and finally to room air, each time allowing technical signal resolution.

### **2.3.6 Subcutaneous Tissue Collection and the Post-Explantation Sensor Calibration**

On day 14, during signal acquisition, the hamsters were given a dose of ketamine/medetomidine anesthetic, followed by a lethal dose of Nembutal, 30mg/kg. Following death, the sensor array was removed from the chamber and membrane and calibrated bare.

### **2.3.7 Data Analysis: Data Filtration and Normalization**

Signal magnitudes in excess of 1.2V, the maximum valid signal from the potentiostat, and signals with noise above 50% of magnitude were eliminated from analysis. Signal values below 0.0011V were determined to have unacceptable noise to magnitude ratios and/or some negative values, and so were eliminated.

Sensor signal magnitudes for *in vivo* baseline responses were normalized to the baseline signal magnitudes from the array pre-calibration with biomaterials, in order to separate the diffusive resistance of the materials from that of the tissue. Signal

magnitudes from the hypoxic challenges were all normalized to pre-calibration signal magnitudes at 10.0% oxygen.

In order to separate out differences in the signal due to inherent tissue structure versus tissue changes due to the foreign body and wound healing response, sensor signal magnitudes were also separately normalized to their first *in vivo* baseline magnitudes. Both normalization methods were multiplicative rather than subtractive, since sensor signals are linearly proportional to oxygen concentration.

ANOVA and paired t-testing with an assumption of unequal variances was used for statistical analyses between groups<sup>(48)</sup>.

## **2.4 Results and Discussion**

### **2.4.1 Validation of the Preparation**

#### **2.4.1.1 Microscopic and Physical Analysis of Dual Membrane Integrity**

Treatment of the titanium window chambers with APTES provided excellent adherence of the cured PDMS, preventing removal of the PDMS by tension or shear, both a significant problem with PDMS cured to untreated titanium. In addition, the membrane seal to the titanium proved moisture and air-tight under mild applied pressure.

Microscopic analysis of membrane cross sections demonstrated that PDMS attached to the cellulose by integrating only the outermost fibers (Figure 2.7). These results were validated by mechanical removal of the cellulose, where only a few fibers were left behind and no PDMS was removed. The two step PDMS curing process allowed the cellulose to integrate while preventing the PDMS from penetrating or disturbing the cellulose's trabecular pore structure.

It was noted that while the interface of cellulose and PDMS was flush in the membrane's dry state, once wet, the cellulose swelled by 13.5-42.3%, possibly causing an imbalance in contact with the tissue.

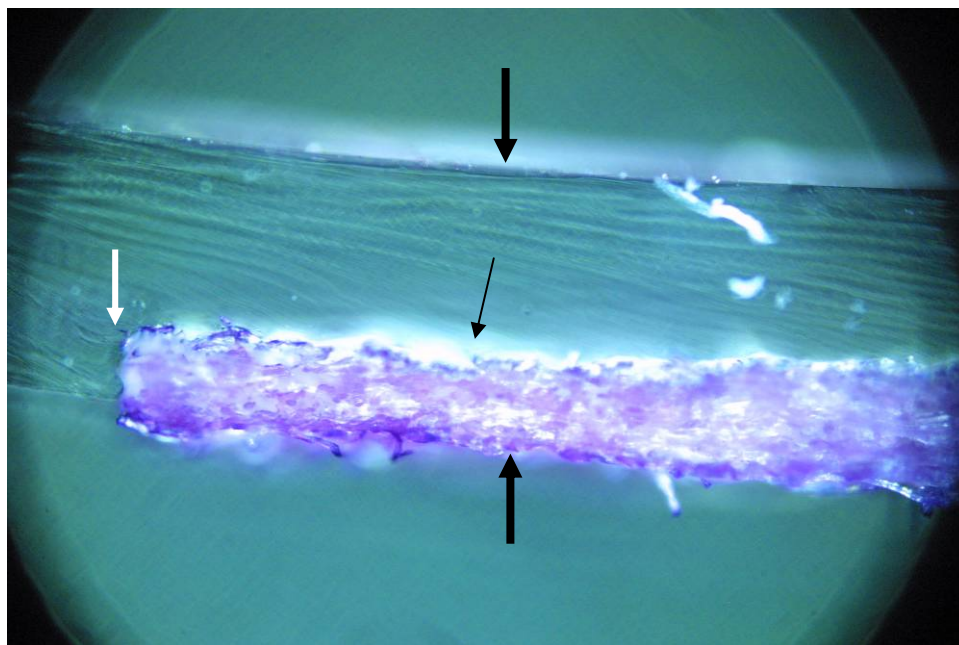


**Figure 2.7** Cross Section of a Dual Biomaterial Membrane (40x)

A membrane cross section shows the cellulose to be integrated spatially into the PDMS, but with only the outermost fibers embedded. A Hematoxylin stain of the cellulose (darker color) penetrated up to the outermost fibers (bright white) noted by the small black arrow. The larger black arrows designate the edges of the membrane, and the white arrow points to the membrane's center line.

#### **2.4.1.2 Calibration of Sensor Response In Vitro**

Sensors for all arrays responded quickly and cleanly to changes in oxygen during calibration. Oxygen reduction was shown to be diffusion limited by the linearity of the sensitivity to oxygen (Figure 2.8).

One sensor on array H-136-8, sensor B2, was determined to be inactive. In addition, the connector selected for the experiment, while providing the lowest noise and most consistent signal magnitudes, did not consistently transfer data from sensor A6.

### 2.4.1.3 Validation of Sensor Response In Vivo

All sensors responded to changes in exogenous, or inspired, oxygen (Figure 2.9). The curve form of the shift in magnitude was exponential, as expected of a diffusion limited shift in concentration, and plots of signal magnitude versus oxygen were linear.

Shifts in the signal magnitude during hypoxic challenges were too slow to indicate leakage or other direct access of the sensors to exogenous air. Thus, changes in sensor signal are believed to represent oxygen changes in the tissue.

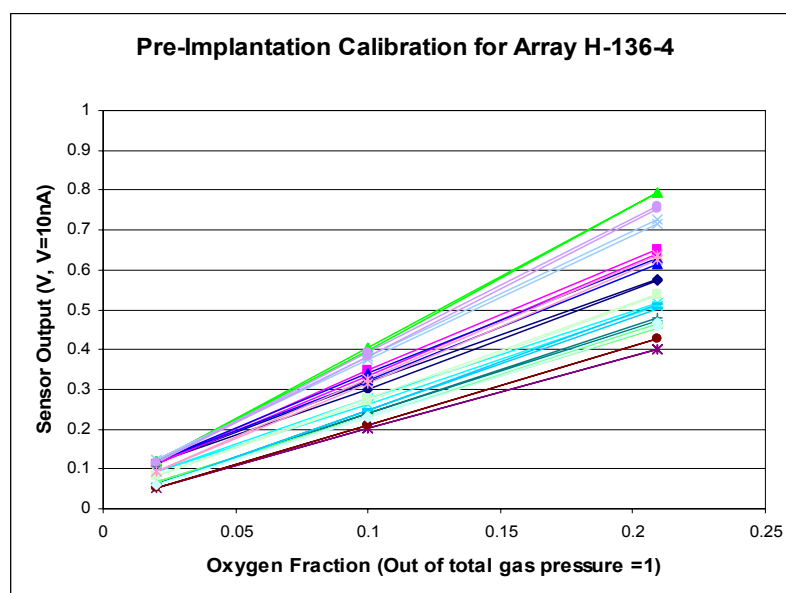


**Figure 2.8** Pre-Calibration of a Bare Sensor Array

The linearity of the response of 16 sensors to oxygen (linearity of the sensor sensitivity) is demonstrated during an *in vitro* calibration for a bare sensor array. 2.0, 10.0 and 20.9% oxygen were used in this example.

## 2.4.2 In Vivo Data

### 2.4.2.1 Baseline Oxygen Concentration in the Hamster Window Chamber

The average baseline partial pressure for oxygen in the hamster skinfold was determined by calibration to be 2.92%, or 22.2mmHg, on day 4 following surgery. This

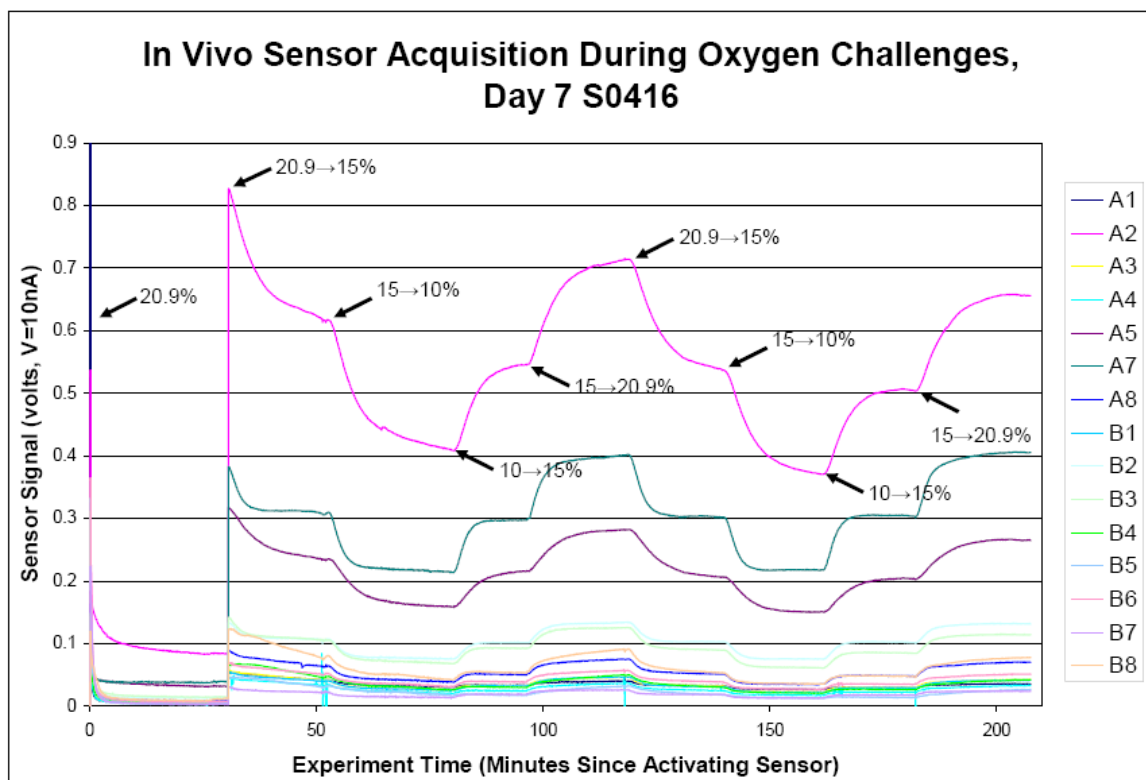


**Figure 2.9** *In Vivo* Sensor Acquisition During Two Cycles of Oxygen Challenges

A plot of sensor signal magnitude over time during an *in vivo* acquisition with two rounds of inspired oxygen challenges. “A” sensors are the 8 encased in PDMS, and “B” sensors are the 8 encased in cellulose. Arrows along the curve for sensor A2 indicate the times at which exogenous oxygen levels were increased or decreased and the initial and final exogenous oxygen concentrations. The first portion of the acquisition, labeled by the 20.9% arrow, was performed at medium gain in order to view the initial drop in signal. At about 30 minutes, the gain was increased to high, multiplying the signals by a factor of 10. (An example of *in vitro* oxygen challenges can be seen in Figure 5.1).

value correlates well to those seen previously in the hamster skinfold<sup>(66)</sup>, which averaged 2.95% oxygen. By day 14, the average had risen to 5.99%, or 45.5mmHg, higher than expected for tissue not immediately adjacent to larger microvessels. Previous studies were usually performed in the first few days following window chamber implantation, not providing an expectation of how oxygen concentrations from later in the experiment should appear. These studies were also performed in the dermal tissue rather than muscular, though muscular tissue would not be expected to have significantly higher oxygen levels under resting conditions.

Baseline sensor signals on day 4 *in vivo* were  $86.0 \pm 15.0\%$  lower than exogenous oxygen, further validating that the oxygen contributing to the sensor signal was from the adjacent tissue.

An ANOVA analysis comparing baseline signals taken on different days showed significant differences ( $P < 0.0062$ ). Signals on days 4 versus 11 and 11 versus 14 were determined to be significantly different ( $P < 0.020$  and  $P < 0.053$  respectively), and those for days 4 and 14 highly different ( $P < 0.0001$ ). However, due to high variance, the null hypothesis was not rejected for comparing days 7 and 11.

#### **2.4.2.2 Biomaterials and In Vivo Sensor Signal Magnitudes: Normalized to Pre-Calibrations with Biomaterials**

On days 4 and 7, pre-calibration normalized signal magnitudes for PDMS encased sensors were greater than those for sensors encased in cellulose ( $P < 0.015$ ,  $n=71$ ), indicating greater flux to these sensors (Figure 2.10). On days 11 and 14, the effect diminished greatly, and all sensors had roughly the same normalized signal. Removal of outlying values 3 and 2 standard deviations had no effect on the form of Figure 2.10 or statistical significance, indicating that the results were not due to a few erratic sensors.

Variance of sensor values was high through the experiment, especially for days 4 and 7, reducing the significance of the comparison between cellulose and PDMS encased sensor values on day 4 ( $P < 0.157$ ). On day 7, PDMS encased sensor signal magnitudes were 1.95 times higher than for cellulose, a difference that was significant despite the variance ( $P < 0.036$ ). These results correspond well to previous work which determined that biomaterial driven neovascularization peaks near 7 days<sup>(97)</sup>. The inflammatory response<sup>(43)</sup> and infiltration of inflammatory cells also experiences a peak near 7 days<sup>(88)</sup>, supporting the supposition that differences in tissue oxygen transport due to biomaterial implantation could manifest during this time period and begin to diminish afterwards.

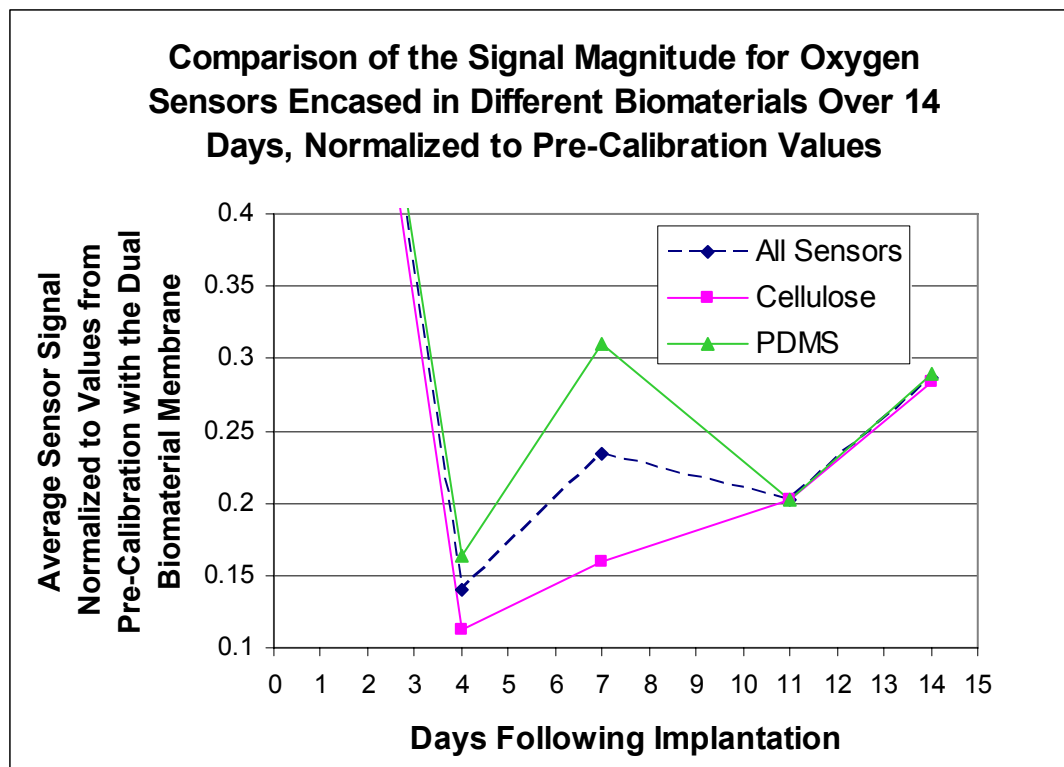


**Figure 2.10** Effect of Biomaterial Encapsulation on Baseline Sensor Signal Magnitudes. Signal magnitudes, normalized by *in vitro* calibrations with biomaterials, were larger for PDMS encased sensors than for those encased in cellulose on days 4 and 7. But the two groups' magnitudes were similar on days 11 and 14. The signal magnitudes on day 0, referring to the pre-surgical calibration with biomaterials, are equal to 1 as a consequence of the normalization, and are truncated for clarity. *In vivo* oxygen pressure ( $PO_2$ ), calculated by comparison to pre-calibration values, are shown on the right hand dependent axis (Each 1.0% exogenous oxygen = 7.6mmHg of  $PO_2$ ).

#### 2.4.2.3 Biomaterials, Signal Magnitude, and Hypoxia

On day 7, there was large difference between signal magnitudes for sensors encased in different biomaterials during hypoxic conditions (Figure 2.11), though the difference was not exactly in proportion to the oxygen levels. When exogenous oxygen levels were dropped to 15.0%  $O_2$ , a 28.2% decrease, the gap between average signal values for PDMS and NC encased sensors dropped 39.8% from baseline. The drop to 10.0% oxygen, a 52.2% change, decreased the gap by 62.1%. The differences are not perfectly proportional, which would imply that the biomaterials may have differentially

affected oxygen stasis mechanisms in the tissue to some degree, mechanisms responsive to hypoxia. This was supported by the observation that sensor sensitivity was not seen to be differently affected by the material membranes *in vitro* ( $P>0.47$ ).

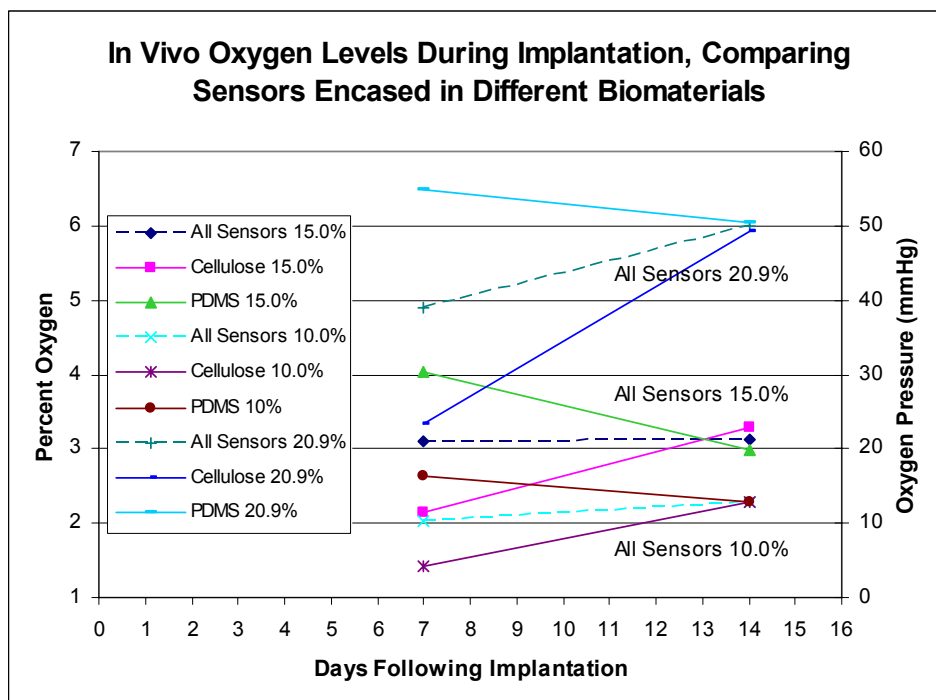


**Figure 2.11** The Gap Between PDMS and Cellulose Encased Sensor Signal Magnitudes at Baseline and Hypoxic Oxygen Levels, Days 7 and 14

On day 7, the gap between signal magnitudes (pre-calibration normalized) for PDMS and cellulose encased sensors was greatest proportionally at 20.9% exogenous oxygen. The gap grew more than proportionally smaller for hypoxic conditions of 15.0 and 10.0%. On day 14, the gaps diminished substantially at all oxygen levels. The dependent axes are the calculated *in vivo* oxygen levels in both percent partial pressure and mmHg.

Lower oxygen levels were avoided in the primary experiments to prevent agitating the animals, which generally slept during mild hypoxic conditions, but panicked when 5.0% oxygen was introduced. Ischemia by vessel constriction was likewise avoided to prevent damage to the tissue that could have marred histological evaluations. Thus, future experiments are suggested to perform careful observations, with respect to

implanted biomaterials, of the tissue response to compressive ischemia and deeper hypoxia.

#### **2.4.2.4 Early In Vivo Values, Measurements Taken Prior to Day 4**

Sensor signals taken prior to day 4 were found to high noise and magnitudes that drifted significantly over time. In particular, signals observed on day 0, the day of surgery, could not be properly averaged. This indicates contact between the sensor and the tissue was initially poor. It may be possible to acquire effective signals in the three days following surgery, but for these experiments, time was given to assure proper equilibration of the sensors with their tissue environment.

#### **2.4.2.5 Normalization to the First In Vivo Values**

Sensor signals magnitudes were normalized to the first *in vivo* values, taken on day 4 of implantation, to account for any differences in the inherent tissue structure. The signal magnitudes normalized in this fashion followed a similar pattern to those normalized by pre-calibration (Figure 2.12), demonstrating that much of the differences observed occurred post-implantation. PDMS encased sensors signal magnitudes were much larger than those of cellulose encased sensors on day 7 ( $P < 0.020$ ,  $n = 71$ ), but unlike the pre-calibration normalized values, this disparity in magnitude persisted through to days 11 and 14. The differences were not statistical on these days, but demonstrated a systematic difference due to biomaterials throughout the implantation.

Comparison of these results to those for the pre-calibration normalized signal indicate that while some of the differences seen between the biomaterials occurred before day 4, much occurred from days 4-7, and some portion of these changes persisted through to day 14. Thus, analysis of the sensor data by both normalization methods rules out that differences in diffusion are due to the biomaterials alone, and further, the normalization to the first *in vivo* values demonstrate with greater surety that much of the difference in

flux observed for sensors encased in different biomaterials are due to changes in the tissue which took place after the sensors were implanted. This is as opposed to the differences in magnitude being due to inherent differences in tissue structure. Future work with earlier and more frequent time points is suggested to better determine the timeline of changes in the tissue.

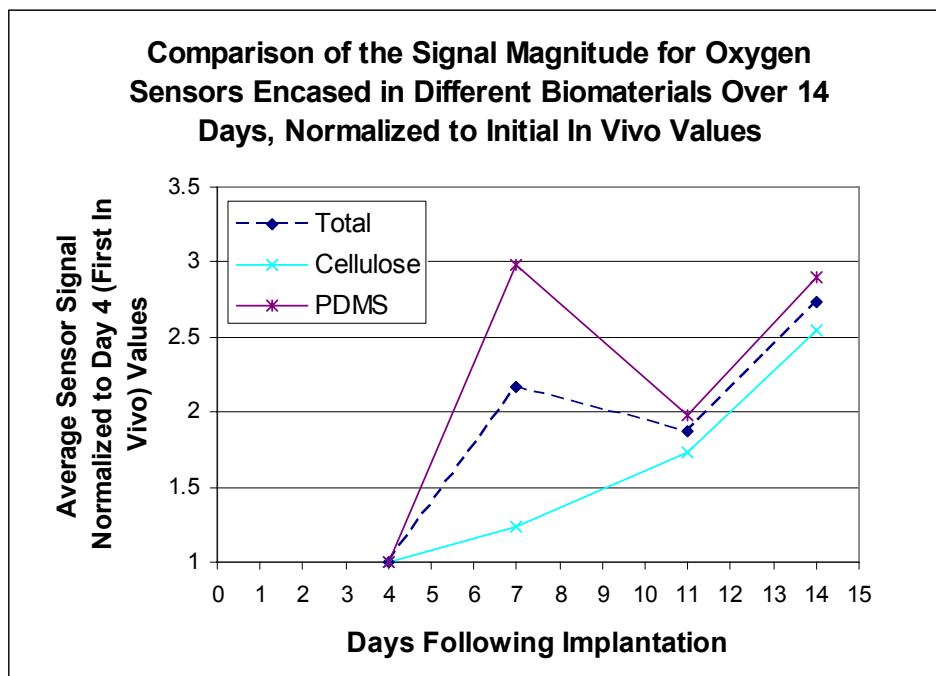


**Figure 2.12** Effects of Biomaterials on Signals Normalized by Early In-Vivo Values  
Signal magnitudes for PDMS covered sensors were systematically higher than those for cellulose encased sensors, when normalized by the signal magnitudes from day 4. As was true for magnitudes normalized by pre-calibration values, the largest difference was seen on day 7. Day 4 values were all equal to 1 as a consequence of normalization. Pre-calibration values on day 0 are not shown, but are roughly an order of magnitude larger.

#### 2.4.2.6 Anterior Vs. Posterior Placement of Sensors In Vivo

There were no significant differences on any day of the experiment between anteriorly versus posteriorly located electrodes for pre-calibration normalized sensor magnitudes. There were also no statistical differences during the hypoxic experiments, between anterior and posterior sensor signal magnitudes at 10.0 or 15.0% inspired

oxygen. Since anterior versus posterior placement of the biomaterials was randomized, these results further validated that differences seen between sensor signals were due to the tissue reaction to biomaterials, not inherent differences in tissue structure.

### 2.4.3 Noise of the Sensor Signal

#### 2.4.3.1 Noise Magnitude and Origins

Noise, as represented by the standard deviation of the acquired signal as a percent of magnitude, was fairly low *in vivo*,  $1.73 \pm 2.19\%$  at 20.9% oxygen. Only rarely did signal noise complicate measurements of magnitude or observations of dynamics.

Noise both *in vitro* and *in vivo* was observed to be largely proportional to the signal magnitude, with larger signals having larger noise for an individual experiment. However, noise was not proportional to gain, with higher gains having 8.9% less noise than lower gains. Thus, at least this portion of the noise is artifact originating between the potentiostat and the computer.

Noise for each sensor, as compared to its bare *in vitro* state, increased 50.0% with the addition of the biomaterials to the array, and then another 39.5% by the first time point of implantation (Figure 2.13). Post-explantation calibration of the arrays demonstrated that the noise levels of the arrays themselves did not change during the implantation. Thus, the biomaterials and tissue were the source of much of the signal noise, 23.9 and 28.3% respectively if noise is assumed to be linearly proportional to the signal magnitude. The remaining noise is assumed to be due to the artifact already described and the connections between the potentiostat and the sensor. Noise changed *in vivo*, increasing substantially to day 7 before falling to near *in vitro* levels by days 11 and 14, as the contact between the sensor and tissue improved and oxygen flux in the tissue became more stable.

### 2.4.3.2 Noise and Hypoxia

Both *in vitro* and *in vivo*, signal noise was inversely proportional to exogenous oxygen (Figure 2.14). *In vivo*, the increase in noise with lower exogenous oxygen was substantially higher, even accounting for the order of magnitude lower oxygen concentrations that reach the sensor *in vivo* (Figure 2.14B). The increase at lower oxygen potentially indicates that oxygen stasis mechanisms in the tissue, such as changes in hemoglobin saturation, functional capillary density<sup>(79)</sup> or cellular metabolism, may be a source of variations in local oxygen flux. Increased heterogeneity of tissue oxygenation and subsequent measurement variance during hypoxia has been observed previously<sup>(63)</sup>.

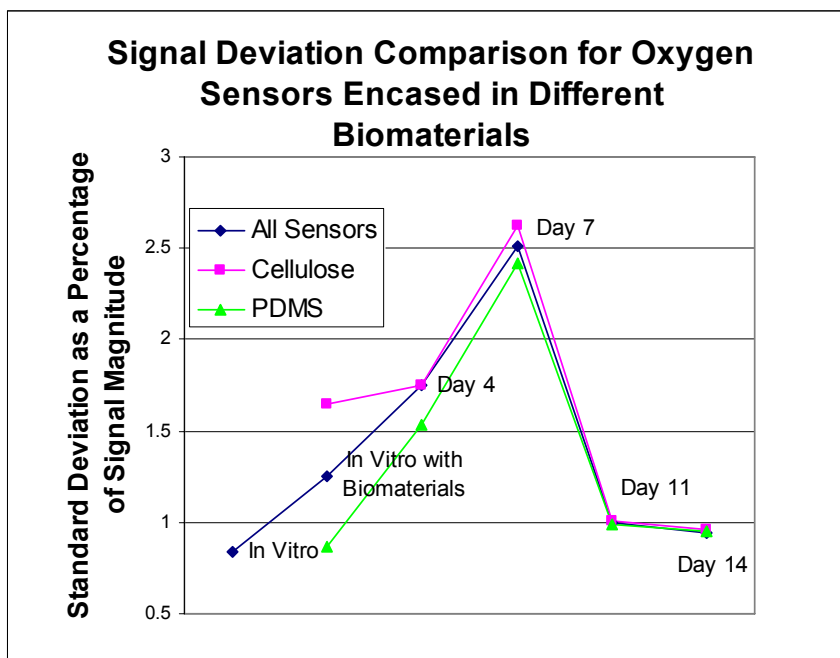


**Figure 2.13** Comparing Noise for Sensors Encased in Different Biomaterials at Baseline Noise levels, as represented by deviation of the signal, increased with the addition of the biomaterial membrane and with implantation in the animal subject. Noise continued to increase during the implantation to day 7, and then fell off to near *in vitro* values by day 11. Overall, cellulose encased signals reported higher noise than those in PDMS. This difference persisted from that seen *in vitro* with the biomaterials membrane, and diminished over the course of the implantation.

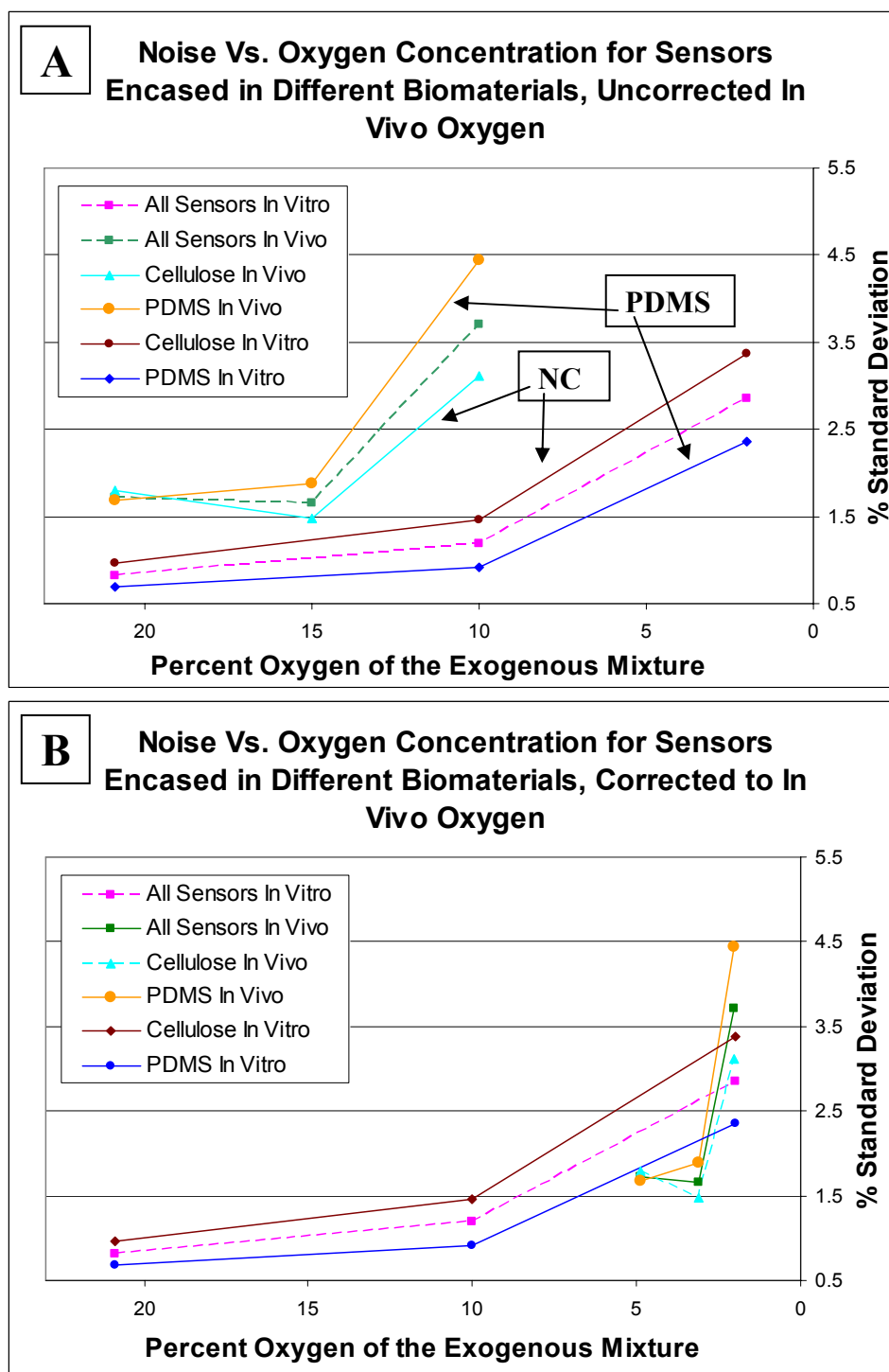


**Figure 2.14** Noise During Hypoxic Challenges

Noise *in vitro* during hypoxic challenges on days 7 and 14 was more linearly proportional to exogenous oxygen than *in vivo*. While cellulose encased sensor noise was higher *in vitro*, more so at lower oxygen, the reverse was true *in vivo*, where PDMS encased sensor noise was higher, more so at lower oxygen. (A) shows the plots of error versus exogenous oxygen, while (B) corrects the *in vivo* oxygen levels to calibrated values.

### 2.4.3.3 Noise and Biomaterials

Cellulose encased sensors had higher noise than those encased in PDMS at baseline (Figure 2.13), both *in vitro* and *in vivo* ( $P < 0.0075$  for all *in vivo* data after removal of outlying values above 2 standard deviations). The difference *in vivo* diminished by days 11 and 14, but was still significant for the experiment as a whole.

### 2.4.3.4 Noise, Biomaterials, and Hypoxic Challenges

While PDMS encased sensor noise was lower than that of cellulose encased sensors at inspired room air, noise for PDMS encased sensors became larger during hypoxic conditions (Figure 2.14), surpassing that of cellulose encased sensors. The gap increased as oxygen levels decreased. This is the exact opposite of the trend seen *in vitro*, where cellulose encased sensor noise was higher, increasingly so with lower oxygen.

Noise was not determined to vary significantly with repeated oxygen challenges.

## 2.4.4 Sensor Sensitivity In Vitro and In Vivo

The sensor sensitivity to oxygen *in vitro* and *in vivo* during the oxygen challenges on days 7 and 14, were shown to be linear. The  $R^2$  value for day 7 was 0.99, and that for day 14 was 0.94. Thus, at least for the mild hypoxia the animal was subjected to, flux in the tissue was proportional to exogenous oxygen.

There were no statistical differences seen either *in vitro* or *in vivo* between slopes of the sensitivity for sensors encased in the different biomaterials (Figure 2.15). In comparing the *in vivo* sensitivity slopes on days 7 versus 14, there was an average 31.0% increase, but the difference was not statistically different ( $P < 0.196$ ) and did not depend on biomaterials. No correlation was seen between the slopes and the thickness of granulation tissue, measured histologically (Chapter 6).

The high oxygen tension values seen in the tissue on days 7-14 indicates that the sensor's *in vivo* sensitivity may have been overestimated. The relative nature of all relationships described here would be preserved if this was the case, but differences would be smaller.

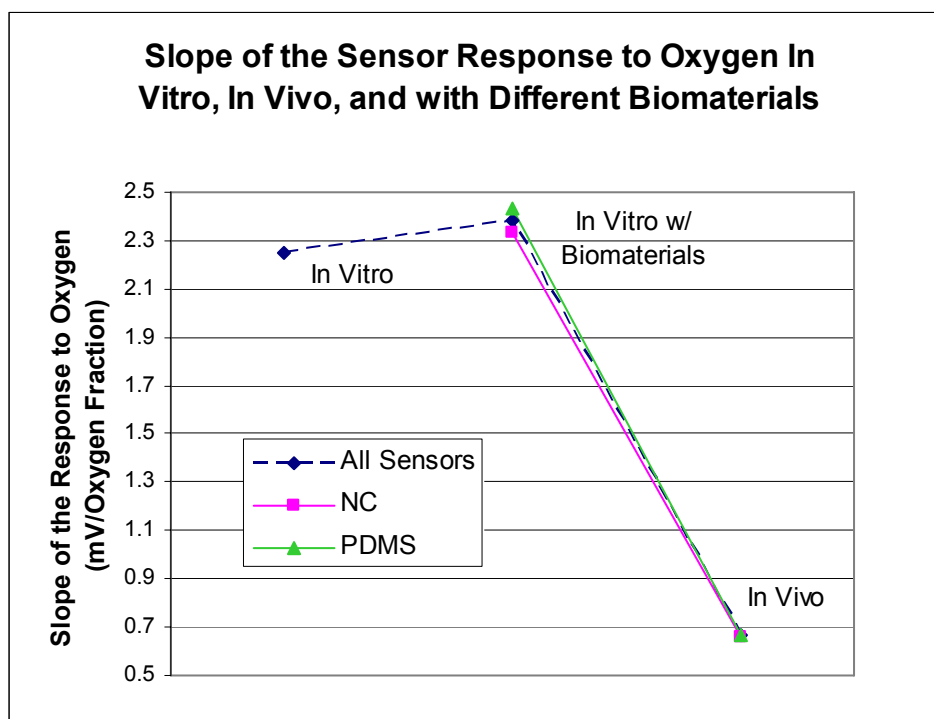


**Figure 2.15** Slope of the Sensor Response to Oxygen: Sensitivity

The slope of the sensor sensitivity, the plot of sensor signal magnitude versus exogenous oxygen concentration, was slightly higher *in vitro* with biomaterials. The slope decreased significantly on implantation ( $P < 10^{-25}$ ). Sensors encased in different biomaterials were not shown to have significantly different slopes *in vitro* and had virtually identical slopes *in vivo*.

#### 2.4.5 Effects of Anesthesia on Signal Magnitude and Noise

Following anesthesia with ketamine and medetomidine, signal magnitudes were observed to drop only slightly,  $0.28 \pm 2.20\%$ . However, noise rose by an average of  $27.8 \pm 9.6\%$ , indicating that change in the microvasculature might have affected flux variance. Neither change was different for sensors encased in different biomaterials.

Deeper investigation of the microvasculature's role in signal noise and magnitude using vasoactive substances<sup>(53)</sup> and compressive ischemia is suggested by this study.

#### **2.4.6 Residual Sensor Signals Following Euthanasia**

Following death of the animals, signal magnitude did not immediately go to zero. Post mortem oxygen challenges showed some response from the sensors, indicating that despite measures taken to isolate and seal the surface of skinfold around the array, diffusion of oxygen through the dermis may still be providing a portion of the observed sensor signal. These observations suggest future study in animals with thicker dermal layers, such as fat sand rats or pigs. Still, subcutaneous tissues are believed to be partially dependent on oxygen diffusion through the skin<sup>(124)</sup>, and it is a point of design that must be considered for the study and practical application of subcutaneous sensors.

#### **2.4.7 Potential Impact of Sensor Driven Hypoxia**

While the sensor was active during less than 5% of the implantation, when operational, it may have provided a substantial oxygen sink. Thus, it cannot be completely ignored as a source of tissue change, possibly leading to vascular perfusion and capillary recruitment changes similar to those seen in chronic hypoxia<sup>(115)</sup>. It is possible that some portion of the differences in tissue diffusion seen for different biomaterials was the result of the biomaterials differentially modulating electrode driven hypoxia. However, for the purposes of this study, given that the sensors encased in each biomaterial were equally active, and that the results are to be applicable to metabolically active sensors and devices, the meaning of the results does not change. A logical progression from this work would be further experimentation and comparison of the tissue response to continuously active sensors versus briefly activated sensors.

## 2.5 Conclusion

The important result of this experiment was the demonstration of a difference in signal magnitude for sensors encased in smooth versus microporous biomaterials for the first 7 days of implantation. Comparing signal normalization methods demonstrated that most of the difference in the signal magnitude between sensors encased in different biomaterials developed during days 4-7, and that changes that occurred during this time persisted for the duration of implantation. The timeline of the differences corresponds well to the timelines of inflammatory and foreign body responses. Future experiments one week in length, with more frequent time points, would be desirable to further explore the timeline of biomaterial driven changes in the tissue.

Noise was also seen to be biomaterial dependent, being greater for cellulose encased sensors at room air and greater for PDMS encased sensors during hypoxic challenges. Sensor noise increased during anesthesia, irrespective of biomaterials encasement, indicating potential changes in the vasculature. Observations of the effects of vascular ischemia and deeper hypoxia are suggested for future work to further determine whether differences are due to convection or diffusion.

The linearity of the sensor response to oxygen was not expected. However, the oxygen levels in this study were not below the animal's comfort zone, and thus may not have explored the non-linear portion of the sensor's *in vivo* sensitivity.

Overall, the use of multi-sensor arrays and the dual biomaterial membranes allowed direct comparison of the biomaterial effect on sensor signal without the usual complications of animal to animal variations or local heterogeneity. This technique offers a more quantitative method of comparing surface biomaterials for biosensors and other diffusion based devices. Pairing this data with careful quantitative histology would provide insight into the tissue response to biomaterials and its effect on oxygen transport.

## **CHAPTER 3: Effects of Implantation on Sensor Performance**

### **3.1 Abstract**

The sensor response to exogenous oxygen was calibrated for 4 oxygen sensor arrays before and after 14 days of implantation in the hamster window chamber. The magnitude of the sensor response and the slope of the sensor sensitivity were found to be consistent for calibrations before implantation and after explantation, with small but not statistically significant differences. In addition, electrodes that had been implanted under PDMS did not perform differently from those that had been implanted under cellulose, improving confidence that differences in these sensors' performance seen *in vivo* can be regarded as due to the biomaterial properties and the tissue environment.

Variance for the slopes and magnitudes of each array's sensitivity did increase significantly from pre-implantation to post-explantation, most likely due to differences in local hydrogel hydration and osmolarity which would affect oxygen diffusivity in the hydrogel and conductance of current by the gel. Rate of response to exogenous oxygen changes increased for most sensors post-explantation, also a potential consequence of changes in the hydrogel

### **3.2 Introduction**

Several of the sensor performance criteria outlined in this dissertation rely on a consistent linear relationship<sup>(85)</sup> between the presence of local oxygen and the corresponding electrode signal, the sensor's per se sensitivity. *In vitro* calibrations provide information about the performance of sensors without the complicating factors of biomaterials or living tissue. Comparison of pre-implantation and post-explantation

calibrations are also a method of validating the results of *in vivo* experimentation. An assurance that differences in signal observed *in vivo* were not due to inherent change in the sensor strengthens confidence in using the sensor to comment on diffusion in the tissue.

A methodical study was performed of the differences seen in calibrated sensor signals on 4 oxygen sensor arrays, before and after 14 days of implantation in the hamster window chamber. Changes in the sensitivity slope and the rate of sensor response to changes in exogenous oxygen were calculated. Shifts in sensor rank by signal magnitude, from pre to post-calibration were also observed. For all criteria, changes in performance were specifically compared for sensors which had been encased in different biomaterials.

### **3.3 Materials and Methods**

Chapter 2 methods describe sensor array preparation and signal acquisition. Chapter 4 methods describe time constant calculations.

#### **3.3.1 Gas Phase Sensor Array Calibrations**

Sensor calibration techniques are described elsewhere<sup>(85)</sup>, but specifics are mentioned here for the sake of reproducibility.

Sensors were moved from the PBS soaking solution into a jacketed flask of PBS kept at 30°C, the approximate temperature of the hamster window chamber as measured by wire thermistor. Rubber diaphragms sealed the moist flask from the array connector teeth. Buffer was extracted from the flask to expose the sensor face, and compressed gas mixtures of specified oxygen were introduced through a flow controlled sparging unit to maintain a moist flow of gas to the array.

Each sensor had signals acquired at least three oxygen levels from 2.0 to 20.9%, transitioning between the levels in fixed steps and allowing signals to resolve until change was less than 1% over 5 minutes. Once resolved, signals were recorded for 1-3 minutes to determine an average magnitude and to estimate signal noise.

Care was taken to address potential error from salt deposits and moisture on the sensor connector, including replacing silicone rubber seals with rubber septums, increasing the frequency of connector cleaning, and re-calibrating sensors when needed. Overall, the connector was the greatest potential source of noise and error. Thus, a new, low-noise connector was selected for the dissertation experiments and cleaned and dried regularly.

### **3.3.2 Data Processing and Analytical Techniques**

The signal magnitude was plotted against exogenous oxygen concentration to determine the best fit line. When curves demonstrated nonlinear behavior, the best resolved signal magnitudes were plotted and the curve was extrapolated.

Rank was assigned for the magnitude of each sensor's signal for the pre and post-calibrations, and then compared. All statistical comparisons between groups were made using paired t-tests with an unequal variance assumption.

## **3.4 Results**

### **3.4.1 Changes in Sensor Sensitivity**

Sensor sensitivity was shown to be both pre- and post calibration to be linear in the tested range of 2.0-20.9% exogenous oxygen (Figure 3.1), validating array function. Sensitivity slopes for the 4 arrays decreased an average of  $2.30 \pm 6.80\%$ , which was not statistically significant. Variance of the sensitivity slopes for all sensors increased an

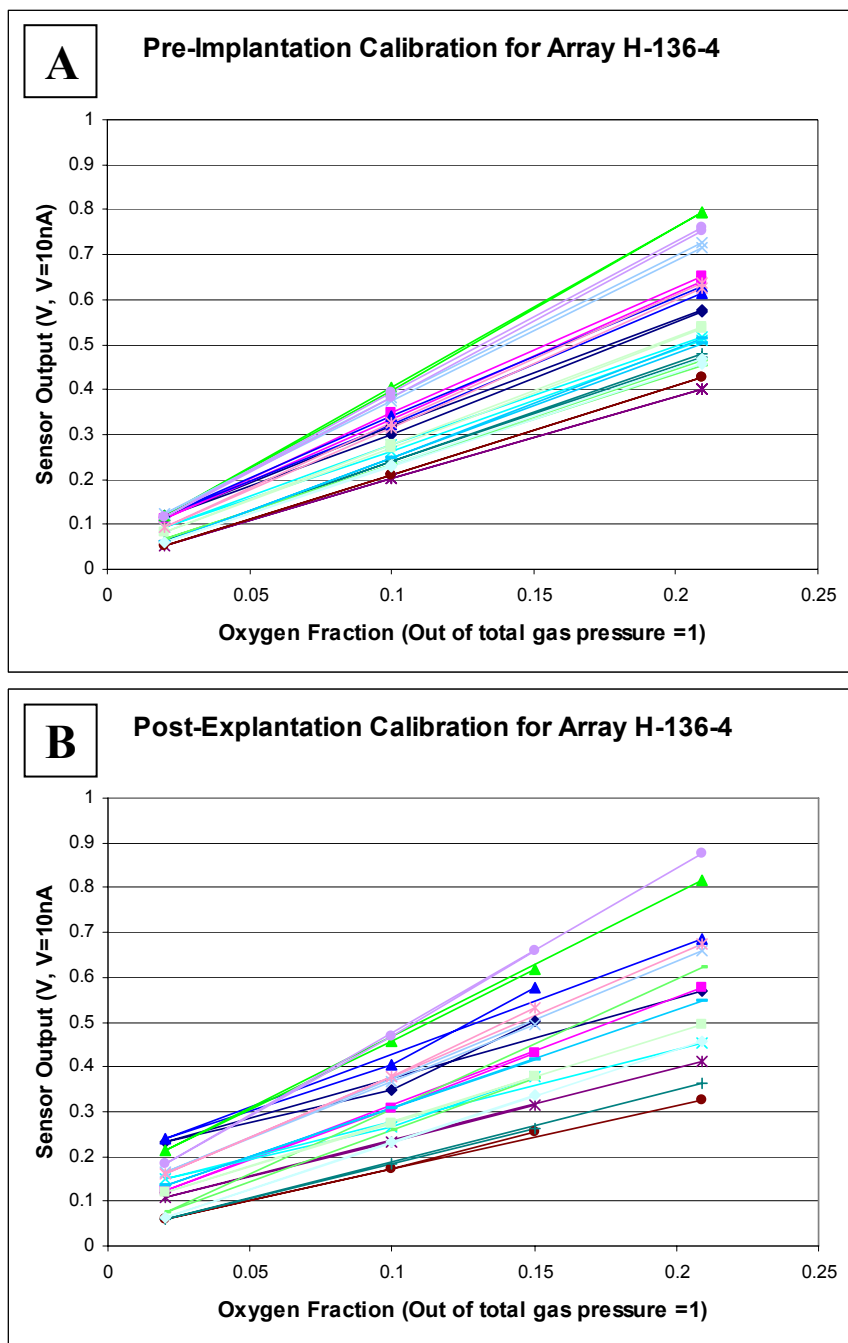


**Figure 3.1** Comparing Pre-Implantation and Post-Explantation Array Calibrations  
 An example of 16 sensor responses to exogenous oxygen is shown for pre- (A) and post- (B) calibrations. The plots double back due to the order of the experiment, where oxygen concentration of the gas mixture was initially lowered to 2.0%, then raised back to 10.0 and then 15.0%. While the linearity of the curves is well preserved, there are changes in the slope and the variance of the signal magnitude and response slope.

average of  $36.4 \pm 43.0\%$  from before implantation to post explantation.

Sensors ranked by magnitude pre-implantation shifted an average  $2.09 \pm 0.63$  ranks when compared to post-explantation rankings. Median rank shift was  $1.5 \pm 1$ , illustrating the effect of outliers. It is worth noting that if one sensor on an array moves from the lowest to highest rank, with no other change, the result would be an apparent average rank shift of  $(n-1)/n$ , here  $15/16$ .

These results indicate that the arrays were stable during implantation. Consistent sensitivity implies a consistent response to oxygen, the most crucial point of sensor performance. Only one sensor, H-136-8, stood out and skewed variance averages on its first use in animal S0411. However, on the second use of the sensor, these issues were reduced, implying that the sensor may not have been properly conditioned prior to its first use.

### **3.4.2 Ratio of Post versus Pre-Calibration Signal Magnitude**

The average ratio of pre versus post calibration signal magnitude was  $0.974 \pm 0.14$ , with the majority of values nearing unity. The ratios for 10.0 and 15.0% oxygen responses were closer to unity, at respectively 0.96 and 0.97. This implies a general consistency in sensor signal magnitude.

### **3.4.3 Relation to Biomaterials**

There was no statistically significant difference for changes in sensitivity slope or variance, or rank shift, between electrodes encased in different biomaterials, for any of the 4 arrays,  $P > 0.251$ . However, there was a slight systematic difference in sensitivity slopes for sensors that were encased in PDMS. Their slopes rose 6.08% more than cellulose encased sensors, with negligible differences in variance. This increase in sensitivity may indicate that PDMS encasement affected hydration or osmolarity changes in the hydrogel differently than cellulose encasement.

Rank shifting differences between electrodes encased in different biomaterials were negligible and statistically not significant. There was also a negligible difference between biomaterials in the calculated ratio between pre and post-calibration signal responses.

There was also a small but systematic increase for all arrays in sensitivity slope magnitude and variance for the right hand anterior side of the sensor (B) relative to the left hand posterior side (A), independent of biomaterials. The difference was isolated to the third quadrant reference electrode on the affected arrays. An error in the reference electrode, such as dissolution, may have affected its enforced potential, affecting the reduction kinetics and thus the sensitivity of the sensors to oxygen. The stability of the reference electrodes in has been well established<sup>(9, 81)</sup>, but effort should continue to be made to automate methods of detecting systemic changes in sensor function *in vivo*.

#### **3.4.4 Dynamics**

The time constants for the calibrations, indicative of the rate of sensor response (Chapter 4), did increase for some arrays without statistical significance. However, since these changes do not correlate to changes in magnitude, they are likely due to the same differences in hydrogel hydration or osmolarity, or differences in compression of the sensor's thin inner membrane.

Delays from the introduction of shifts in exogenous oxygen to the beginning of the sensor response did not appear different for pre and post-calibrations. Diffusion through the sensor's inner membrane and hydrogel layer would be expected to be rapid. Thus the majority of the delay would be due to the calibration apparatus, likely diffusion of gases through the sparging unit, and not the array. Any noticeable change would have indicated a substantial alteration to sensor performance.

### 3.4.5 Potential Influences on Sensor Performance

Hydration or salt content of the sensor hydrogel are the most likely differences seen between pre and post-calibration sensor performance. Both would affect oxygen diffusivity and differential swelling of the hydrogel. The current between the working and counter electrodes is dependent on the ability of the hydrogel to transmit the electron carrying species, affecting rate of magnitude shift, but not the magnitudes themselves.

### 3.4.6 The Effect of Connectors

The potential for salt accumulation and moisture interference were greater for *in vitro* calibrations, affecting the stability of signal conduction by the sensor connector. Reduction of the number of connection points is suggested for future design, saving maintenance time and reducing potential error.

## 3.5 Conclusion

Sensor signal magnitudes and sensitivity were found to be fairly consistent from pre-implantation to post-calibration, the change in neither being statistically significant. In addition, the *in vitro* performance of electrodes that had been implanted under PDMS was not significantly different from the performance of those implanted under cellulose, improving confidence that differences seen *in vivo* were genuine. The biomaterial surface chosen does not appear to impact performance of the sensor array per se through the implantation process.

The time constant for most sensors increased, implying a more rapid rate of curve resolution following implantation. Signal and slope variance also increased significantly. Both sets of results highlight the importance of stabilizing or monitoring sensor hydration.

## CHAPTER 4: Biomaterials and the Sensor Dynamic Response to Single Oxygen Shifts

### 4.1 Abstract

Five hamsters fitted with oxygen sensor arrays encased in two adjacent but different biomaterials were subjected to challenges consisting of step shifts in exogenous oxygen. The dynamics of the sensor response observed were the rate of signal response and delay in signal response following oxygen challenges. The time constant  $\tau_c$ , was used as a single value representation of the rate of signal response. Dynamics were compared for sensors encased in cellulose versus PDMS, for increases versus decreases in oxygen, for *in vitro* versus *in vivo* cases, and finally correlated to histological measurements of the explanted tissue, specifically the average vascular proximity.

The rate of sensor signal change in response to challenge and to a lesser extent its delay were found to be well correlated to vascular proximity, an estimation of oxygen's diffusion path in the tissue, indicating potential use of oxygen challenges for non-invasive characterization of an implanted sensor's vascular access. Time constants for response curves representing increases in oxygen were found to be larger than for those representing decreases. This ratio was greater *in vivo* and also corresponded well to vascular proximity, suggesting a differential tissue response to increases versus decreases in tissue oxygen. The existence of this differential response for even very small tissue volumes indicated vascular changes to be responsible.

Oxygen transfer was significantly affected by biomaterials. Sensors encased in PDMS had faster responses than those encased in cellulose to shifts in exogenous oxygen, despite the average distance to vasculature being greater in their adjacent tissues, indicating a relatively higher diffusion rate to these sensors than to those encased in

cellulose. However, thinner microporous membranes would offer less diffusive resistance, and due to their correlation to closer vasculature may be potentially better choices for sensors with dynamic applications.

The diffusion constant for the array environment was estimated on average to be  $1.91 \pm 0.86 \times 10^{-5} \text{ cm}^2/\text{s}$ . Differences between biomaterials were not statistically significant.

## 4.2 Introduction

### 4.2.1 General

Implanted sensor performance is not limited to static criteria, but rather is highly defined by the sensor dynamics. The ability of a sensor to react to local changes both quickly and predictably is key to its diagnostic and predictive applications.

There are many stages of transfer and diffusion before a change in exogenous oxygen levels manifests in the sensor's tissue environment. The lag, or delay, between the triggering event and the beginning of the actual shift in the sensor signal is an important value. A minimal delay is optimal, especially for diagnosis or closed-loop sensor application where quick decisions may affect patient health and survival. Additionally, if the delay is greater than the timescale of the triggering event, one event may easily become confused with another as their effects overlap.

Change in oxygen concentrations in the tissue following a change in vascular oxygen can be modeled as a diffusion-limited step shift (derivation and discussion in Appendix A).

$$\text{Equation 4.1} \quad C_t = C_1 - (C_1 - C_0) * e^{(-\tau_c * \Delta t)}$$

$C_0$  and  $C_1$  represent the initial and final concentrations. The exponential term is dimensionless, where  $\Delta t$  is the elapsed time and  $\tau_c$  is the time constant (units of inverse

time) representing the rate of concentration change independent of signal magnitude. As seen in Appendix A,  $\tau_c$  is a ratio of the diffusion constant over the diffusion path. For the three electrode oxygen sensor, the signal is recorded in terms of voltage,  $V$ , which can be linearly converted to oxygen concentration,  $C$ , using calibrated values<sup>(85)</sup>. Equation 4.2 describes the curve form of the sensor response to a step shift in oxygen.

$$\text{Equation 4.2} \quad V_t = V_1 - (V_1 - V_0) * e^{(-\tau_c * \Delta t)}$$

In this study, the time constants of implanted sensors for responses to single shifts in exogenous oxygen were calculated and compared for electrodes encased in different biomaterials, seeking to determine if differences exist in the mass transfer properties of the adjacent tissue. The time constants after 14 days of implantation were related to histological analysis of the explanted tissue and used to estimation the diffusion constant.

#### **4.2.2 Determining Time Constants from Discretely Sampled and Incomplete Curves, Application to Sensor Control Algorithms**

An additional factor that may limit the use of dynamic information in diagnostic or predictive methods involves the accuracy of curve fitting. For the sake of practical application, this study will include exploration of the effect of curve extent, sampling frequency, and specification of endpoint values on time constant calculations. This section will be located in Appendix B.

### **4.3 Materials and Methods**

#### **4.3.1 Data Acquisition from *In Vivo* Oxygen Challenges**

Hamsters were fitted with window chambers and cellulose/PDMS encased planar oxygen arrays. On days 7 and 14 following implantation, the animals were subjected to hypoxic challenges (Chapter 2).

### 4.3.2 Sensor Response Delay Calculations

Delays in sensor response were calculated in all animals during *in vivo* oxygen challenges on days 7 and 14, defined as the time difference between the introduction of a shift in exogenous oxygen concentration and the first time point of the sensor response curve. Delays were separated for oxygen increases versus decreases.

### 4.3.3 Calculating Time Constants

#### 4.3.3.1 Signal Shift Data Preparation in Excel Spreadsheets

The acquisitions resulting from the oxygen challenges were translated to Excel (Microsoft, Version 2003) sheets, where plots were then dissected into individual responses to each change in oxygen. The beginning of each shift was identified visually, and then the points at the beginning were filtered to find one that represented a change in signal more than twice the signal noise and the first point of a consistent trend. Curves ended in the resolved portion previously used to determine average signal magnitude (Chapter 2). For each shift, the signal data between the selected first and last points, along with  $\Delta t$ , was translated to a Tab Separated Values file for importation into Mathematica.

#### 4.3.3.2 Types of Data

1. Signal shifts representing changes in exogenous oxygen concentration of 10.0→15.0% and 15.0→10.0%, were prepared for all animals, on day 14 *in vivo*.
2. Signal shifts were prepared *in vivo* acquisitions for animal subject S0414, including
  - a. the signal shifts for 10.0→15.0% and 15.0→10.0% on days 7 and 14, and

- b. the signal drop following sensor activation on days 4 and 11.
- 3. Signal shifts representing changes between 2.0 and 10.0% exogenous oxygen for the pre-implantation calibration, the pre-calibration with biomaterials, and the post-explantation calibration of array 136-4, corresponding to animal subject S0414.

#### **4.3.3.3 Time Constant Calculations in Mathematica**

For proper recognition by Mathematica (Wolfram Research Labs, Version 5.0), the Tab Separated Values (.tsv) files prepared in Excel were changed to Data (.dat) files. Calculations of the time constant for all 16 sensors on each array were performed using Mathematica's Nonlinear Regression tool, fitting the raw signal data for each electrode to Equation 4.2.  $V_o$  and  $V_1$  values, when specified, were obtained by averaging the resolved signal magnitudes before and after the shift.  $V_o$  values for the initial signal drop following sensor activation were calculated using the same nonlinear regression methods, where both  $V_o$  and  $\tau_c$  were solved for.

The best fit  $\tau_c$  value for each curve was based on error minimization<sup>(12)</sup> between the raw data and an iteratively calculated exponential function. To validate results, the calculated  $\tau_c$ 's were used to plot the final fit curves against the raw signal data. The curves were visually analyzed, and time constants from poorly fit curves, or those with high average squared error, were excluded from further analyses.

#### **4.3.4 Correlating Dynamics to Vascular Proximity**

The distance between the sensor array and the nearest vasculature, defined as microvessels in the granulation tissue or the retractor muscle layer, was calculated for each animal (Chapter 6). This distance is referred to as vascular proximity. In brief, distances were measured using digital images of the explanted tissue histology, with pixel

size calibrated by slide micrometer calibration. Assuming diffusion limited mass transfer, roots of vascular proximity were used in correlations with dynamics.

It is recognized that the proximity calculated by this method may be closer to the maximum than the average. Capillaries in the granulation tissue, closer to the sensor, were more difficult to label and identify than those in the retractor muscle, and therefore may not have been fully accounted for.

Animal S0415 was excluded from most proximity plots due to evidence of some hemorrhage. This animal's results are discussed however as an interesting case.

#### **4.3.5 Comparing Time Constants for Oxygen Increases and Decreases of Equal Step Size: The Shift Directional Ratio**

For each animal subject, the time constants from the *in vivo* oxygen challenges on day 14 were compared for the equally sized increases and decreases in exogenous oxygen, calculating the ratio ( $\tau_c$  Oxygen Increase/  $\tau_c$  Oxygen Decrease), referred to from here on as the Shift-Directional Ratio (SDR).

#### **4.3.6 Estimation of the Diffusion Constant**

Using the average time constants and vascular proximity calculations for day 14 in each animal, the average oxygen diffusion constant ( $DO_2$ ) of the preparation was estimated. This assumed the 2-dimensional approximation of  $\tau_c$  as a ratio of the diffusion rate and the diffusion area<sup>(72)</sup> (Appendix A). Diffusion constants for the PDMS and cellulose membranes were calculated from the *in vitro* calibrations. The PDMS diffusion constant was calculated first, then used to factor out the role of the PDMS layer behind the cellulose, using Equation 4.3, where  $D$  is the diffusion constant and  $d$  is the thickness of each material. Each term has units of time (seconds).

Equation 4.3  $(d_{membrane}^2)/D_{membrane} = (d_{cellulose}^2)/D_{cellulose} + (d_{pdms}^2)/D_{pdms}$

While imperfect, these calculations are intended to demonstrate that with thinner biomaterial membranes and high quality histology, diffusion in the tissue may be estimable using the dynamics of the sensor response.

### 4.3.7 Analysis and Statistical Methods

All comparisons were performed using t-tests, assuming unequal variance.

Error for curve fitting was determined using average squared error, calculated by squaring the distance error between each point on the raw curve and the fit curve, then averaging by the number of points, all as a percent of total magnitude.

## 4.4 Results and Discussion

### 4.4.1 Time Constant Calculations in Mathematica

Curves produced with the calculated  $\tau_c$  values fit the raw signal response curves very cleanly (Figure 4.2), validating the choice of the exponential function and time constants as representative of sensor dynamics. Jumps in the raw data or high noise did not generally produce visibly misfit curves or unacceptable squared error. However, a large proportion of response curves had mildly S-shaped bases, exhibiting inflection opposite that of the rest of the curve. These signal shifts were slightly less cleanly reproduced, with the fit curve resolving early, increasing calculated time constants (Figure 4.2B). The average squared error for these S-shaped curves still fell well below 5% of the relative curve magnitude.

The S-shape in signal shifts could be explained by a source of active diffusive resistance with a low threshold. Alternately, several convective sources at different

distances from the sensor each contributed to the signal, but with small differences in delay, making the initial signal rise slowly, then gain momentum.

### In Vivo Sensor Signals During An Oxygen Challenge

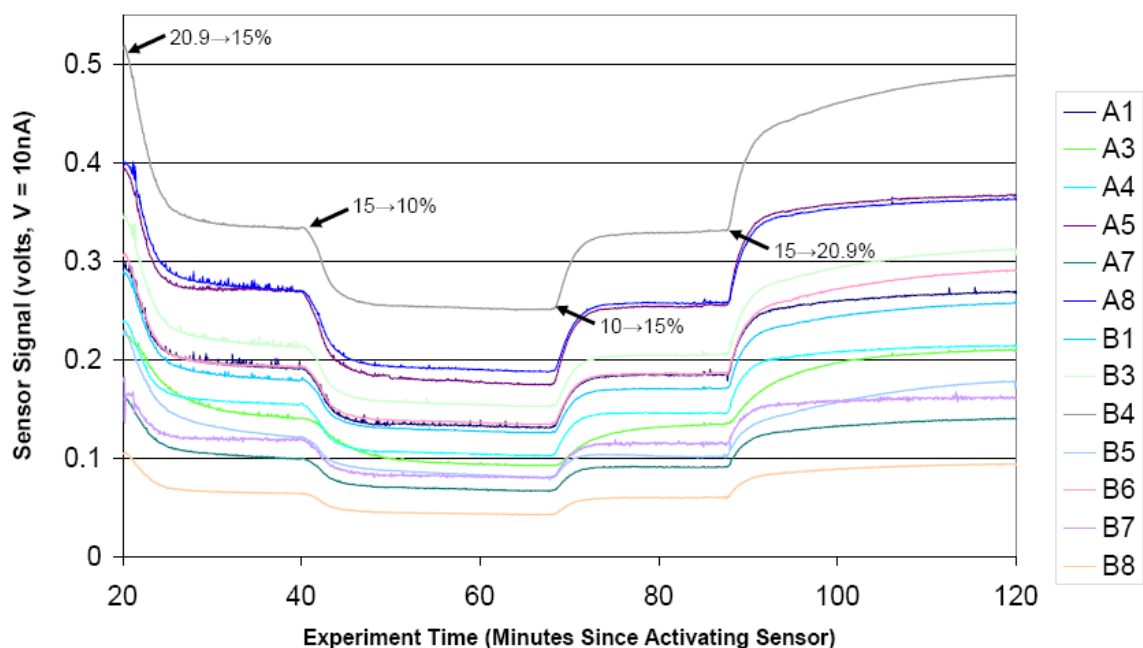


**Figure 4.1** Sensor Signals During an *In Vivo* Oxygen Challenge

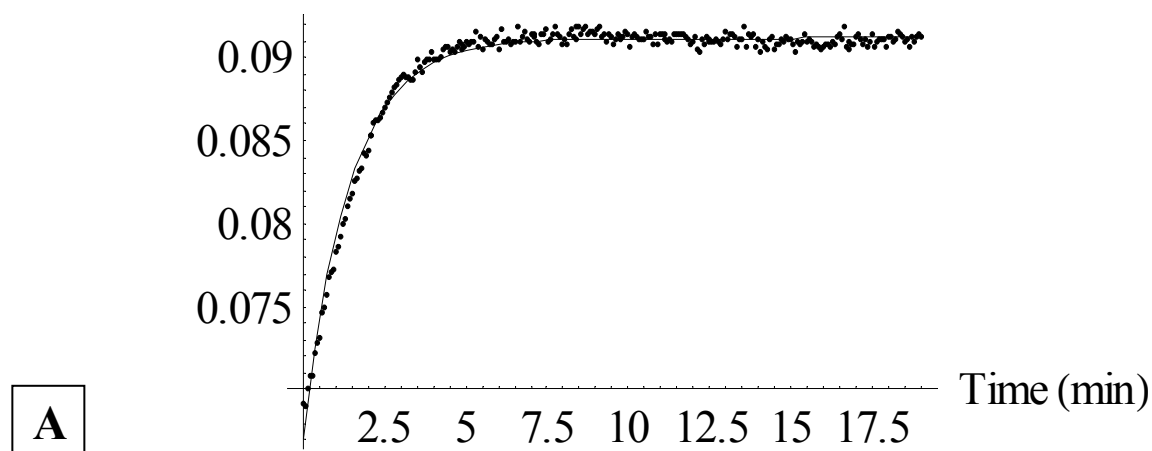
An example plot of recorded sensor signals from an *in vivo* oxygen challenge. Voltage is plotted against time simultaneously for the 16 electrodes of the planar array. Here, the electrodes labeled A are encased in cellulose and those labeled B are encased in PDMS. The beginning of shifts in the exogenous oxygen levels are designated by arrows, with the initial and final oxygen levels noted. Response curves begin with each arrow and end with the next.

## 4.4.2 Delays in the Sensor Response

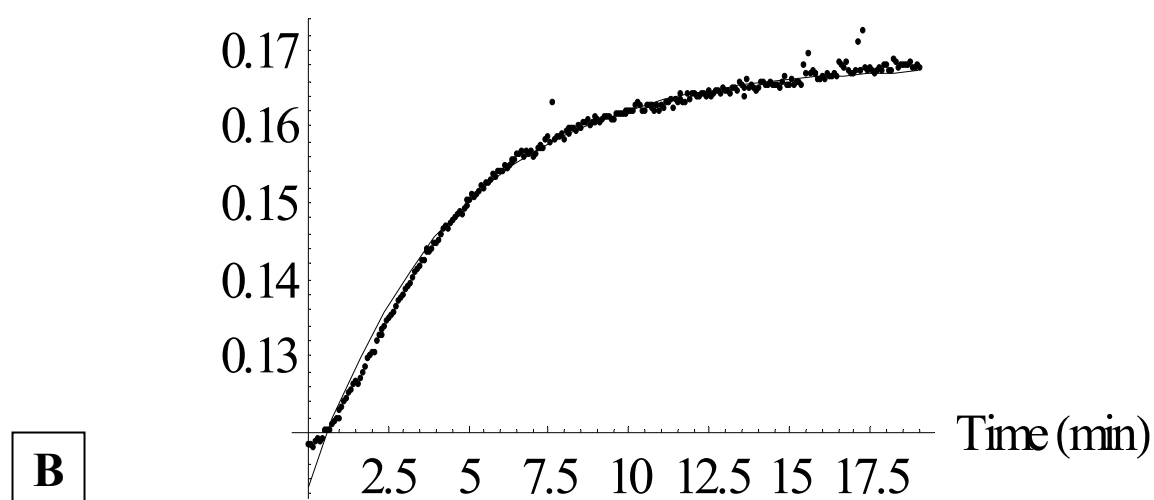
### 4.4.2.1 Uncertainty in Delay Calculations

There was some inherent error in delay calculations due to the speed at which the oxygen tanks in use could be switched. A breakout valve system was devised to make switch times shorter and more accurate, but human error and the need to prevent the

Combined Sensor Output A7 (V)



Combined Sensor Output A2 (V)

**Figure 4.2** Comparing Raw Data and Fit Curves

Two example plots are shown of individual sensor responses to an upward shift in exogenous oxygen. The raw data is represented by individual points and the curve fit determined by least squares regression in Mathematica is shown as a continuous line. (A) shows a smaller step with rapid resolution, where (B) shows a larger step with slower resolution. The time constant for the curve in (A) is larger. (B) also shows the slight S-shape at the beginning of the response curve common to many sensor responses.

These plots also allow closer observation of the noise (variance) of the sensor signal (Chapter 2). Noise for (A) is greater as a percentage of magnitude.

animal from becoming agitated often caused some uncertainty on the order of seconds about the actual time the new concentration was introduced. Thus the recorded delay times were only semi-quantitative.

#### 4.4.2.2 Delay Results

Delay averages for each animal ranged from  $12.8 \pm 9.3$  to  $142.6 \pm 49.5$  seconds, with an average of  $57.1 \pm 57.9$  seconds. There was little variation between delay times for sensors on a given array, but some sensors were seen to begin responses up to 3 time points ( $\sim 3$  seconds) before or after their fellows. Although the plot of delays versus the root of vasculature proximity not linear for all animals ( $R^2 = 0.5031$ ), removal of an outlier greatly increased linearity ( $R^2 = 0.9091$ ) (Figure 4.3). The outlier had a lower delay than expected, implying that a few close microvessels that were observed in this tissue may have been undervalued by the averaging process, underestimating the vascular access of this array. Modeling to determine the impact of lone microvessels on tissue oxygenation, and better methods of defining vascular proximity are suggested<sup>(41)</sup>.

Previous researchers' estimations for the delay between exogenous changes and changes in capillary oxygenation were less than 10 seconds<sup>(63)</sup>. This suggests that the majority of the delay seen here, up to 93%, was in the diffusive transfer of oxygen through the tissue and not in convective transfer or other processes.

Delays were observed to be systematically but not statistically longer, by  $14.7 \pm 12.6$  seconds, for lower concentrations of exogenous oxygen. In addition, delays for decreases in exogenous oxygen were on average far greater than those for increases in oxygen, roughly  $2.47 \pm 1.07$  times larger *in vivo*. There is some potential that together these findings may imply an oxygen-concentration dependent behavior of tissue mechanisms or vascular flow to the subcutaneous tissue. However, a more carefully controlled delay experiment would be warranted to substantiate these ideas.

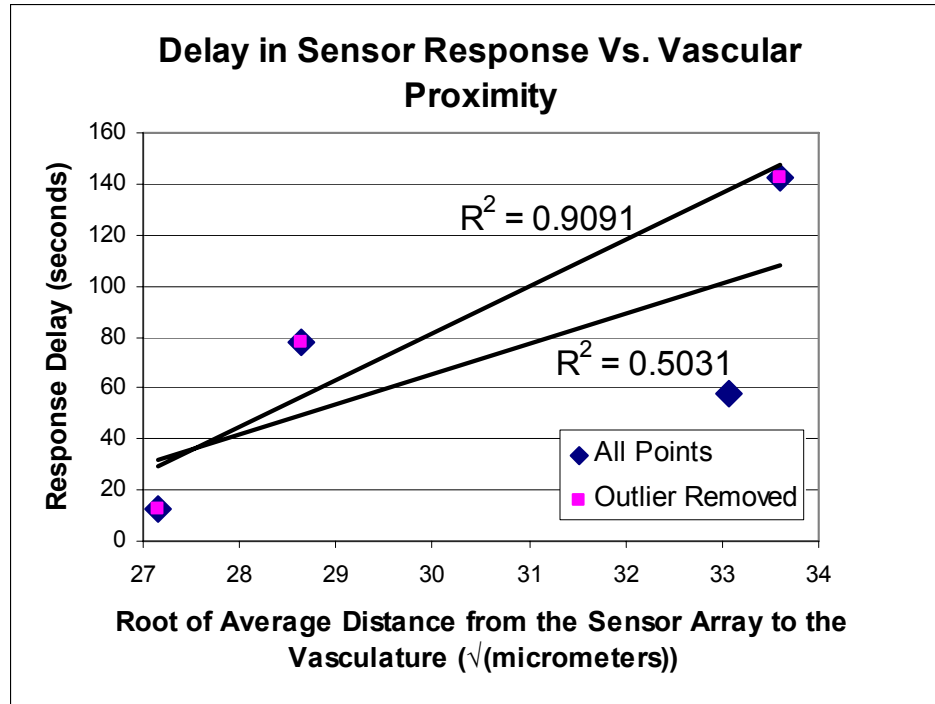


**Figure 4.3** Delay in the Sensor Response and Vascular Proximity

The delays between the introduction of a shift in exogenous oxygen concentration and the sensor response are shown plotted against the root of vascular proximity for each animal subject. The relationship is not substantially linear, as would be expected for purely diffusion limited situation, but removal of the low outlier increased linearity greatly. The low delay value of the outlier implies the presence of a few close microvessels, keeping the response time low, but not altering the average vascular proximity.

#### 4.4.3 Correlating Time Constants to Vascular Proximity

The average time constants for 4 of the 5 animals correlated well to vascular proximity (Figure 4.4). While the proportional relationship validates that the diffusion path dominates the time constant and therefore the rate of signal shift, the plot was not linear, indicating factors other than pure, homogenous diffusion. Specifically, the data fits the pattern for disproportionately higher equilibration to exogenous changes in thinner tissues due to either higher diffusion constants or differences in perfusion.

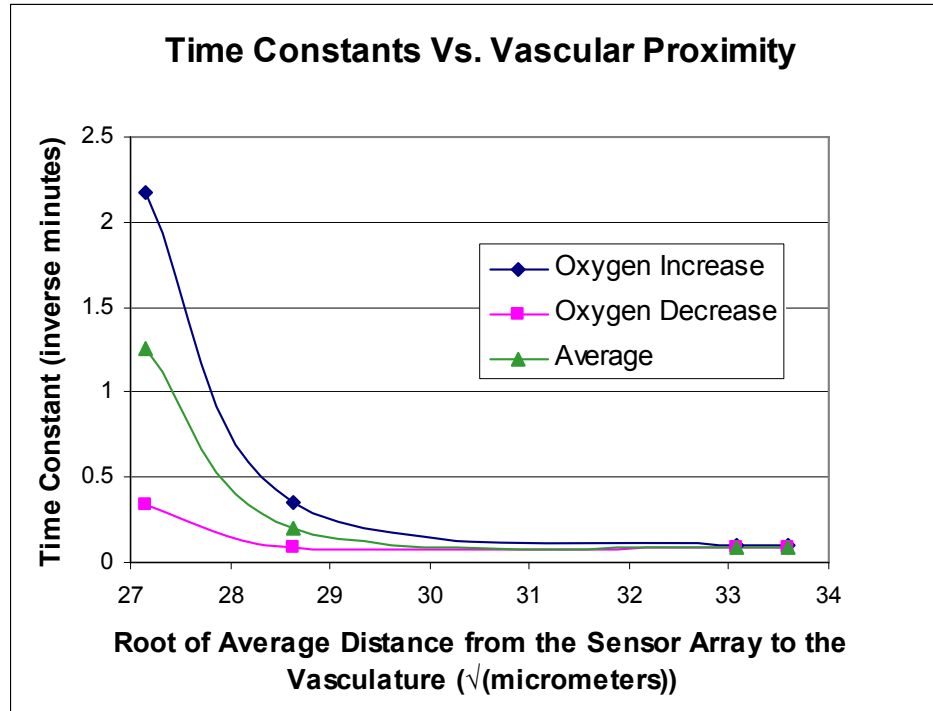


**Figure 4.4** Time Constants and Vascular Proximity

Calculated time constant values for each animal are shown plotted against the square root of vascular proximity. Curve shape is nonlinear, implying that more than diffusion distance contributes to the rate of curve resolution. Time constants for oxygen increases were distinct from that for decreases, but followed a similar curve form. Each point represents the average of 16 sensor measurements, 32 for the 'Average' series.

#### 4.4.4 Comparing Time Constants for Oxygen Increases and Decreases of Equal Step Size: The Shift-Directional Ratio

##### 4.4.4.1 In Vitro Shift-Directional Ratios

Time constants for step increases in oxygen were found in all cases *in vitro* and *in vivo* to be larger than those for an equal size step decrease in oxygen. The ratio (increase/decrease) of these time constants will be referred to as the Shift-Directional Ratio (SDR). For the calibration of bare sensors and biomaterials encased sensors, SDRs were  $1.18 \pm 0.14$  and  $1.18 \pm 0.14$  respectively. An  $SDR > 1$  indicates some resistance to oxygen loss that is not present for oxygen gain. The remarkable similarity of the *in vitro*

SDRs suggests that such a resistance to loss may exist in the sensor components, such as the hydrogel layer, that is not exhibited by the biomaterial membranes. The time constants for the *in vivo* experiments were very different with and without biomaterials, and very different for sensors encased in different biomaterials. Despite these differences, all *in vitro* measurements had the same SDR.

#### 4.4.4.2 In Vivo Shift-Directional Ratios

The SDRs for the day 14 *in vivo* oxygen challenges correlated well to the root of vascular proximity for each animal (Figure 4.5). SDRs increased with closer vasculature, and decreased with further vasculature, seeming to level off near a value of unity.

The average ratio for all electrodes in all 5 animals on day 14 was  $3.56 \pm 3.95$ . While the average time constant for all shifts in oxygen were much lower *in vivo* than *in vitro*, time constants for downward shifts in oxygen were disproportionately lower, increasing the SDRs.

The largest SDRs were for S0414, jumping from 1.18 *in vitro* to  $3.43 \pm 1.83$  on day 7 *in vivo*. By day 14 of the implantation, S0414's SDR had increased to  $7.82 \pm 5.46$ , due to both reduced time constants for oxygen decreases and increased time constants for oxygen increases, nearing *in vitro* values (Figure 4.6). S0414's extremely thin granulation and dermal tissues contributed to these observations and suggest that small amounts of tissue can actively resist oxygen loss, but do not work to prevent oxygen gain. Thicker tissues may still have only the same ability to resist loss, but a higher resistance to overall diffusion of oxygen reduces the rate at which oxygen increases can take place. Thus, it is most likely that the mechanisms involved are vascular, such as changes in vascular perfusion and functional capillary density.

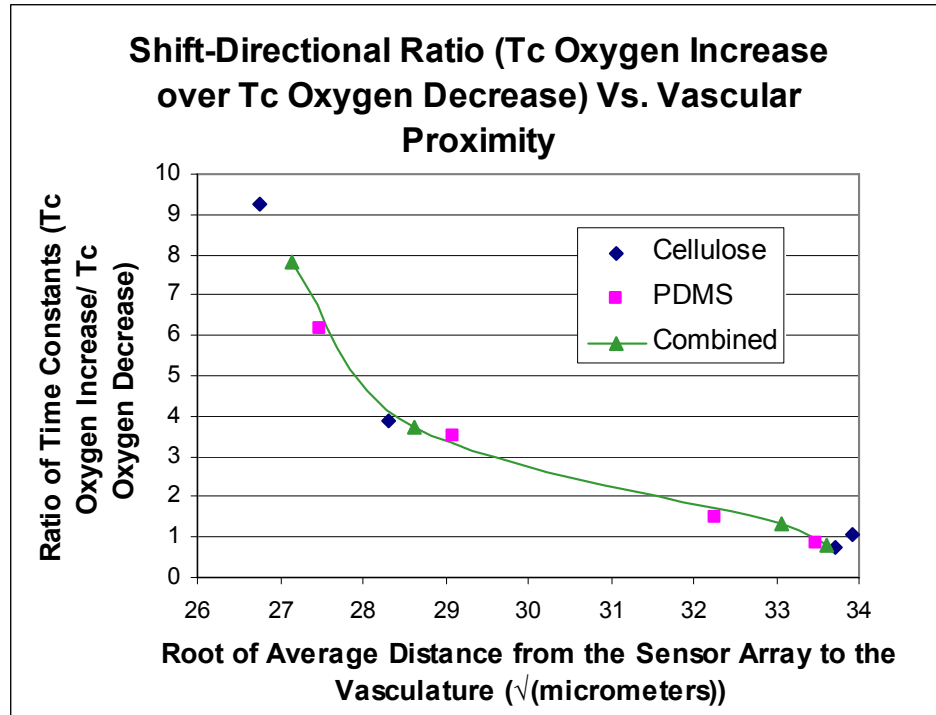


**Figure 4.5** The Shift-Directional Ratio and Vascular Proximity

The Shift-Directional Ratio plotted against the square root of vascular proximity, exhibiting a strong relationship in all animals. However, the shift-directional ratio was not seen to be dependent on the biomaterial encasing the sensor. The plot is not exactly linear,  $R^2=0.925$  for the closest fit linear trend, implying that other tissue factors may impact the ratio. The curve does not appear to level off as proximity increases, but does appear to head towards a value of 1 as proximity decreases.

#### 4.4.5 Correlating Dynamics to the Presence of Biomaterials

##### 4.4.5.1 Time Constants and Biomaterials

*In vivo* time constants for electrodes encased in cellulose were found to be lower on average than those for electrodes encased in PDMS, with a ratio of  $0.867 \pm 0.147$  (PDMS/cellulose,  $n=141$ ). Due to high variance, differences were only found to be statistically significant for 1 of 5 animals ( $P < 0.012$ ). However, when the comparison was further broken down to time constants for increases versus decreases in exogenous oxygen, greatly reducing variance, cellulose sensors had significantly lower time constants in 4 of the 10 *in vivo* cases ( $P < 0.037$  for 3 groups, and  $P < 0.084$  for the 4th).

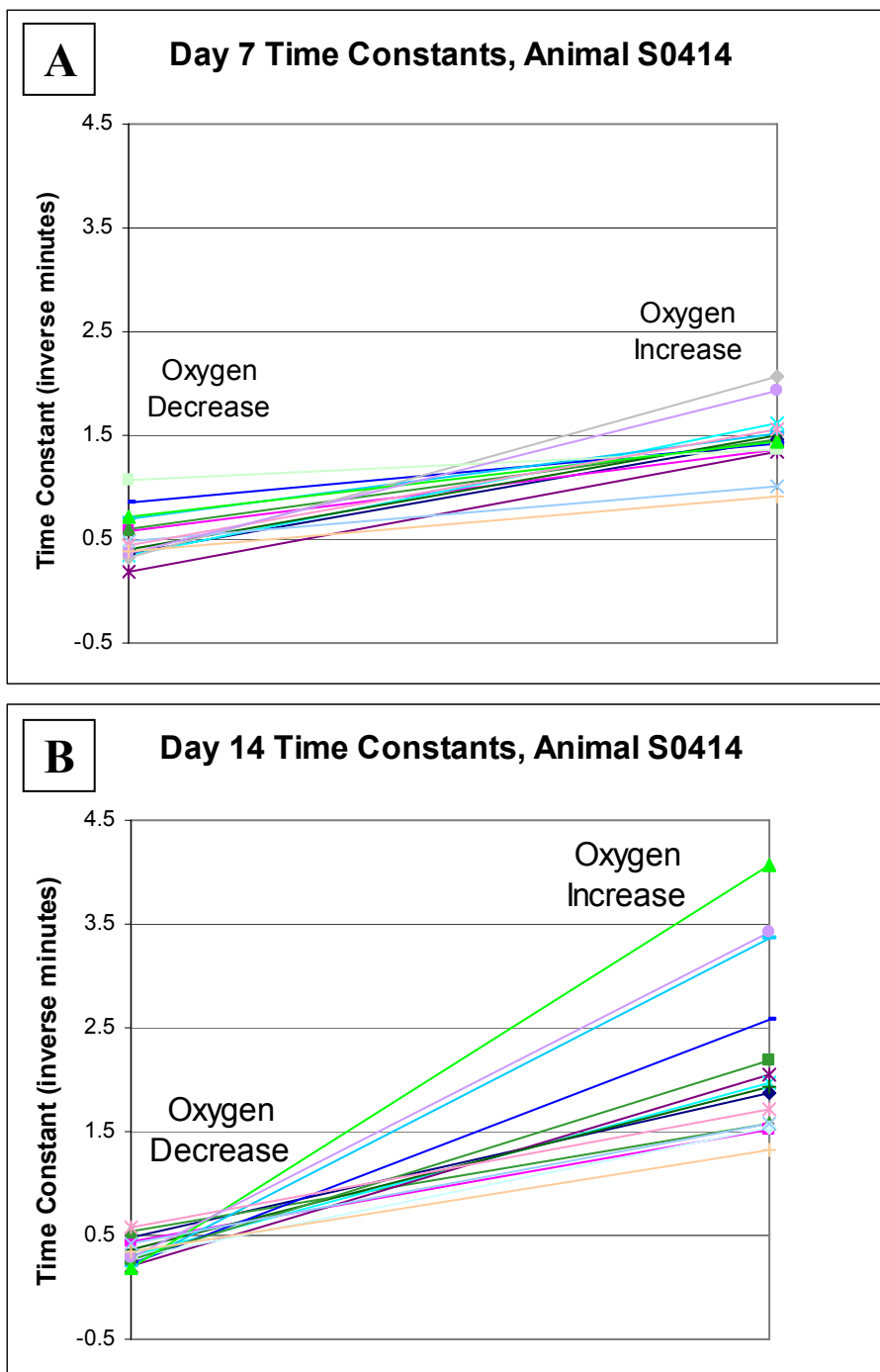


**Figure 4.6** Time Constant Changes from Day 7 to Day 14

(A) shows the average time constants for signal responses corresponding to both oxygen decreases and increases in 16 sensors on day 7 following implantation in animal S0414. (B) shows the time constants for the same sensors on day 14 following implantation. By day 14, there is a drop in time constants for oxygen decreases and a jump in the time constants for oxygen increases, both leading to higher shift-directional ratios.

#### 4.4.5.2 Biomaterials and Vascular Proximity

The results of higher time constants correlating to PDMS encasement appear to contrast with the findings in Chapter 6, that the distance from the membrane to the vasculature in tissues over cellulose were 17.9% shorter on average than for those over PDMS ( $P=0.129$ ), especially given that time constants were seen to correlate well to vascular proximity independent of biomaterials (Figure 4.7). However, time constants for *in vitro* calibrations of the electrodes encased in cellulose were found to be 4.88 fold smaller than those for PDMS, indicating that wet cellulose has a greater resistance to diffusion. *In vivo*, the impact of this higher diffusion resistance remains, but has either been diminished by ingrowth of the tissue into the cellulose, or by the relatively large diffusion resistance of the tissue. If thinner membranes of the same biomaterials were implemented, it is possible that the difference in vascular proximity elicited by cellulose may still be exhibited, but that the material itself would have a far lesser impact on diffusion, thus making microporous materials a potential better choice for optimizing sensor dynamic performance.

#### 4.4.5.3 The Effects of Biomaterials on the Sensor

Time constants for the post calibration of the sensor array, though higher than time constants calculated for the pre-calibration, showed no statistical difference in this change between sensors encased in different biomaterials, similar to observations in Chapter 3. This indicates that differences seen *in vivo* are due to biomaterials and tissue.

#### 4.4.6 Time Constant and Initial Magnitude Calculations for the Initial Signal Drop *In Vivo*: Effect of Biomaterials

Following sensor activation, a 20-30 long drop in signal magnitude was observed, far larger in time scale than transient signals seen in *in vitro* calibrations of the arrays and then previously observed for *in vitro* sensors<sup>(82, 131)</sup>.

The time constants calculated for S0414's drop in signal after sensor activation decreased an average of 67.2%, from  $0.73 \pm 0.74$  on day 4 to  $0.24 \pm 0.12$  on day 11 in animal S0414. Time constants started 4.27 times higher for cellulose encased sensor  $\tau$ 's than PDMS encased sensor  $\tau$ 's. The two groups saw a loss of 86% and a gain 1.7% respectively by day 11, significantly different ( $P < 0.012$ ) (Figure 4.8). Time constants for sensors encased in different biomaterials was significantly different on both days 4 and 11 ( $P < 0.020$  and  $P < 0.026$  respectively), indicating that at some point between days, the groups may have been similar.

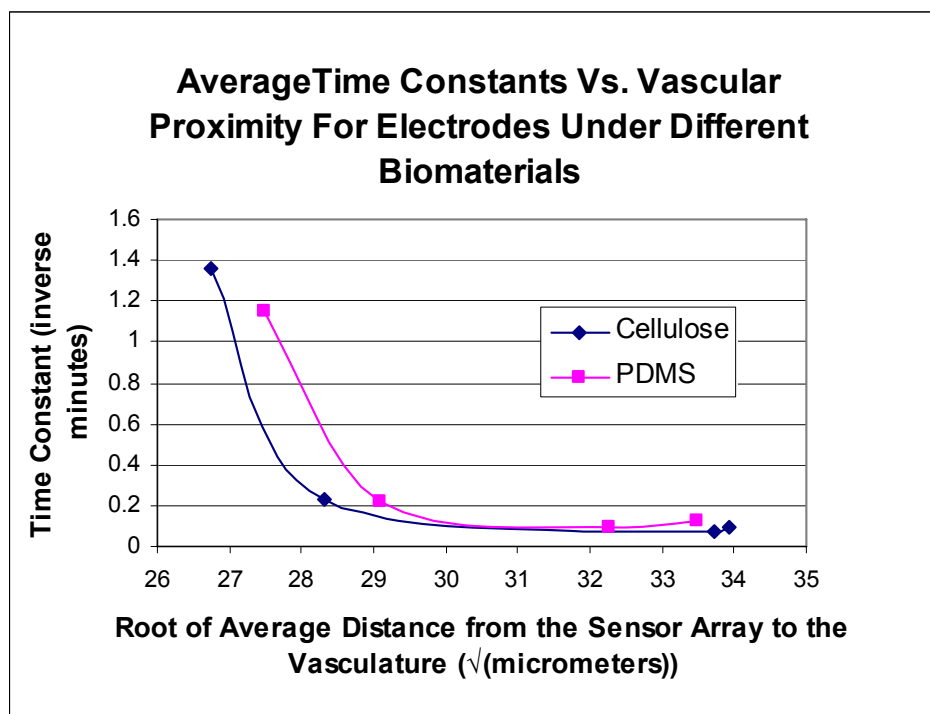


**Figure 4.7** Biomaterials, Time Constants, and Vascular Proximity

Calculated average time constants are shown plotted against the root of vascular proximity for each animal and each encasing biomaterial. The curve of time constants for electrodes encased in cellulose is distinctly lower from that for sensors encased in PDMS, but follows a similar curve form. Each point represents the average of 16 sensor measurements.

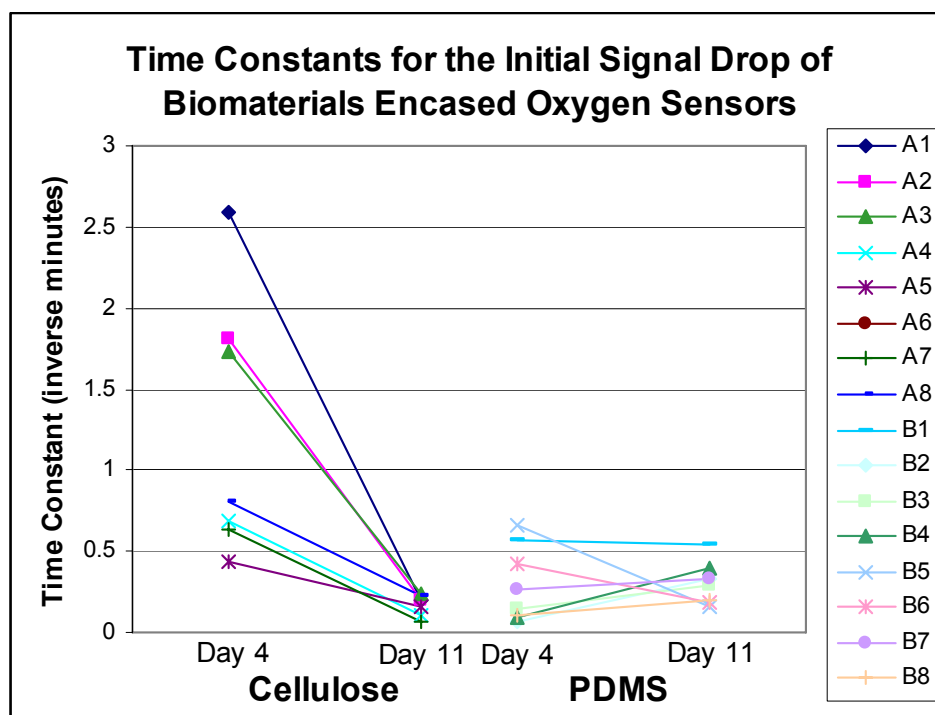


**Figure 4.8** Time Constants and the Initial Signal Drop *In Vivo*

Time constants are shown for the initial drop in sensor signal following its activation, on days 4 and 11 of implantation for animal S0414. The average magnitude and variance of the time constants for cellulose encased sensors (A) decrease by day 11, while those for PDMS encased sensors do not significantly change (B).

The change in the initial signal magnitude for each sensor, calculated by nonlinear regression, was highly dependent on the encasing biomaterial, falling  $63.2 \pm 33.5\%$  for cellulose and rising  $37.4 \pm 70.8\%$  for PDMS, a significant difference ( $P < 0.0048$ ) despite the high variation of the PDMS group, (Figure 4.9).

Higher initial signal magnitudes would suggest storage of higher concentrations of oxygen, increasing flux of oxygen at activation, while higher time constants suggest more accessible oxygen stores that were rapidly depleted. It is possible that the oxygen storage of the cellulose or its contents was initially high at first but was greatly reduced, while the oxygen storage in tissues adjacent to both materials increased, more so for tissue adjacent to PDMS, which had 17.9% longer tissue diffusion distances on average.

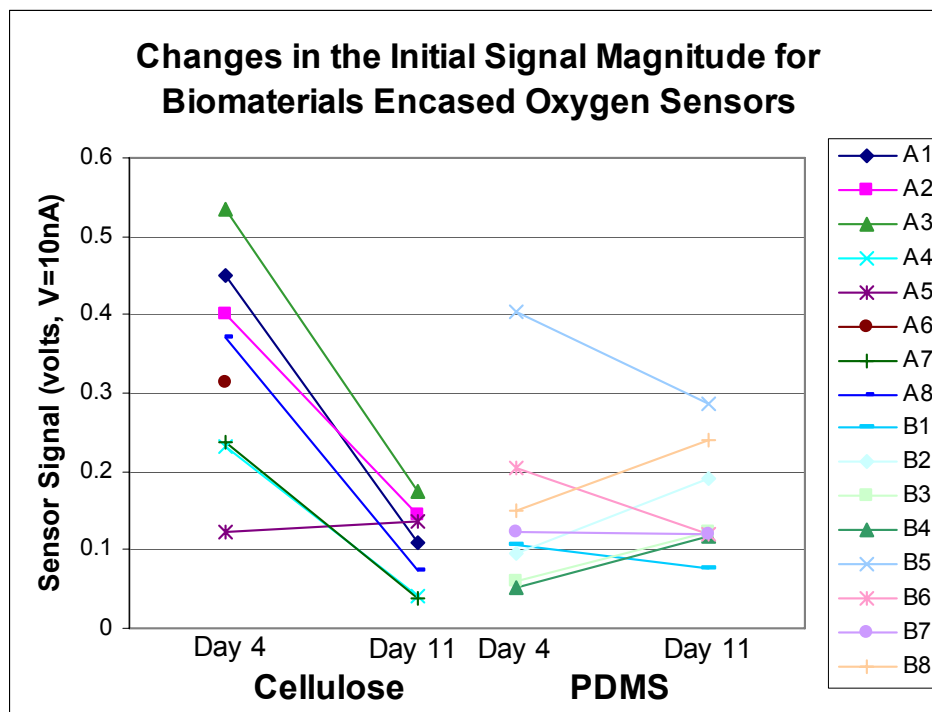


**Figure 4.9** Biomaterials and Transient Initial Signal Magnitude

The calculated initial magnitudes for the initial drop in signal are shown for both cellulose and PDMS encased sensors on days 4 and 11 following implantation. While the cellulose encased sensors had a much reduced initial signal magnitude by day 11, possibly due to the ingrowth of tissue, the PDMS encased sensors experienced an increase in initial signal magnitude.

Final signal magnitudes for the sensors rose  $10.0 \pm 28.2\%$  from day 4 to 11 for all sensors, supporting the theory of increased oxygen storage or flux. Histological observations described in Chapter 6 also showed that the tissue had completely penetrated S0414's cellulose leaving a thin layer of dense connective tissue and cells. This supports the explanation that the oxygen storage of cellulose changed during implantation.

#### 4.4.7 Estimating the Diffusion Constant

Using the calibrations of arrays with biomaterials, the diffusion constant in PDMS was estimated to be  $2.15 \times 10^{-5} \text{ cm}^2/\text{s}$ , on par with values from the literature<sup>(28, 96)</sup>. However, the sensor hydrogel layer was not accounted for, which implies that true values may be higher. Using the estimated  $\text{DO}_2$  for PDMS and Equation 4.3, the diffusion constant in cellulose was found to be  $4.41 \times 10^{-7} \text{ cm}^2/\text{s}$ .

Estimates of the diffusion constants for the array environment, combining the material membranes and the tissue, varied for each animal from  $1.04\text{--}8.10 \times 10^{-5} \text{ cm}^2/\text{s}$  (Table 4.1). The large outlier value was again for S0415, and the average of the remaining values was  $1.91 \pm 0.86 \times 10^{-5} \text{ cm}^2/\text{s}$ . These values are within the expected order of magnitude for tissue diffusion constants seen by previous investigators in the hamster skinfold and similar muscular tissues<sup>(15, 16, 129, 145)</sup>. However, when the  $\text{DO}_2$  of tissue in the preparations was calculated by factoring out the contribution of the biomaterial membranes, unrealistic values were obtained, indicating that the diffusion constants of the biomaterials may have increased from their *in vitro* values. Alternately, *in vitro* values may have been underestimated due to excess moisture on the membrane surfaces.

With better histology and biomaterial characterization, there is a potential use of sensor dynamics in determining the tissue diffusion constant *in vivo*.

#### 4.4.8 Limitations of the Histology and Future Directions

The outlier for all proximity calculations, S0415's average distance to vasculature was the highest at  $591.2 \mu\text{m}$ , but a few close capillaries around muscle fibers may have increased the time constants for this animal to 0.397, the second highest observed average. In addition, evidence of fluid presence or hemorrhage was found in S0415's

tissue which could have affected diffusion. This latter observation was the driving force for removing S0415 from most calculations.

**Table 4.1** Oxygen Diffusion Constants for the Array Environment

Diffusion constants to the array are estimated for each animal, using average time constants and vascular proximity. The diffusion path accounts for the distances in the tissue as well as the membrane thickness, which was relatively constant.

<b>Table 4.1 Estimated Oxygen Diffusion Constants for the Array Environment</b>			
<b><u>Animal Subject</u></b>	<b><u>Diffusion Path (cm<sup>2</sup>)</u></b>	<b><u>Time Constant</u> <b>15.0→10.0% O<sub>2</sub> (min<sup>-1</sup>)</b></b>	<b><u>DO<sub>2</sub> (10<sup>-5</sup> cm<sup>2</sup>/s)</u></b>
S0411	0.01275	0.089044	1.89
S0414	0.00543	0.340499	3.08
S0416	0.00672	0.0925	1.04
S0417	0.01196	0.082003	1.63
<b>Combined S0411-S0417</b>			<b>1.91±0.86</b>
S0415	0.01668	0.291318	8.10

It should be noted that the presence of capillaries in the granulation tissue could not be absolutely determined due to the absence of suitable hamster antibody stains, the failure of enzyme activity stains, and a thaw defect that occurred with the frozen histology. These issues are discussed in Chapter 6. As well, a site relatively devoid of large venules and arterioles was chosen with the intention of creating an initially evenly oxygenated preparation. For the most part, capillaries surrounding retractor muscle fibers constituted the nearest identifiable vasculature.

For the benefit of future work, anti-hamster antibodies for targets such as endothelial cell CD-31 marker are currently being tested. These may improve the identification of vasculature for future studies.

## 4.5 Conclusion

Time constants for electrode curves were found to be well correlated to the sensor's access to vasculature, with faster signal resolution for closer microvessels. However, the extreme curvature of the relationship implied that thinner tissues may have had distinctly higher diffusion rates. Delays between challenges and sensor responses showed similar correlation, with outliers tending to have lesser delays, perhaps due to a few undetected microvessels close to the biomaterial membrane surface. Cellulose encasement reduced sensor time constants, to a much lesser extent *in vivo* than *in vitro*, but with visible effects even after 14 days of implantation.

Time constants were consistently higher for increases in oxygen versus decreases. The shift-directional ratio *in vitro* was the same for both bare sensor arrays and those encased in biomaterials, implying that biomaterials do not inherently affect this ratio. However, the ratio was, on average, 3.02 times larger *in vivo*, and correlated very cleanly to vascular proximity. These results both suggest that the tissue, most likely the local vasculature plays a role in buffering against hypoxia, and that implanted sensors are a potential method of studying these phenomena.

Overall, this study validates the dynamics of sensor signals as a valuable part of assessing sensor performance. Time constants were demonstrated to be a simple representation of sensor dynamics, utilizing empirical *in vitro* and *in vivo* data as well as quantified histology. Between the correlation of time constants and the shift-directional ratio to vascular proximity, artificial oxygen challenges are strongly suggested as a means for non-invasively determining the access of implanted sensors to vasculature.

Calculations of diffusion constants for the array environment were similar in magnitude to those expected from material and tissue values in the literature, but estimation of tissue  $\text{DO}_2$  was not successful, due to possible changes in the diffusion

through the biomaterials *in vivo*. More carefully controlled experimentation would be needed to use the implanted sensor as a measure of tissue DO<sub>2</sub>.

This study encourages future work on *in vivo* dynamics for other analytes, such as glucose and lactate, particularly with regards to biomaterials. Alternate methods of challenges, such as ischemia or hyperoxia, would provide a more specific understanding of which tissue mechanisms affect dynamics and how biomaterials affect these mechanisms.

## CHAPTER 5: Biomaterials and the Response to Hypoxia and Oxygen Challenges

### 5.1 Abstract

Sensor performance was measured in response to several dynamic oxygen challenges with and without a dual biomaterial membrane *in vitro* and with a dual membrane *in vivo*. The challenges took the form of short term hypoxic exposure and repeated cycles of oxygen decreases and increases.

Following hypoxia, sensor signals in bare arrays did not return to their former magnitudes, but resolved at lower values. The effect was reversible by extended exposure to higher oxygen levels. With the biomaterial membranes, these effects were greater, with an average  $8.85 \pm 2.68\%$  loss of signal magnitude following an 80% reduction in oxygen concentration. Cellulose encased sensors experienced significantly greater signal loss than PDMS encased sensors ( $P < 0.0011$ ). Loss and gain of dissolved oxygen in the materials and fluids of the sensor may have contributed to these phenomena by creating a temporary imbalance in flux, even in the short diffusion path of the bare arrays. *In vivo*, loss of signal magnitude following hypoxia was greater,  $15.73 \pm 12.88\%$  with a 28% reduction in oxygen, but with no significant difference in biomaterials. Signal loss was significantly greater on day 14 than day 7. Continued loss of signal magnitude was observed with repeated oxygen challenge cycles.

The time constants for *in vivo* sensor response curves were observed to increase following hypoxic shifts. Time constants also increased on subsequent cycles of the repeated oxygen challenges. *In vitro*, where no oxygen dependent mechanisms are assumed to exist, time constants actually decreased with rapid repeated cycles of oxygen challenge.

These results indicate that signal magnitude and dynamics are both dependent on oxygen history, and that the tissue response can affect this dependence.

## 5.2 Introduction

Many elements of physiology exhibit active responses to metabolic challenges. In particular, the short and long term reactions of cells and tissue to oxygen fluctuation and hypoxia is an important phenomena to wound healing and device implantation<sup>(34, 63, 115, 120)</sup>. Biosensors are inherently likely to be in environments experiencing variable oxygen flux, and thus their designs should take into account the effect of dynamic change on performance. In addition, it should be considered how the response of the tissue to the device implantation and to the implant materials affects these changes.

This study examined the effects on sensor magnitude and rate of response of short term hypoxia and of repeated cycles of oxygen decreases and increases. For the purposes of the study, normoxic levels were considered to be those at room air, or 20.9% oxygen. A shift to lower oxygen and back, for example 15.0→10.0→15.0%, is referred to as a hypoxic exposure. Hyperoxia was never introduced, but in several instances, measurements are made at 15.0% oxygen following shifts to and from 20.9% oxygen. In these situations, the shift is referred to as an exposure to elevated oxygen.

## 5.3 Materials and Methods

### 5.3.1 *In Vitro* Data Collection: Bare Arrays

During *in vitro* calibrations (Chapter 3) of several bare arrays, sensors had three separate experiments performed on them for hypoxic exposure.

- 1.) 20.9→2.0→20.9% exogenous oxygen, a simple hypoxic exposure.

2.) 20.9→2.0→15.0→20.9%, hypoxic exposure with interim equilibration.

3.) 10.0→2.0→10.0%, a smaller scale hypoxic exposure.

The *in vitro* multi-cycle challenges were performed on one array, starting at 20.9%, then following the pattern, (2→10→15→), three times (Figure 5.1).

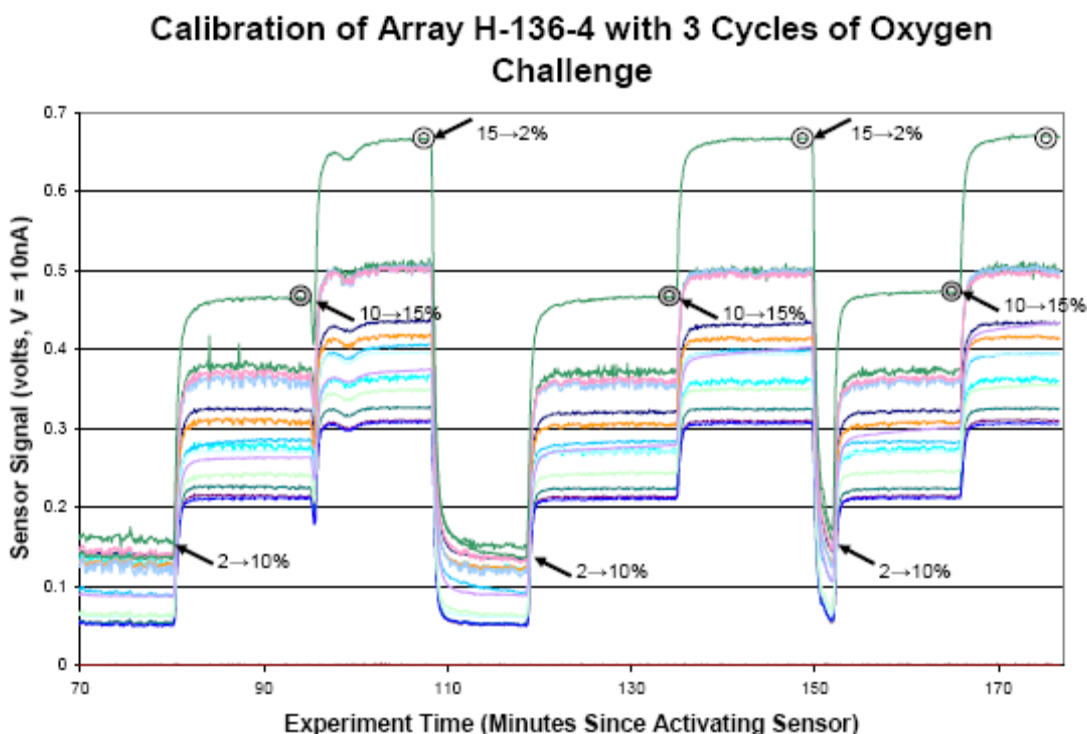


**Figure 5.1** *In Vitro* Calibration of a Bare Sensor Array: 3 Cycles of Hypoxic Challenges  
The signal magnitudes for 16 oxygen sensors of a planar array are plotted against time. The array is exposed to 3 cycles of oxygen challenge, with increases in oxygen indicated by upturned arrows and decreases indicated by downturned arrows. The initial and final concentrations of each shift in exogenous oxygen are noted at the arrows. The times at which measurements of signal magnitude were made are noted by colored rings on an example sensor signal. The grey rings denote measurements at 10.0% exogenous oxygen, and the white rings measurements at 15.0%. Time constants were measured for each shift in oxygen, beginning at an arrow, and ending at a ring.

For the three single shift experiments, the signal magnitude was measured (Chapter 2) before and after the exposure for comparison. For the multi-cycle challenge, signal magnitudes were collected at 10.0 and 15.0% oxygen for each cycle.

### 5.3.2 *In Vitro* Data Collection: Arrays with Biomaterials

During *in vitro* calibrations of several arrays encased in their biomaterial membranes, sensors had their signal magnitudes measured before and after a 10.0→2.0→10.0% hypoxic exposure. Loss of signal magnitude was compared for sensors encased in different biomaterials.

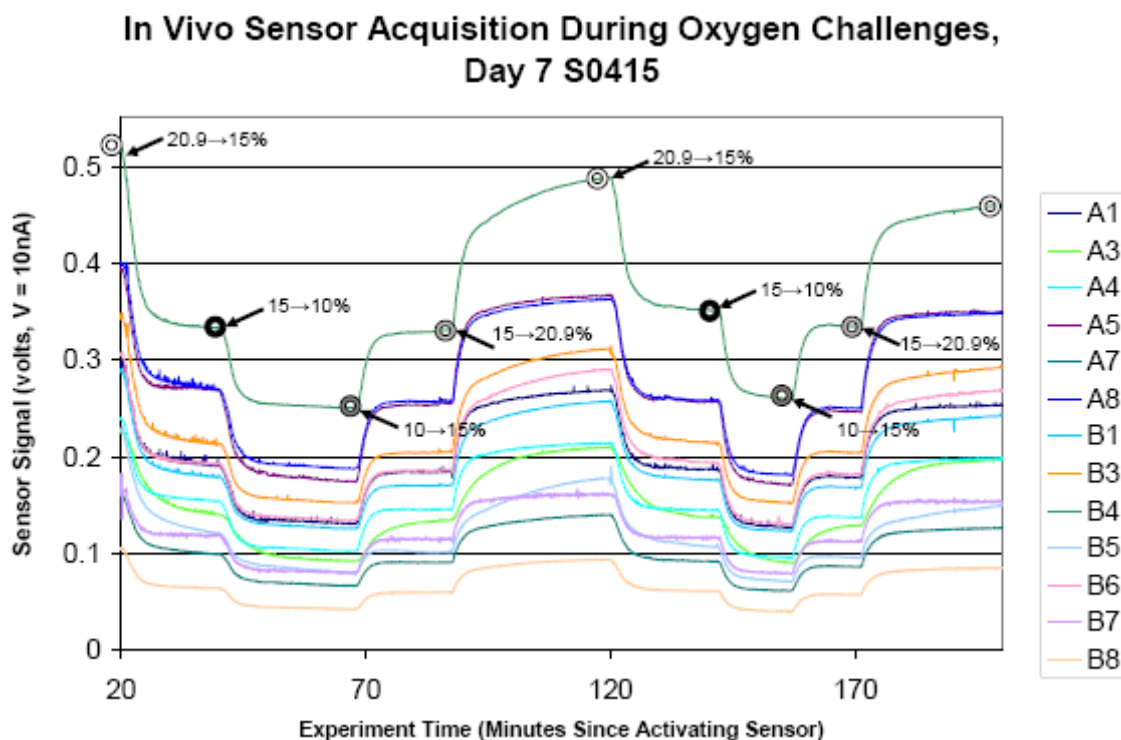


**Figure 5.2** *In Vivo* Acquisitions of 16 Oxygen Sensors: 2 Cycles of Hypoxic Challenges  
The signal magnitudes for 16 oxygen sensors of a planar array are plotted against time. The array is exposed to 2 cycles of oxygen challenge, with increases in oxygen indicated by upturned arrows and decreases indicated by downturned arrows. The arrows indicate the beginning of a shift in the exogenous oxygen mixture, with the initial and final oxygen levels noted. Rings are shown to denote the time at which signal magnitudes were measured and are further described in (Table 5.3). Time constants were measured for each shift in oxygen, beginning at an arrow, and ending at a ring.

### 5.3.3 *In Vivo* Data Collection

For all animals on days 7 and 14 following implantation of the sensor array and biomaterial membranes, signal magnitude was measured before and after two types of hypoxic exposures: 1.) 20.9→15.0→20.9%, and 2.) 15.0→10.0→15.0%.

On day 7, for animals in good temperament, the hypoxic challenge cycle (Chapter 4 methods), 20.9→15.0→10.0→15.0→20.9%, was repeated two full times consecutively (Figure 5.2), constituting the multi-cycle challenge. Signal magnitudes were measured at each exogenous oxygen level. The length of these experiments and comfort of the animal allowed only two of these experiments to be performed.

### 5.3.4 Sensor Dynamics: Time Constants

Time constants were calculated (Chapter 4) for each shift from 10.0 to 15.0% exogenous oxygen during the bare array multi-cycle challenge. Time constants were calculated for all shifts of exogenous oxygen for the *in vivo* multi-cycle oxygen challenges.

### 5.3.5 Data Analysis and Statistical Methods

Loss or gain of signal magnitude was determined as a percentage of the original magnitude. The sensor magnitudes and time constants were compared for each cycle of the multi-cycle challenge using ANOVA methods. Other two group comparisons were made using paired t-testing with the assumption of unequal variance.

## 5.4 Results and Discussion

### 5.4.1 Hypoxic Exposure and Signal Magnitude

#### 5.4.1.1 Hypoxia and the Bare Sensor Array

Changes in signal magnitude for the three single cycle experiments are shown in (Table 5.1). The signals measured at 20.9% with exposure to 2.0% lost significantly less magnitude when allowed to equilibrate at 15.0% before returning to 20.9% ( $P < 0.054$ ). Signals measured at 10.0% with exposure to 2.0%, lost significantly more magnitude than the signals at 20.9% with the 2.0% exposure and 15.0% equilibration ( $P < 0.000293$ ,  $n = 59$ ), but did not lose significantly more magnitude than for the 20.9% measurements with simple 2.0% exposure.

**Table 5.1** Changes in Signal Magnitude *In Vitro* Following Hypoxic Exposure  
Values are given as the change in signal magnitude as a percent of original magnitude.

<b>Table 5.1: The Bare Sensor Array, Changes in Sensor Signal Magnitude Following Hypoxic Exposure</b>		
<u>Oxygen Levels</u>		
<u>Measurement Level</u>	<u>Intervening Hypoxic Exposure</u>	<u>Change in Magnitude</u>
20.90%	2.0%	-2.26±3.07
20.90%	2.0, then 15.0%	-0.37±1.66
10.0%	2.0%	-2.98±2.76

For the experiment with three full cycles, the signal magnitudes did not change significantly from cycle to cycle (Figures 5.1 and 5.3). However, the first signal was collected following a period of 2.0% oxygen, so the signal magnitude may have already dropped by as much as was possible prior to this measurement.

A possible explanation for the loss of signal magnitude following hypoxia is based on the linear relationship between oxygen concentration in aqueous media and

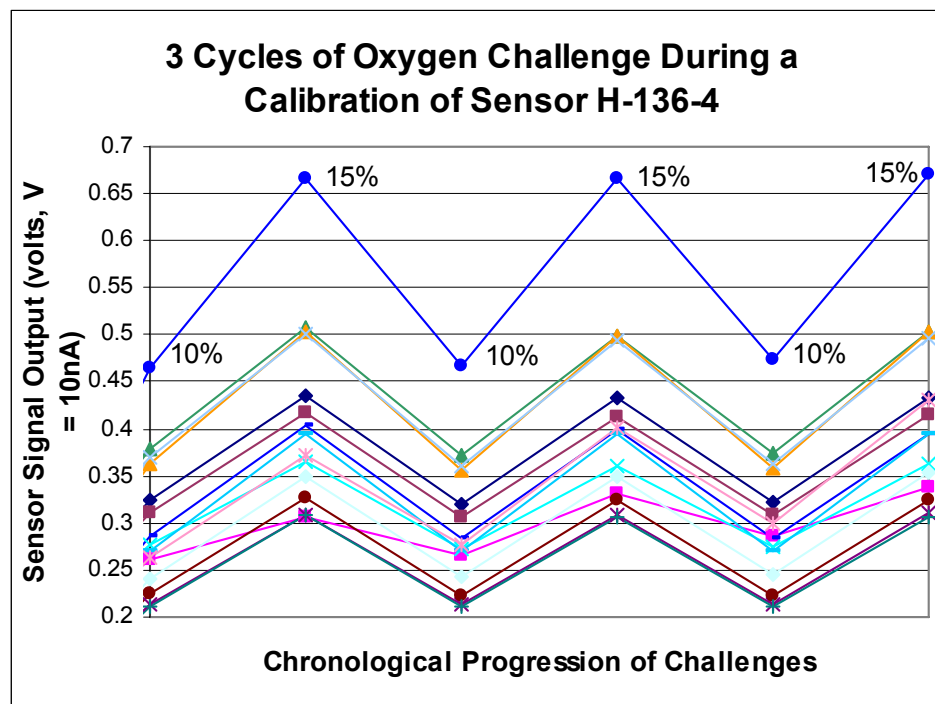


**Figure 5.3** Signal Magnitudes for 3 Cycles of *In Vitro* Oxygen Challenges

The signal magnitudes taken at 10.0 and 15.0% exogenous oxygen are compared for three cycles of oxygen challenge during a sensor array calibration. The values for the 16 sensors are relatively stable, not changing significantly from one cycle to another.

the exogenous partial pressure of oxygen (Henry's Law). The results show that more extreme hypoxia caused a greater loss of signal magnitude, and that the effects were observed to be reversible with exposure to elevated oxygen. Both support the possibility of changes in dissolved oxygen which could have temporarily disrupted the flux balance, lowering the sensor signal. While some elements of the calibration apparatus may retain oxygen, such as the fluid media in the calibration flask, the timescale of the changes that were observed, their rapid reversibility, and the clean exponential form of the signal shifts, imply a smaller closer source than the flask media such as the hydrogel layer, the hydrophobic membrane, or adsorbed moisture.

There was no clear relationship between signal loss and the oxygen concentration at which measurements were taken, only dependence on the size of the hypoxic shift.

#### 5.4.1.2 Hypoxia and the Sensor Array with Biomaterials

The loss of signal magnitude seen following a hypoxic challenge was much greater with the biomaterial membrane in place. Sensor signals measured at 10.0% oxygen, with intervening 2.0% exposure, lost an average of  $-8.85 \pm 2.68\%$  magnitude. The average loss for sensors encased in cellulose was  $-12.79 \pm 2.95\%$ , significantly larger than the average loss for those encased in PDMS,  $-5.17 \pm 2.78\%$  ( $P < 0.0011$ ).

PDMS is known to have some solubility for oxygen, but far less than water. Thus its solvation of oxygen may be augmented by water vapor retention. Solubility of oxygen in cellulose will also be due largely to the aqueous buffer it retains. Assuming solubility is constant throughout the membrane volume, the cellulose had a 5.91 fold greater impact than PDMS on signal loss, creating a greater temporary flux imbalance. While medical applications would utilize thinner membranes, those requiring higher accuracy should take material oxygen solubility into account when designing for dynamic environments, also considering the fluid and vapor retention of these materials.

#### 5.4.1.3 Hypoxia In Vivo: Single Exposures

Table 5.2 shows the change in signal magnitudes *in vivo* at 20.9% and 15.0% exogenous oxygen, following short term hypoxic exposure. All measurements showed a loss of signal, greater on day 14 than day 7 ( $P < 0.018$ ,  $n = 273$ ), but almost identical for sensors encased in different biomaterials. Loss was larger than seen *in vitro* with biomaterials by a factor of 1.96, suggesting the tissue stores equivalent oxygen or alternately that the lower flux experienced *in vivo* was easier to perturb. Signal loss did not appear to correspond to vascular proximity (Chapter 4 methods). One animal, S0415, lost far less signal. Histological observations of the animal's tissue showed strong evidence of hemorrhage, fluid retention, and loose red blood cells. Thus, the hypoxia may have not fully depleted the potentially considerable stores of oxygen in this tissue.

**Table 5.2** Changes in Signal Magnitude *In Vivo* Following Hypoxic Exposure  
Change in magnitude as a percent of original signal magnitude following hypoxic exposure is shown for all animals on days 7 and 14 following implantation, with standard deviations. Changes with respect to biomaterial encasement are also shown. The increase in the sensor signal loss on day 14 versus 7 should be noted.

<b>Table 5.2: The Sensor Array with Biomaterials <i>In Vivo</i>, Changes in Sensor Signal Magnitude Following Hypoxic Exposure</b>					
<u>Days Following Implantation</u>	<u>Oxygen Levels</u>		<u>Change in Magnitude</u>		
	<u>Measurement Level</u>	<u>Hypoxic Exposure</u>	All Sensors	Cellulose Encased	PDMS Encased
7	20.9%	15.0%	-14.90±9.10	-14.30±8.77	-15.47±9.52
	15.0%	10.0%	-12.58±10.27	-13.29±11.62	-11.89±8.92
	Combined		-13.74±9.73	-13.80±10.22	-13.68±9.32
14	20.9%	15.0%	-16.74±16.51	-15.59±18.51	-17.91±14.33
	15.0%	10.0%	-17.96±12.92	-19.30±14.40	-16.55±11.18
	Combined		-17.34±14.80	-17.45±16.58	-17.24±12.80
All Days	20.9%	15.0%	-15.91±13.69	-15.02±14.94	-16.80±12.35
	15.0%	10.0%	-15.54±12.06	-16.66±13.50	-14.40±10.39
	Combined		<b>-15.73±12.88</b>	<b>-15.84±14.21</b>	<b>-15.61±11.44</b>

**Table 5.3** Changes in Signal Magnitude *In Vitro* Between Cycles of Oxygen Challenges  
Changes in signal magnitudes between the two cycles of a multi-cycle oxygen challenge are shown at all oxygen concentrations. Measurements were not made immediately before and after a single exposure, but rather at the same position in each cycle. The measurements are marked by colored rings on the plot of one example sensor in Figure 5.2. Here, the intervening oxygen level is defined as the hypoxic or elevated exogenous oxygen level the sensor was most recently exposed to.

<b>Table 5.3: The Sensor Array with Biomaterials <i>In Vivo</i>, Changes in Sensor Signal Magnitude Between Cycles of a Multi-Cycle Oxygen Challenge</b>					
<u>Figure 5.2 Marking</u>	<u>Oxygen Levels</u>		<u>Change in Magnitude</u>		
<u>By Ring Color</u>	<u>Measurement Level</u>	<u>Intervening Level</u>	All Sensors	Cellulose Encased	PDMS Encased
Light Grey	15.0%	10.0%	-10.17±7.54	-8.11±5.75	-12.14±9.20
White	20.90%	15.0%	-7.97±1.42	-7.22±2.31	-8.81±2.17
Dark Grey	10.0%	15.0%	-7.39±6.74%	-6.39±5.31%	-8.36±8.14
Black	15.0%	20.9	1.34±1.77	0.49±1.18	2.32±2.18

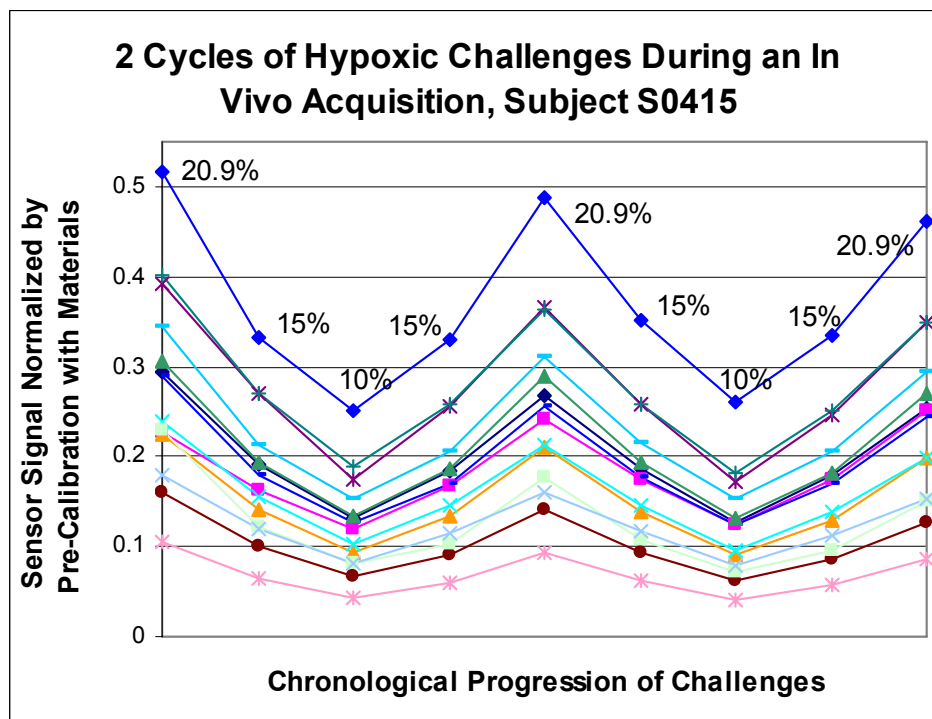


**Figure 5.4** Normalized Signal Magnitudes for 2 Cycles of *In Vivo* Oxygen Challenges. Measured signal magnitudes are compared for two cycles of an *in vivo* oxygen challenge on the 7<sup>th</sup> day following implantation of the sensor array with biomaterials. Magnitudes at each oxygen level, 10.0%, 15.0%, and 20.9% oxygen dropped from the 1<sup>st</sup> to the 2<sup>nd</sup> cycle, except for those at 15% immediately following exposure to 20.9% oxygen, which rose slightly. Normalization was to pre-calibration of the array with biomaterials.

#### 5.4.1.4 Hypoxia In Vivo: Multi-Cycle Oxygen Challenges

For the multi-cycle oxygen challenges, signal magnitudes from the first to the second cycle dropped for all measurements at 20.9% and 10.0% exogenous oxygen (Table 5.3) (Figure 5.4). The signals measured at 15.0% oxygen also lost magnitude following exposure to 10.0%, but with elevated 20.9% oxygen intervening, magnitudes actually increased, with high significance for a difference between these two groups ( $P < 1.28 \times 10^{-7}$ ). This last result, where change in signal magnitude was dependent on the levels of intervening oxygen exposure, was consistent with the *in vitro* results, indicating strongly that the biomaterials and the tissue have a depletable store of oxygen, or that oxygen dependent tissue mechanisms were activated such as changes in cellular oxygen

metabolism, or changes in functional capillary density, vascular tension or flow rate, or hemoglobin saturation. Most sensor signals lost magnitude from cycle to cycle, even the measurements at 10.0% oxygen, further indicating changes in the tissue that may affect flux and flux balance. Careful experiments relating changes in dissolved oxygen to changes in exogenous oxygen may be a potential method of estimating the solubility coefficient of the tissue.

The change in signal magnitude between cycles was systematically, but not statistically larger for cellulose encased sensors than PDMS encased sensors *in vivo*. Tissue effects on oxygen flux during challenges may have largely outweighed the effects of the materials.

As was also observed *in vitro*, no pattern was established relating changes in signal magnitude to the oxygen levels at which the measurements were taken.

## **5.4.2 Hypoxic Exposure and Time Constants**

### **5.4.2.1 Time Constants and In Vitro Multi-Cycle Challenges**

For the *in vitro* multi-cycle oxygen challenges, the average time constants decreased from each cycle to the next, losing  $4.92 \pm 11.50\%$  from the first to the second cycle, and  $14.12 \pm 12.34\%$  from the second to the third cycle, a total loss of  $20.47 \pm 10.98\%$  (Figure 5.5). An ANOVA test of the time constants for each cycle showed a significant difference ( $P < 0.011$ ), and t-tests between the last two cycles showed their time constants to be significantly different ( $P < 0.020$ ). While the initial and final signal magnitudes are virtually identical (Figures 5.1 and 5.3), the response to shifts in oxygen took longer to resolve. The most likely reason is reduced hydration or altered osmolarity of the sensor hydrogel, or changes in the adsorbed moisture on the sensor face. Even given the short duration of the calibration, hydration may have had an effect on sensor performance.

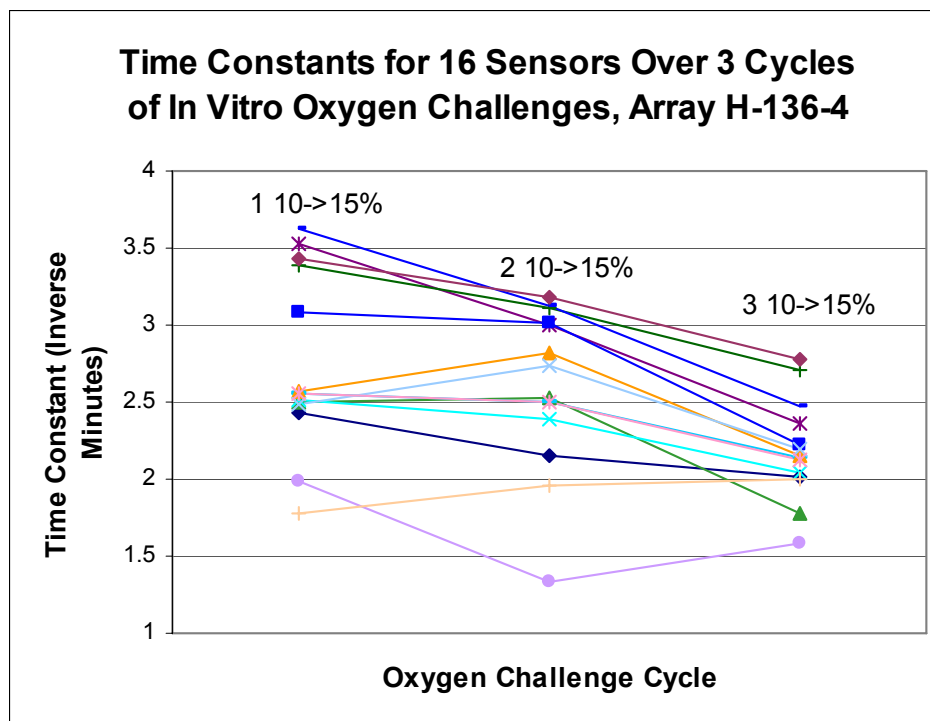


**Figure 5.5** Time Constants for Three Cycles of *In Vitro* Oxygen Challenges

#### 5.4.2.2 Time Constants and In Vivo Multi-Cycle Challenges

For the multi-cycle *in vivo* oxygen challenges, time constants were seen to increase significantly from the first cycle to the second ( $P < 0.013$ ,  $n = 112$ ) (Table 5.4) (Figure 5.6). Time constants for the shift from 20.9% exogenous oxygen to 15.0% showed the least increase between cycles, significantly different than for the other shifts ( $P < 1.2 \times 10^{-9}$ ). This correlates well to the results for changes in signal magnitude, where this was the only data point to increase. The difference in time constant values from the 1<sup>st</sup> to the 2<sup>nd</sup> cycle was significant for the shift from 15.0 to 10.0% exogenous oxygen and the shift from 15 to 20.9% ( $P < 2.09 \times 10^{-5}$  and  $P < 0.033$  respectively), but was not seen to be significant for the other two shifts. Increases in time constants were far greater than those expected due to the reduction of signal magnitudes and the consequently increased ease of curve resolution.

Visual inspection of the response curve form demonstrated that the first portion of each response curve, the exponential portion, was similar from cycle to cycle, but the second more linear portion of the response curve lost a significant amount of slope in later cycles (Figure 5.2). This more linear portion may correspond to specific effects of the tissue or materials on diffusion or flux.

**Table 5.4** Changes in Time Constants *In Vivo* Between Cycles of Oxygen Challenges  
Changes in time constants between the two cycles of a multi-cycle oxygen challenge are shown at all oxygen concentrations. The response curves are marked on (Figure 5.2), beginning at the appropriate arrow and ending with the assigned colored ring. Initial and final oxygen values of the corresponding exogenous shift are noted at the arrow.

<b>Table 5.4: The Sensor Array with Biomaterials In Vivo, Changes in Time Constants Between Cycles of a Multi-Cycle Oxygen Challenge</b>				
<b><u>Response Curve Markings in Figure 5.2</u></b>	<b><u>Oxygen Shift</u></b>	<b><u>Change in Magnitude From the 1<sup>st</sup> to 2nd Cycle</u></b>		
<b><u>By Ring Color</u></b>		<b>All Sensors</b>	<b>Cellulose Encased</b>	<b>PDMS Encased</b>
Light Grey	10.0→15.0%	16.28±13.67	15.21±16.49	17.35±11.41
White	15.0→20.9%	52.72±23.23	53.85±26.16	51.60±21.96
Dark Grey	15.0→10.0%	59.45±41.99	69.30±51.99	49.61±29.85
Black	20.9→15.0%	0.75±9.15	-2.79±6.86	4.29±10.24
	Combined	32.30±34.94		

Tissue reactions to hypoxia and oxygen dynamics may have caused increases in the functional capillary density of the tissue<sup>(79, 94, 132)</sup>, reducing the average diffusional distance. Other factors that could increase the rate of the tissue's response to exogenous change could be increased myoglobin facilitated diffusion in the muscle<sup>(39, 52, 91)</sup>, or increased vascular flow or extraction of oxygen from hemoglobin in nearer vessels.

There were no consistent or significant differences seen in the time constant changes for sensors encased in different biomaterials. It is likely that, for this particular experiment, rapid dynamic changes in the tissue due to hypoxia may have overshadowed any long term effects of the biomaterials.

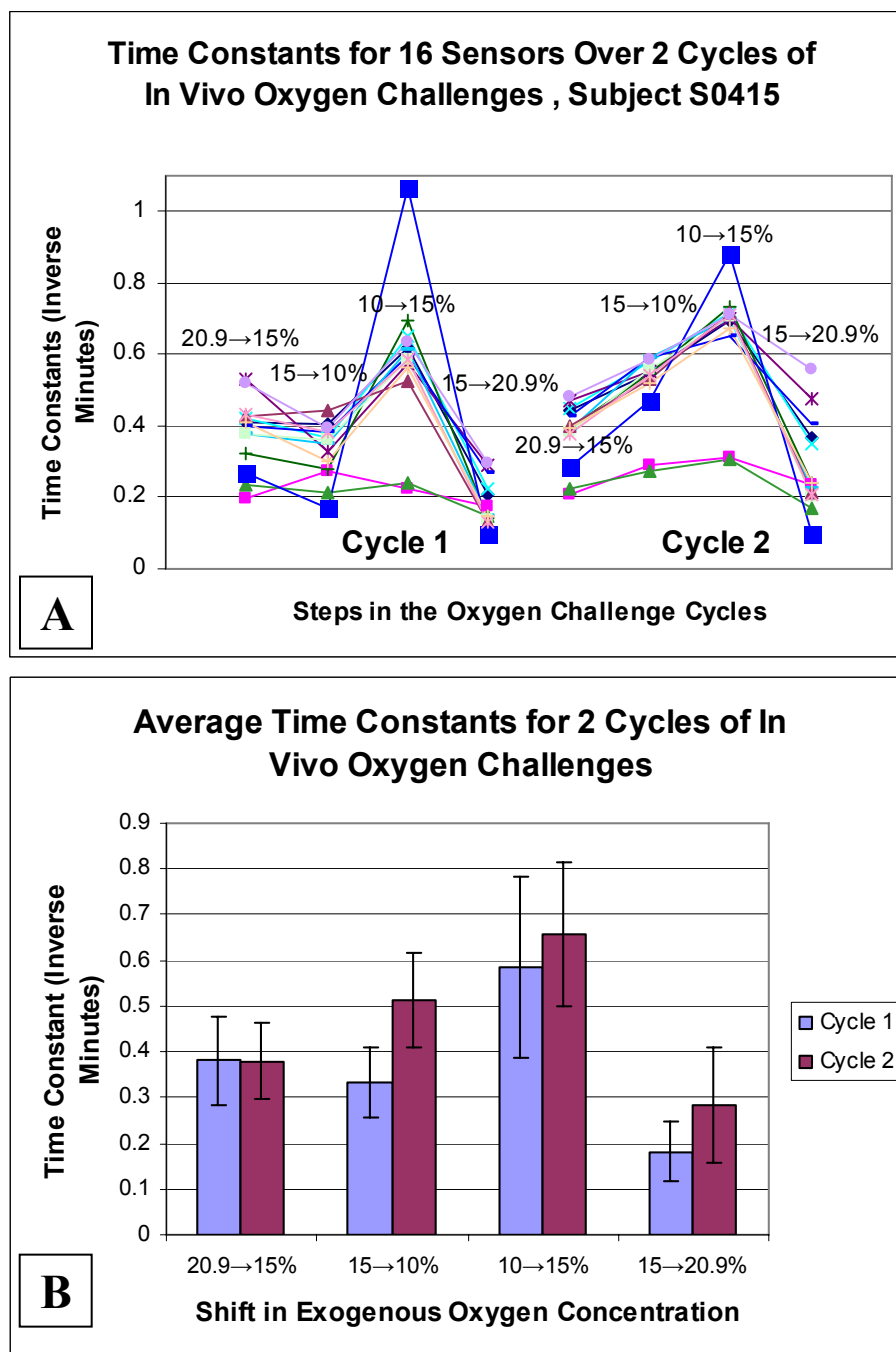


**Figure 5.6** Time Constants for Two Cycles of *In Vivo* Oxygen Challenges

Calculated time constants are shown for four different shifts in exogenous oxygen, during the first and second cycle of an *in vivo* oxygen challenge. (A) shows the time constants for all 16 sensors in different cycles. The oxygen shift the time constants were calculated for is noted, and the first and second cycle are shown separately. (B) shows the averages for each shift for clarity. In general, time constants increased significantly from the 1<sup>st</sup> to the 2<sup>nd</sup> cycle, the exception being the shift from 20.9 to 15.0% oxygen.

#### 5.4.2.3 Effect of Signal Resolution

While many of the sensor responses in these experiments were not allowed to resolve fully, the signal loss from allowing technical resolution as opposed to complete resolution was estimated to be an order of magnitude smaller than the loss of signal magnitude seen with hypoxic exposure.

#### 5.4.2.4 Use of Relative Measures

It is not known for sure how much of the solubility of tissue oxygen is dependent on exogenous oxygen concentration. As well, the respective roles of potential vascular changes versus dissolved oxygen have not yet been established. These uncertainties complicate comparison of *in vitro* and *in vivo* data. Future experimentation would benefit from sensor calibrations performed at lower exogenous oxygen concentrations, closer to those experienced by the sensor *in vivo*.

### 5.5 Conclusion

The results of this experiment demonstrate a role of both tissue and the biomaterials in the response of the sensor to oxygen challenges. The *in vitro* results demonstrate that biomaterials may retain dissolved oxygen that acts to buffer rapid shifts in oxygen concentration. Following periods of hypoxia, these stores are depleted and do not contribute to the sensor signal until the flux imbalance is resolved.

*In vivo* results strongly indicate that tissue also acts to store oxygen, changing measurements in signal magnitude following hypoxic events elevated oxygen exposure. In particular the lesser increase in time constants and the overall increase in signal magnitude at 15.0% oxygen following elevated oxygen exposure demonstrate that the tissue is retaining oxygen that can be depleted and replenished. It is also possible that tissue mechanisms, specifically vascular, may affect the signal magnitude following

hypoxic exposures by altering the flux balance or diffusion properties. Implanted biomaterials seemed to have a less significant effect than the tissue, at least over the two weeks covered by the current study.

Time constants increased during *in vivo* challenges, which conflicts with the *in vitro* observations. Paired with the loss of magnitude from cycle to cycle of the *in vivo* challenges, indicate that oxygen transfer in the tissue was altered by hypoxia. The most likely changes involve increases in functional capillary density or other delivery of oxygen to nearer vessels, changes that would increase the ability of the tissue to adjust to oxygen changes. However, it is interesting that subcutaneous tissue, in the range of hypoxia explored in these studies, does not appear to substantially stabilize oxygen levels, but rather seems to only slow or reduce the loss of oxygen.

There were two key observations of these experiments. First, there was a dependence of the sensor signal and dynamic performance on oxygen history, an important consideration for using the sensor in diagnostic or predictive applications, or for the function of enzymatic sensor co-analyzing oxygen. Second, the tissue response to the material implantation affected this dependency.

A future direction for experimentation would be to study the effects of chronic hypoxia on the phenomena observed here, specifically the change in signal magnitude and time constants. In addition, the comparison of the magnitude of the results seen *in vitro* and *in vivo* were complicated by the relationship of the exogenous oxygen to the actual oxygen experienced by the sensor. Thus future experiments would benefit from calibrations performed at low oxygen levels, closer to those seen *in vivo*.

Experiments using vasoactive compounds<sup>(53)</sup> to even out perfusion of the vasculature may also allow the roles of dissolved oxygen or vascular changes in the tissue during oxygen challenges to be quantified.

# **CHAPTER 6: Quantitative Histological Analysis of Subcutaneous Tissue from Biomaterial Implantations**

## **6.1 Abstract**

In this study, a large scale project to quantify histology through analysis of digital images was undertaken. First a technique for creating seamless images of tissue sections at high resolution was developed. Then, using in-house image processing tools programmed in Matlab (Mathworks), a user interface was created to analyze the digitized histology with respect to specific tissue features with potential impact on oxygen diffusion: including microvessels, muscle fibers, collagen, and cells. For each specific tissue feature, several tools were created to allow analysis of its general color and morphological properties. The established properties were used to filter images, isolating the desired features, quantifying them, and providing information about their spatial distribution.

The results of the project were that color filters, especially those in NTSC space proved useful in feature identification, but morphological filters were required for full isolation of features, and most images required some form of artifact removal, for which tools were developed. The ability of the program to isolate a wide range of features was validated despite variations in sample color and form due to the histological process. The versatility of the program with respect to those elements was also validated.

Subcutaneous tissues from sensor implantations in the hamster window chamber were analyzed with the final program for the vascular proximity values in Chapters 2, 4 and 5 of this dissertation. Tissues adjacent to cellulose were found to have a 17.9% lower average distance to vasculature from the sensor, and cellulose membranes were observed to have been completely penetrated by ingrown tissue by day 14. In addition dermal

tissues adjacent to cellulose in animals implanted with only biomaterial membranes were observed to have a lower mast cell density than tissues adjacent to PDMS.

Potential improvements in future programming, computational capacity, and histological processing are also discussed.

## **6.2 Introduction**

Historically, histological evaluation of the tissue response to biomaterials has tended to be more qualitative in nature. The lower numbers of animal subjects used in these experiments and the implicit difficulty of histological analyses encouraged randomized sampling and subjective scoring of tissue samples. However, to study tissue mass transfer, analysis of histology should be complete, quantitative, and spatial, and should also be correlatable to a method of analyte measurement, such as the implanted oxygen sensors studied in the early chapters of this dissertation.

In this study, methodology is described for analyzing and quantifying several specific tissue features -including microvessels, muscle fibers, collagen, and cells- that may impact oxygen diffusion in the subcutaneous sensor environment. Parameters for isolation using color and morphological filters will be determined, as well as other methods such as combining images from different staining of similar tissue sections, and artifact removal. The study also seeks to create spatially maps of the tissue features, preparing them for application, in future work, to a spatial empirical model of oxygen diffusion. Methods for digitizing histological samples are also detailed in this work, along with a description of the histological measurements used in the earlier chapters of the dissertation.

Because of the variability inherent to tissue collection and staining, fully automated analysis faces significant artifact. The programming in this study is optimized

to allow input from the user during the identification and quantification of features by color and morphological properties and during artifact removal.

## **6.3 Materials and Methods**

### **6.3.1 Nature of the Tissue Samples**

Cutaneous tissue samples were collected as described in Chapter 2 methods. Arrays were active in the 5 animal subjects described in Chapters 2 methods, for about 14 hours over the course of the implantation, with consequent oxygen consumption during those times. In addition, tissue was collected from several animals with dual biomaterial membranes but no active sensor. To test methods for specific stains and tissue features, some samples of paraffin embedded organs were used from fat sand rats.

### **6.3.2 Tissue Sample Processing**

The cutaneous tissue adjacent to each dual material membrane was stiffened using a tetrafluoroethylene (TFE) cooling spray, then was excised with the membrane attached. Each samples' epidermis was carefully marked for orientation before the samples were soaked in histological freezing medium and placed in a double bath of isopentane (2-methyl butane) in liquid nitrogen. The frozen samples were cut into four cross-sections perpendicular to the midline between the biomaterials. Half of these sections were resealed with freezing medium and transferred to a -80°C freezer, and half were transferred to buffered Formalin.

Formalin fixed samples were placed between polyester sponges to prevent deformation and allowed to soak for 24 hours. The samples were then dehydrated over 24 hours in increasing concentrations of ethanol, submerged for 10 minutes in benzene,

and finally transferred to a warm paraffin bath for 24 hours, with two changes of paraffin before embedding. Paraffin samples were professionally sectioned to 8-13 $\mu$ m thick at the UC San Diego Medical Center (Hillcrest Facility).

Frozen samples were sectioned on a Leica 3050 Cryostat at 8-13 $\mu$ m thickness at a 5-10 degree angle. Regular spraying of the samples with TFE between cuts allowed better sectioning. Slices were mounted to positively charged glass slides (Fisher Superfrost Plus slides, Fisher Scientific) and fixed in 4°C acetone for 5 minutes.

For all samples, the resulting slides were cross-sections of the cutaneous tissue with the epidermis at the top, and the sensor on the other. The tissues adjacent to each biomaterial were located on either side, with the cellulose membrane remaining embedded to determine location of the biomaterials.

### **6.3.3 Sample Section Staining**

Sections from each sample were stained with Hematoxylin and Eosin (H&E) to view basic tissue structure and nuclei, with Trichrome for additional identification of collagen, and with a long stain of Giemsa to identify metachromatic cells. Additional frozen sections were stained separately for alkaline phosphatase, periodic acid Schiff, and human and rat CD-31 in order to label the microvasculature.

Paraffin sections were embedded in permount (Fisher Scientific), and frozen sections in glycergel (Dako). HistoClear (Fisher scientific) clearing agent was used for all sections, and fresh anhydrous ethanol was used for mixing dehydration solutions.

H&E stains for paraffin sections were performed by the UCSD Medical Center. H&E staining of frozen sections was performed using a 20 and 5 seconds in Harris' Modified Hematoxylin (Fisher) and Eosin Y respectively with differentiation in acid alcohol (1% HCl in 70% ethanol). Gomori's one step Trichrome (Fisher) with Hematoxylin counterstain was applied per manufacturer instructions to both frozen and

paraffin sections from each sample and compared to consecutive paraffin sections stained with Chromaview's Masson's Trichrome staining kit (Richard Allen Scientific), adopting the methodology of the kit. Both types of sections were soaked in filtered Giemsa, 10% from stock (Fisher) for 20-60 minutes.

Staining for alkaline phosphatase on frozen sections was performed using Burstone's methods<sup>(23, 51)</sup>. Periodic acid Schiff staining was performed on paraffin sections using a kit and the manufacturer's protocol (Sigma Aldrich 395B). Human and rat anti-CD-31 immunohistochemistry staining specific to endothelial cells, was performed on paraffin sections by the UCSD Medical Center. Successful CD31 labeled sections of human tissue were also provided by the UCSD Medical Center.

#### **6.3.4 Digitization of Stained Sections**

Stained sections were mounted on a BX-51WI intravital microscope stage and photographed with an Olympus E330 DSLR camera. Slightly high exposure photographs were taken in a raster pattern assuring contrast with the background, and roughly 15% overlap of adjacent images and of image rows. The dual CCD was used for real-time focusing, avoiding discrepancies in the parfocality. Focus discrepancies were carefully avoided to maximize both photomerge quality and the contrast of individual tissue elements for later machine vision application. Images were taken at 4 and 10x objective magnification using Olympus air objectives, and at 20 or 40x using water objectives, each with 10x magnification by the microscope body.

A multi-core workstation with 4 Gigabytes of high-bus RAM was constructed for image analysis. Virtual memory, the previous bottleneck in photomerge processing, was extended to 64 Gigabytes by exploiting a 64 bit processing architecture.

Photographs were opened in exact consecutive order in Photoshop (vCS2, Adobe), and an in-house program was used to automate cropping of uneven lighting or

edge effects due to the trinocular housing. Once cleaned, images were compiled with the photomerge tool. Despite the increased computing capacity, photomerges taken at 20x objective magnification or greater were compiled in multiple sections. And although the high image exposure reduced background coloration, the final images had their color channel curves flattened in the near white range to increase feature contrast.

### **6.3.5 User Guided Quantitative Analysis of Digitized Histology**

An extensive programming project was undertaken to construct an image processing tool capable of adjustable color and morphological segmentation and filtration of digitized histology. A user interface (Figure 6.1) was constructed for user guided feature selection and artifact removal, export of spatial feature maps, and export of complete spreadsheets of the quantified measurements. The project, termed HistoQuant (HQ), was programmed in Matlab (v6.5.1-2006a, Mathworks) and compiled to an executable program using Matlab Compiler v4 (Mathworks).

### **6.3.6 Abbreviated Processing Pathway and Algorithms**

Complete code and algorithm annotation for the programming has been made available (Appendix D). The general processes for identifying and quantifying a tissue feature are described here in brief.

Analysis is begun by converting an image selection to a 24-bit, 3 layer numerical matrix representing the RGB (Red Green Blue) color space. An spatial map of RGB value labels for each pixel (Figure 6.2) (Matlab v2006a, Mathworks), as well as pseudo-color images and histograms of each color space (Figure 6.3) are used to help determine the color values and morphology of a specific feature. Each image is also converted to NTSC space (Figure 6.4), a common camera and television broadcasting format. This

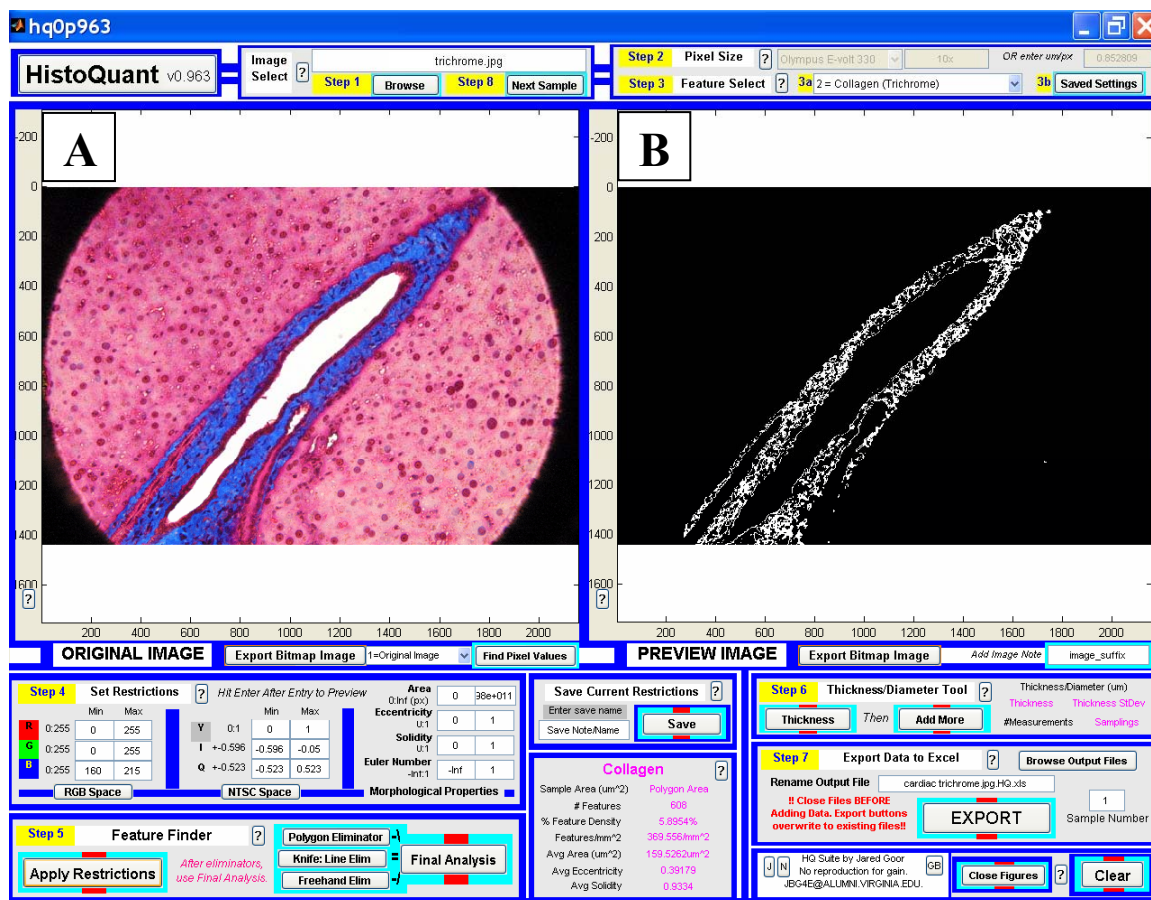


**Figure 6.1** The HistoQuant User Interface: Isolating Collagen in Masson's Trichrome Stained Liver Images

The HistoQuant user interface is shown in full. An image is selected in the first step, and then a series of tools are employed to determine the color and morphological qualities of the desired tissue feature. The determined values, along with several manual artifact removal tools, are used to isolate the tissue features, quantifying their number and morphology. The image of the isolated tissue is exported for modeling, and all numerical data is finally exported to a spreadsheet for analysis. Collagen is shown stained blue by Masson's Trichrome in a liver section (200x) (A). The program used a low pass filter for blue coloration and a high pass for in-phase chrominance to isolate the collagen (B). The axes are labeled in pixels, at  $0.52\mu\text{m}/\text{pixel}$ .

method has proven to be helpful in distinguishing features that are similarly colored in RGB space. Once the color properties of the feature of interest are found, they are used to filter the image matrix keeping only values above the established minimum and maximum values for

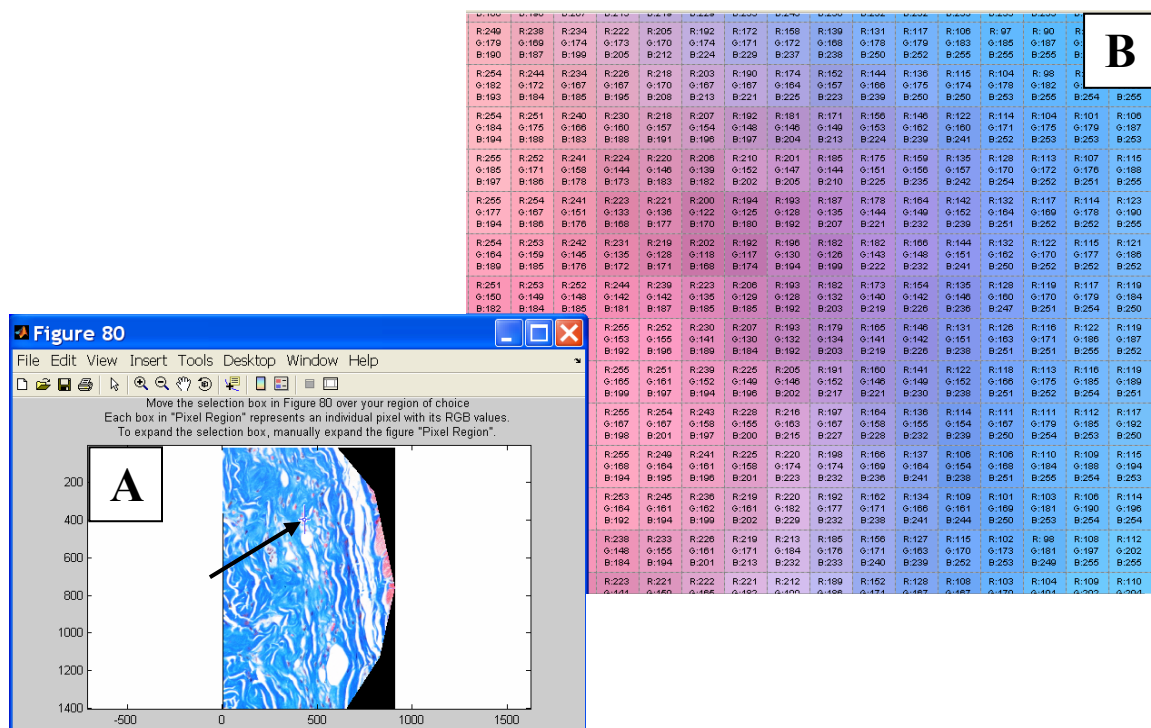


**Figure 6.2** Spatial Map of RGB Pixel Values: Isolating Erythrocytes in Masson's Trichrome Stained Subcutaneous Tissue Images

The figure shows a spatial map of RGB pixel values (B) transposed onto the corresponding real color pixels from an enlarged high resolution image of the small selection in (A) labeled by the black arrow. The left hand side of (B) shows the red coloration of an erythrocyte against a background of blue stained collagen (200x) at the right. Values for color filters were gleaned from comparing RGB values in these two sections. The axes are labeled in pixels, at  $0.52\mu\text{m}/\text{pixel}$ .

a feature. The Hadamard product of the RGB and NTSC matrices, often referred to as the 'dot' or 'entrywise' product, is flattened by further entrywise multiplication of the 3 layers, resulting in a 2-dimensional matrix. The matrix is normalized, resulting in a binary image, with all pixels passing the color filters having a value of 1.

Camera model and objective magnification are used to calculate the true size of an image pixel based on pre-calibration images of slide micrometers. These calculations are used to estimate the area and length of the feature. Besides the simple proportion measurements, the eccentricity, solidity, and Euler number of the feature are determined.

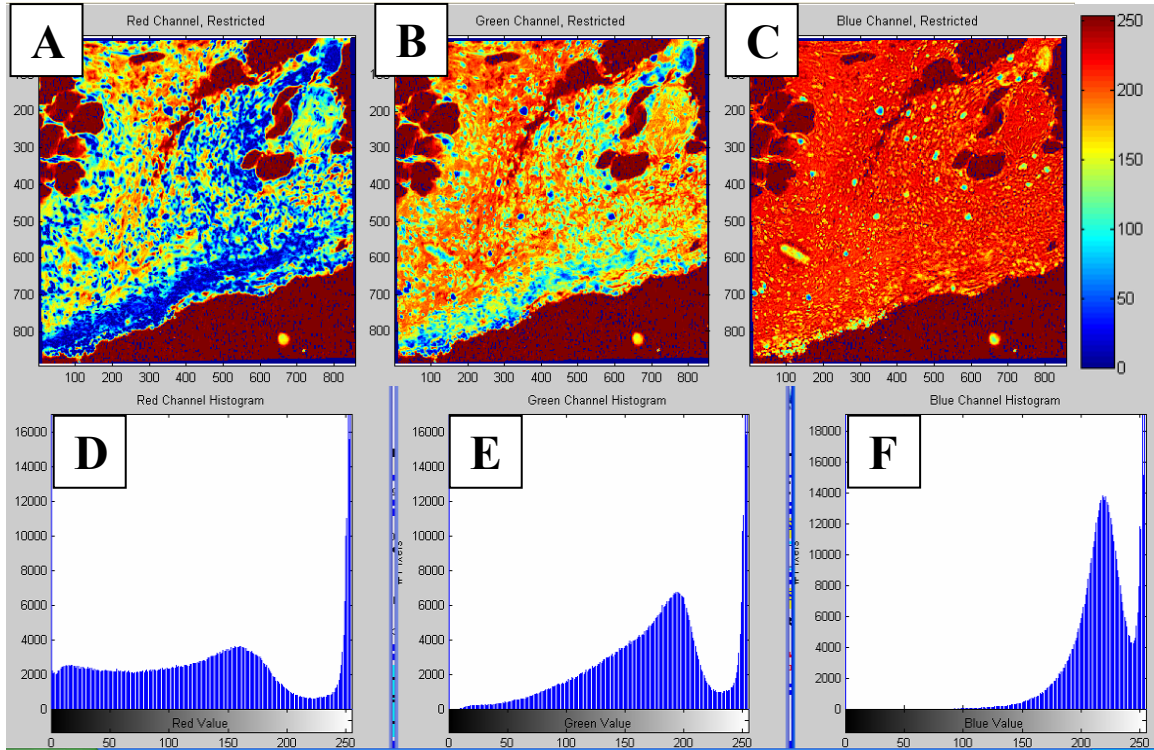


**Figure 6.3** Pseudo-Color Images and Histograms of the RGB Color Channels: Isolating Mast Cells in Giemsa Stained Subcutaneous Tissue Images

Subcutaneous tissue from adjacent to an inactive cellulose covered biosensor is shown, separated into RGB color channels. The red (A), green (B), and blue (C) color information from the image are displayed in pseudo-color. A color bar at right shows how the pseudo-color scale relate to the pixel's color intensity in 8-bits (range = 0-255). The histograms for the three color channels are shown (D-F). Bins on the X-axis are for pixel intensities from 0-255, with the number of pixels in the bin shown on the Y-axis. These tools, along with those for the NTSC channels, allow the color filters to be determined for isolating specific features. Mast cells (200x) are visible in (C) as green dots and in (B) as dark blue dots. Too few mast cells are present to create a peak in the histograms. The axes are labeled in pixels, at  $0.52\mu\text{m}/\text{pixel}$ .

$$\begin{bmatrix} Y \\ I \\ Q \end{bmatrix} = \begin{bmatrix} 0.299 & 0.587 & 0.114 \\ 0.596 & -0.274 & -0.322 \\ 0.211 & -0.523 & 0.312 \end{bmatrix} \begin{bmatrix} R \\ G \\ B \end{bmatrix}$$

**Figure 6.4** Conversion Matrix for NTSC Color Space

The conversion matrix shown is used to translate red (R), Green (G), and Blue (B) pixel values and translate them into the three color channels utilized by NTSC, luminance (Y), In Phase Chrominance (I), and Quadrature Chrominance (Q). For programming purposes, the RGB values are first normalized. Y has a range from 0-1, but I and Q values, due to color subtraction, have ranges of  $\pm 0.596$  and  $\pm 0.523$  respectively.

Eccentricity refers to the relationship between the major axis,  $a$  of the feature and its minor axis,  $b$  ( $\text{Eccentricity} = \sqrt{1-b^2/a^2}$ ), where a circle has an eccentricity of 0, and a line an eccentricity of 1 (Range: 0-1). Solidity is the fraction of non-zero pixels in a feature (Range: 0-1). Euler number is the number of objects minus the number of holes in the object (Range:  $-\infty$ -1).

For morphological filtering, Equivalence methodology<sup>(54)</sup> is applied, first identifying pixels in the image that are adjacent to one another, or 'clustered', then assigning clusters of pixels unique numerical labels. Cluster boundaries and orientation are used to determine their morphological characteristics. Then, the properties of each pixel clusters are logically compared to the desired minimum and maximum morphological properties of the specific feature. Pixel clusters meeting the criteria are kept, while those which do not are eliminated. Clusters that are too large or small, too eccentric, not solid enough, etc. are removed from the image and the remaining clusters are re-identified and their properties quantified. Initial determination of a specific feature's morphological properties is thus often iteratively determined by several adjustments to filter values.

The images are segmented by color and morphology and filtered for pixels and pixel clusters that do not meet filter criteria of the feature under analysis. Next, a user guided system allows the removal of remaining artifacts. Two types of tools are employed: a polygonal elimination tool (Figure 6.6) and line-drawing tools designed to separate adjoined objects by minimized deletion of their connecting pixels (Figure 6.7). After artifact removal, the remaining pixel clusters are re-analyzed, their properties calculated, and the resulting data exported to Excel (v2003 Microsoft) spreadsheet format for further analysis. The spatial map of the clusters is also exported.

In addition to pixel selection, the HQ program allows true scale length measurements. A user guided tool is used to trace lines on the original image, which are converted to real distances using the pre-calibrated pixel size measurements.

### **6.3.7 Features of Interest**

Several tissue features were analyzed that were expected to have a significant effect on oxygen transfer: these features were nonspecific cell nuclei, mast cells, muscle fibers, microvasculature, and collagen. In addition, the thicknesses of the muscle layer, the distance between the biomaterial and the muscle layer, the thickness of the dense tissue at the biomaterial surface, and the depth of tissue penetration into the microporous biomaterials were measured.

While the detailed analysis of tissue from biosensor implantations is the long term goal of the histological quantification project, for the purposes of this dissertation, the focus will be on methods and parameters for identifying tissue features and the successful production of spatial feature maps. The maps are for use in spatial analysis of feature distribution and for future use in spatial diffusion modeling of oxygen transfer in the tissue surrounding implanted sensors.

## **6.4 Results**

### **6.4.1 Length Measurements**

The length measurement tool was found to be highly reliable down to within 1-2 pixels. However, images with poor resolution were prone to error in true distance. A solution to reduce the error from pixelation was implemented, where the endpoints of measurement lines were not rounded off to exact pixels, i.e. forced onto a grid, but rather

allowed to be designated in fractions of pixels. Accuracy of measurements was improved an estimated 7.9% in the measurement of capillaries imaged at  $1.04\mu\text{m}$  per pixel.

Table 6.1 lists the distance measurements made in the tissue samples from the 5 animals. Tissue penetration of the cellulose was determined to be 100% in all samples. For animal S0414, whose cellulose was completely intact, the cellulose itself was found to occupy only 33.20% of its bounding box (Figure 6.5). The ingrown tissue, mostly loose connective tissue, occupied 12.42% of this space inside the cellulose with remainder being occupied by elements such as fluids or proteoglycans which would have been removed by the histological processing. The ingrown tissue was largely concentrated at the interface of the cellulose with layer of PDMS backing. It occupied a space  $92.79\pm 15.35\mu\text{m}$  on average from this inner membrane. Very little ingrown tissue was seen surrounding cellulose fibers, further indicating that the tissue reacted more to the PDMS inside the cellulose than to the cellulose. The results in S0414 reflected those seen in intact regions of cellulose in other animals.

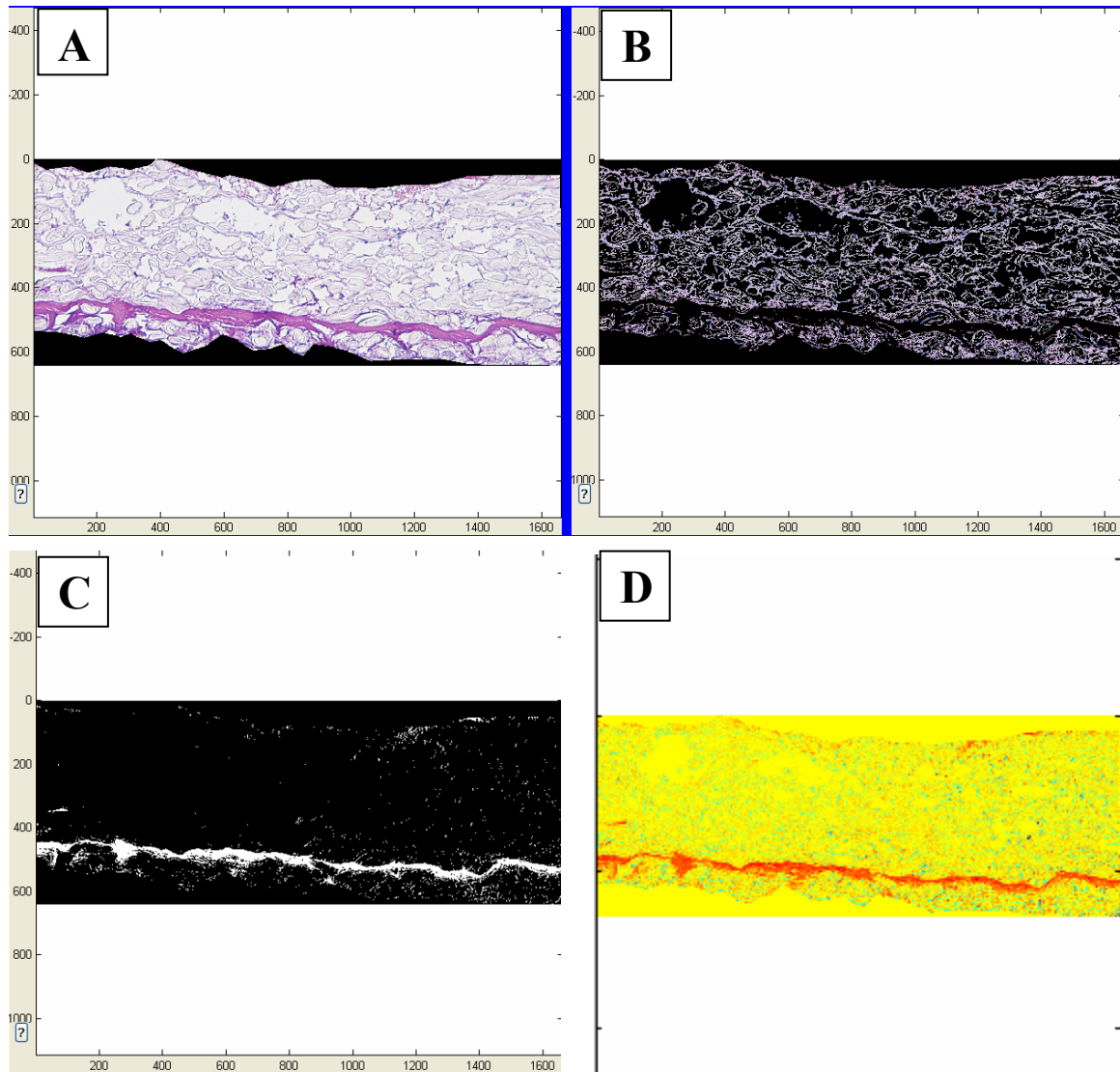
#### **6.4.2 Color and Morphological Criteria for Feature Isolation**

Table 6.2 lists the collected filtration criteria that were determined for each of the specific features, including methods of manual artifact removal. These criteria allowed artifact free spatial maps of the features to be created for used in the tissue oxygen diffusion model.

**Table 6.1** Measured Distances in Subcutaneous Tissue Explanted from Hamster Window Chambers with Active Oxygen Sensor Arrays

Vascular proximity is measured to the membrane rather than the array for contrast. In addition to the measured distances shown in the table, the results of magnitude and time constant measurements for each animal on day 14, just prior to sacrifice, are included for reference. These values are referred to in Chapters 2 and 4 respectively. Time constants for both upward and downward shifts in exogenous oxygen are shown.

<b>Table 6.1 Measurements in Subcutaneous Tissue From Active Oxygen Sensors</b>							
<b>Animal Subject</b>		<b>S0411</b>	<b>S0414</b>	<b>S0415</b>	<b>S0416</b>	<b>S0417</b>	
<b>Vascular Proximity to Membrane (<math>\mu\text{m}</math>) (n &gt; 48)</b>	<b>Combined</b>	429.0 $\pm$ 102.7	37.1 $\pm$ 29.1	591.7 $\pm$ 171.7	120.0 $\pm$ 40.6	393.7 $\pm$ 63.8	
	<b>Over Cellulose</b>	437.3 $\pm$ 102.0	15.1 $\pm$ 7.74	519.8 $\pm$ 112.2	102.2 $\pm$ 16.5	450.8 $\pm$ 25.8	
	<b>Over PDMS</b>	421.1 $\pm$ 104.7	54.7 $\pm$ 28.0	678.5 $\pm$ 192.3	145.7 $\pm$ 50.8	340.7 $\pm$ 36.2	
<b>Muscle Layer Thickness (<math>\mu\text{m}</math>) (n&gt;48)</b>	<b>Combined</b>	279.5 $\pm$ 151.0	8.29 $\pm$ 16.0	142.2 $\pm$ 148.2	n/a	91.6 $\pm$ 58.1	
	<b>Over Cellulose</b>	240.9 $\pm$ 154.6	1.75 $\pm$ 1.89	82.8 $\pm$ 65.0	n/a	47.0 $\pm$ 15.1	
	<b>Over PDMS</b>	318.2 $\pm$ 139.4	14.2 $\pm$ 20.4	201.7 $\pm$ 183.1	n/a	134.1 $\pm$ 46.9	
<b>Time Constant (<math>\text{min}^{-1}</math>) (n &gt; 6)</b>	<b>Cellulose</b>	<b>15.0<math>\rightarrow</math>10.0%</b>	0.085 $\pm$ 0.010	0.364 $\pm$ 0.123	0.256 $\pm$ 0.268	0.065 $\pm$ 0.019	0.088 $\pm$ 0.003
		<b>10.0<math>\rightarrow</math>15.0%</b>	0.061 $\pm$ 0.008	1.929 $\pm$ 0.353	0.544 $\pm$ 0.058	0.397 $\pm$ 0.141	0.094 $\pm$ 0.007
	<b>PDMS</b>	<b>15.0<math>\rightarrow</math>10.0%</b>	0.093 $\pm$ 0.027	0.320 $\pm$ 0.125	0.327 $\pm$ 0.101	0.124 $\pm$ 0.075	0.078 $\pm$ 0.009
		<b>10.0<math>\rightarrow</math>15.0%</b>	0.150 $\pm$ 0.065	2.397 $\pm$ 1.061	0.461 $\pm$ 0.037	0.321 $\pm$ 0.122	0.114 $\pm$ 0.034
	<b>Combined Average</b>		0.092 $\pm$ 0.041	1.259 $\pm$ 1.099	0.397 $\pm$ 0.180	0.204 $\pm$ 0.162	0.094 $\pm$ 0.023
<b>Baseline Signal Magnitude on Day 14, Normalized To: (n &gt; 6)</b>	<b>Pre-Calibration</b>	<b>Cellulose</b>	0.510 $\pm$ 0.112	0.091 $\pm$ 0.017	0.272 $\pm$ 0.118	0.458 $\pm$ 0.225	0.096 $\pm$ 0.021
		<b>PDMS</b>	0.427 $\pm$ 0.052	0.131 $\pm$ 0.048	0.235 $\pm$ 0.071	0.567 $\pm$ 0.337	0.342 $\pm$ 0.278
		<b>Combined</b>	0.351 $\pm$ 0.380	0.113 $\pm$ 0.041	0.253 $\pm$ 0.095	0.509 $\pm$ 0.278	0.227 $\pm$ 0.234
	<b>Day 4</b>	<b>Cellulose</b>	3.45 $\pm$ 2.79	1.69 $\pm$ 0.22	0.63 $\pm$ 0.11	3.99 $\pm$ 2.23	1.62 $\pm$ 0.60
		<b>PDMS</b>	1.28 $\pm$ 0.86	1.47 $\pm$ 0.43	1.93 $\pm$ 2.20	4.57 $\pm$ 4.67	5.11 $\pm$ 3.49
		<b>Combined</b>	0.24 $\pm$ 2.30	1.58 $\pm$ 0.35	1.54 $\pm$ 1.90	4.26 $\pm$ 3.45	3.48 $\pm$ 3.09



**Figure 6.5** Tissue Ingrowth into Cellulose Implanted in Hamster Subcutaneous Tissue  
 In (A) the original true color image of H&E stained cellulose from a 14 day implantation adjacent to a sensor is shown. (B) shows the binary image of isolated cellulose fibers produced by a low pass filter for all RGB color channels, and a banded filter for quadrature chrominance. Figure (C) shows the binary image of the isolation of ingrown tissue from the original image in (A), created using a high pass filter for in-phase chrominance (IPC). (D) shows the pseudo-color image of the IPC channel. The axes are labeled in pixels, at  $0.56\mu\text{m}/\text{pixel}$ .

**Table 6.2** Filtration Parameters for Isolating Specific Tissue Features in Digital Images of Histological Sections

The table gives an overview of the filter parameters determined to be effective in isolating histological features in digital images. Effective isolation was defined as the ability to quantify the feature's morphology, and to distinguish features from one another, from artifact, and from background. In general, color filters alone were not sufficient and required pairing with morphological filters. Many images retained artifacts after filtration that required manual removal. The artifact removal process for each feature is listed.

(RGB color space = R, G, and B) (luminance = Y, in-phase chrominance = I, and quadrature chrominance = Q) (Eccentricity = Ecc, Solidity = Sol)

<b>Table 6.2 Filter Parameters for Digital Histological Feature Isolation</b>					
<b>Tissue Feature Parameters</b>			<b>Filters</b>		<b>Artifact Removal</b>
<b>Feature</b>	<b>Tissue Type</b>	<b>Stain</b>	<b>Color</b>	<b>Morphological</b>	
<b>Collagen</b>	Liver	Masson's Trichrome	Low: B, High: IPC	n/a	Polygon
<b>Mast Cells</b>	Subcutaneous	Giemsa	Low: RGB,Y,I	High: Area	Polygon
<b>Nuclei</b>	Subcutaneous	H&E	Low: R,B,Y	Band: Area	Polygon, Knife, Dilation
<b>Muscle Fibers</b>	Subcutaneous	H&E	Band: I	High: Area, Low: Ecc	n/a
	Subcutaneous	Giemsa	Low: I	High: Area	n/a
<b>Erythrocytes</b>	Subcutaneous	Masson's Trichrome	Low: G,B High: I	Band: Area, Low: Ecc, High: Sol	n/a
<b>Endothelial Cells</b>	Human Tumor	CD-31 IHC	Low: R, High: I	Low: Area, before and after dilation	Dilation & Erosion

#### 6.4.2.1 Collagen

Collagen was isolated as a measure of potential diffusive resistance in the tissue. Staining via Masson's Trichrome also provided a simple example of the use of color filtration (Figure 6.1). Collagen in large vessel walls and subcutaneous tissue was easily isolated and distinguishable from counter stains using only color filters.

Future studies with labels specific to new collagen, or immunohistochemical methods for labeling type I versus type III collagen<sup>(61, 135)</sup> would be useful in the further understanding of potential wound healing differences in the tissue adjacent to the biosensors.

#### 6.4.2.2 Mast Cells

Mast cells were isolated as a potential measure of tissue inflammation. Counts during preliminary data analysis found that the tissue adjacent to cellulose implants had a systematically but not statistically greater number of mast cells than tissues adjacent to PDMS, by  $21.85 \pm 8.18\%$  on average,  $n=12$ . The relationship was by linear density, where cell number was normalized by the width of the tissue cross-section. By area the disparity was greater, since PDMS tissues were seen to be thicker on average from the muscle to the biomaterial membrane (Table 6.1).

An average of 521.3 cells were found per square millimeter in the tissue adjacent to cellulose implants without active sensors, most located near large microvessels or in the retractor muscle layer 184-376 $\mu\text{m}$  away from the sensor. The more avascular samples from animals with sensors had generally very few mast cells, which makes sense given that vessels, preferentially larger ones, are required to introduce mast cells recruited from the marrow<sup>(43)</sup>. The mast cells that were observed were found to be in various stages of degranulation, indicating that the cells were still active.

Isolation of the mast cells in Giemsa stains was primarily accomplished by several low pass color filters (Figure 6.6). Filters for any one color were effective in removing most of the background tissue, but a combination was more effective at removing artifacts such as dye deposits, and tissue folds, and dust or oil in the optical path. Distinguishing mast cells from other nuclei was effected by a low pass for red coloration. Color filtering allowed many artifacts to remain, especially small clusters or individual pixels not large enough to be cells. Other artifacts included clusters of non-specific cell nuclei. High pass filters for area and solidity, as well as a low pass filter for cell eccentricity, removed most of these artifacts, but a few were removed by hand using a

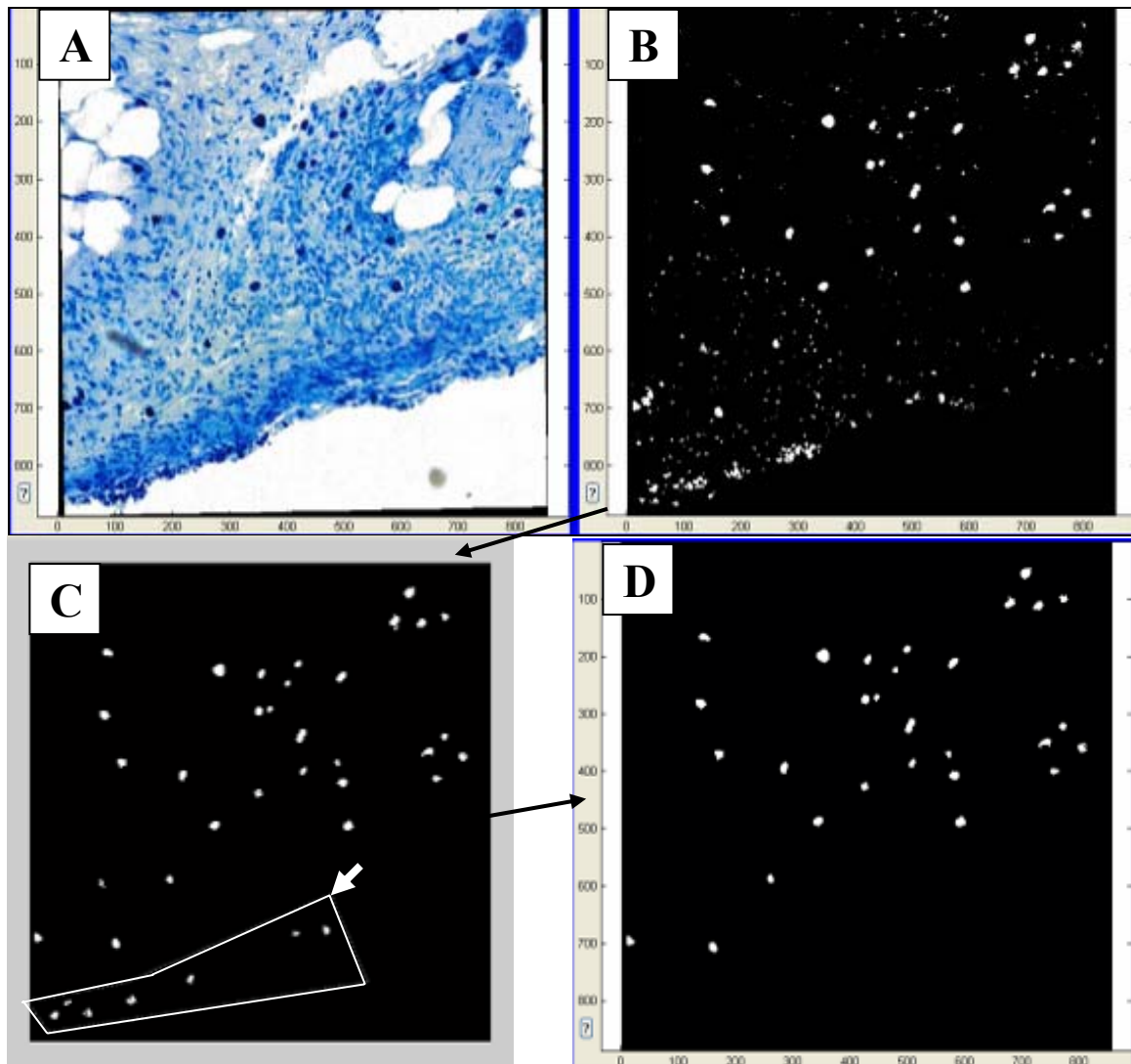


**Figure 6.6** Isolating Mast Cells in Giemsa Stained Subcutaneous Tissue Images

The figure shows isolation of mast cells using a combination of filters. (A) shows the original polygonal selection taken from a digitized histological slice (200x) of subcutaneous tissue from a cellulose membrane without an active sensor. (B) is a binary image, representing the pixels which passed color filters. (C) then shows the binary image after a low pass filter for pixel cluster eccentricity, and high pass filters for cluster area and solidity. The polygon shown in (C) is the user guided artifact elimination tool in the process of removing some dark staining portions of the fibrous capsule. These artifacts then do not appear in the final binary image (D), which is ready for numerical analysis and export to the empirical oxygen diffusion model. The axes are labeled in pixels, at  $0.52\mu\text{m}/\text{pixel}$ .

polygon removal tool (Figure 6.6C). Euler number also proved useful in removing a few artifacts with significant holes, which the solidity filter did not catch. In the program,

jagged objects appear to have lower solidity. Thus, solidity filters could not be too stringent, or genuine cells that are not smooth at the edges would have been removed.

Using the determined isolation criteria, mast cells in the biomaterials preparations were found to have an average area of,  $50.04 \pm 18.83 \mu\text{m}^2$ , which varied slightly for cells in different stages of degranulation. Future refinements to the program may utilize solidity and perimeter analyses, as well as cluster entropy measurements to isolate cells in the process of degranulating, a potentially more powerful marker of inflammation.

#### **6.4.2.3 General Nuclei**

Microscopic observations demonstrated the presence of fibroblasts, lymphocytes, and vascular endothelial cells in the dermal tissue and near the implants, as well as other cell types more difficult to identify morphologically. General nuclei from these cells were isolated for the purpose of estimating tissue consumption, under the simplified assumption that greater numbers of cells would relate to greater oxygen consumption. It is understood that the rate of individual cellular consumption varies by cell type and can be altered by inflammation, hypoxia, and other factors. Thus, future studies using mitochondrial markers or active measures of tissue metabolism may lead to improved understanding of tissue oxygen diffusion. Additionally, immunohistochemical stains or use of unique nuclei shapes could help separate different cell types using the program.

Using H&E stains, isolation of nuclei was essentially isolation detection of regions of heavy hematoxylin stain. Red and luminance low pass filters were sufficient to remove most, 85.2%, of the tissue background (Figure 6.7). The area of the nuclei was very consistent, and thus a banded area filter removed virtually all remaining artifacts, or 36.9% of pixels which passed the color filters but were not nuclei. Unlike Mast cells, there was more clustering of nuclei, so for small images, the knife tool built into the program helped to separate these nuclei prior to quantification, without greatly altering density measurements (Figure 6.8). The average nuclei area before using the knife tool

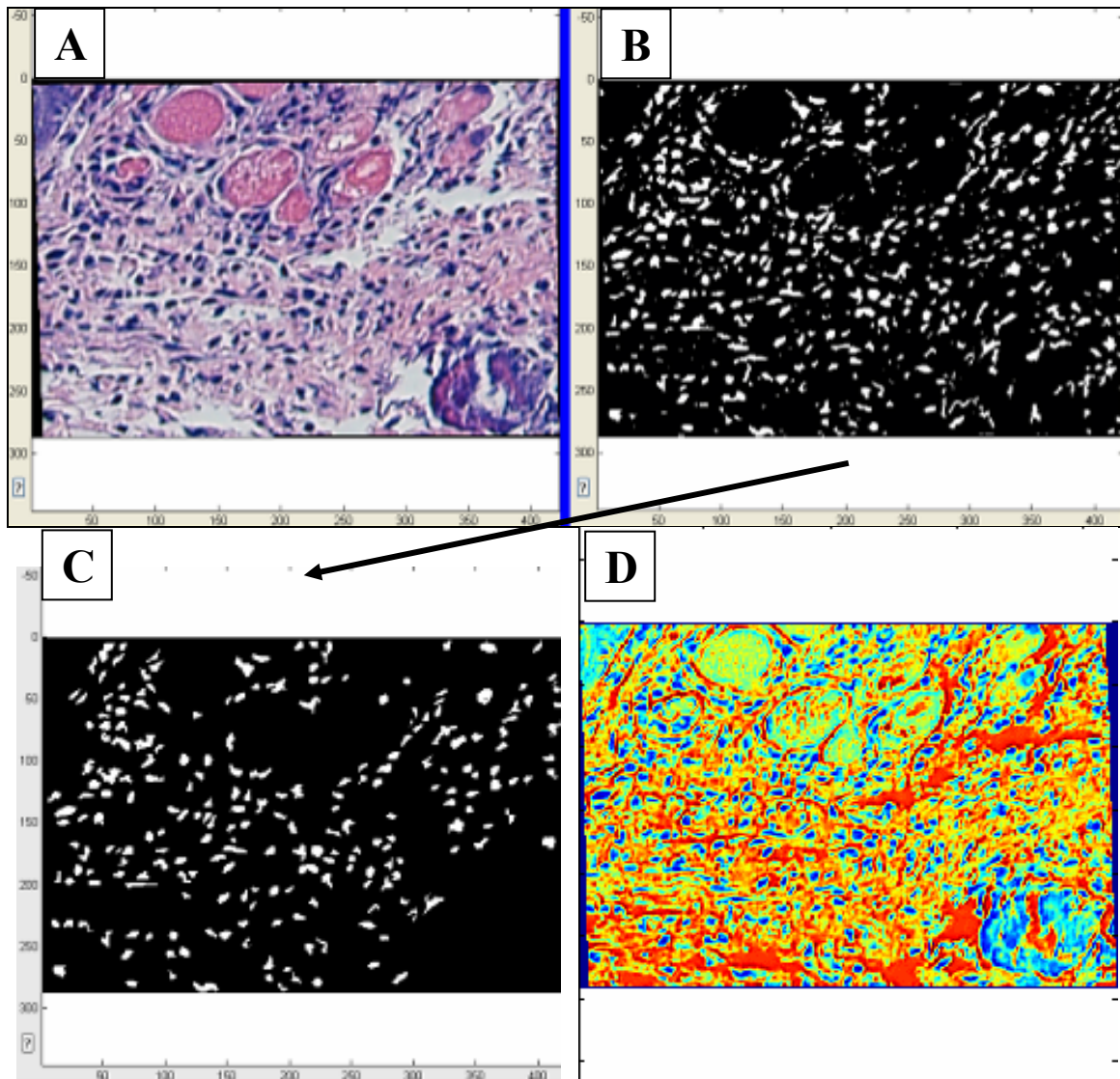


**Figure 6.7** Isolating General Cell Nuclei in H&E Stained Subcutaneous Tissue Images (B) shows the initial isolation of general cell nuclei from the original image selection (A) (100x), using color filters, specifically low pass red and luminance. Many artifacts remain. (C) shows the final binary image after an a banded area filter, polygon elimination of the artifact in the bottom right corner, and some cell separation with the knife tool (Figure 6.8). The luminance (D) channel is shown in pseudo-color, where nuclei are visible as dark blue spots indicating the high concentration of hematoxylin and a lack of eosin. Larger artifact regions are easily identifiable as light blue, indicating incomplete hematoxylin stain and some eosin. The axes are labeled in pixels, at  $0.56\mu\text{m}/\text{pixel}$ .

was  $51.4 \pm 27.0 \mu\text{m}^2$ , while that after was  $43.0 \pm 18.3 \mu\text{m}^2$ , a drop of 16.4%, indicating that nuclei clustering is a problem to quantification. Thinner tissue sections would very likely circumvent the problem of nuclei clustering, as would improvements in image focus. An alternative to the knife tool, for larger tissue samples, is to perform careful counts on a few small images and use the ratio of nuclei count to density to calibrate larger images.

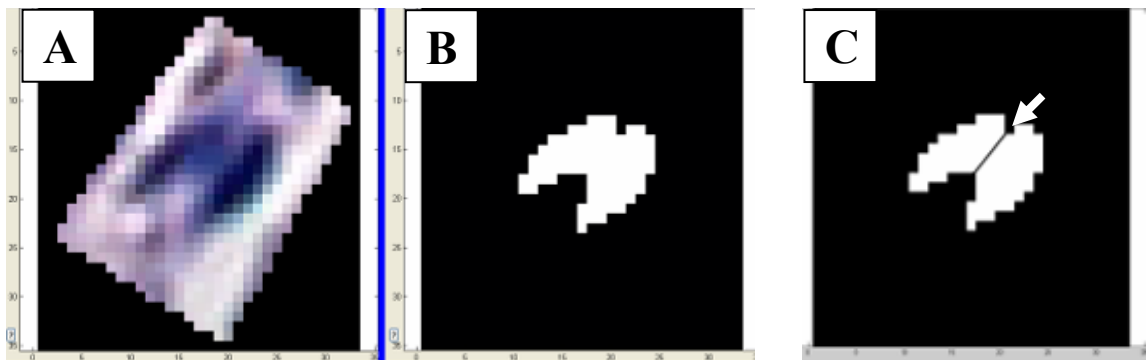


**Figure 6.8** Separation of Adjoined Features

A cluster of two nuclei that are mathematically indistinguishable is shown in (A). The image was verified by microscopic observation at higher magnification to be two different nuclei. (B) is a binary image of the pixels that met color filter criteria. The two nuclei are not distinguished from one another. In (C) the knife tool is shown while separating the nuclei by the minimum number of pixels required to classify them as distinct. The axes are labeled in pixels, at  $0.56 \mu\text{m}/\text{pixel}$ .

Prior to use in an oxygen diffusion model, spatial maps of the nuclei would be modified. Knowing that cellular oxygen consumption occurs in the mitochondria, pixel clusters representing the cell nuclei are proportionately dilated to encompass the cell cytoplasm (Figure 6.9). The dilated nuclei have the same eccentricity and orientation, but the method does not account for variations in different cell types' nucleus-to-cell area ratio or for the unique shapes like flattened fibroblasts or macrophages.

#### 6.4.2.4 Muscle Fibers

Muscle fibers were isolated from images of both H&E and Giemsa stained sections using in-phase chrominance filters (Figures 6.10 and 6.11). High pass filtering of pixel cluster areas removed some artifact, but a low pass filter for eccentricity finalized the isolation. Eccentricity of the muscle fibers was very low due to their circular nature

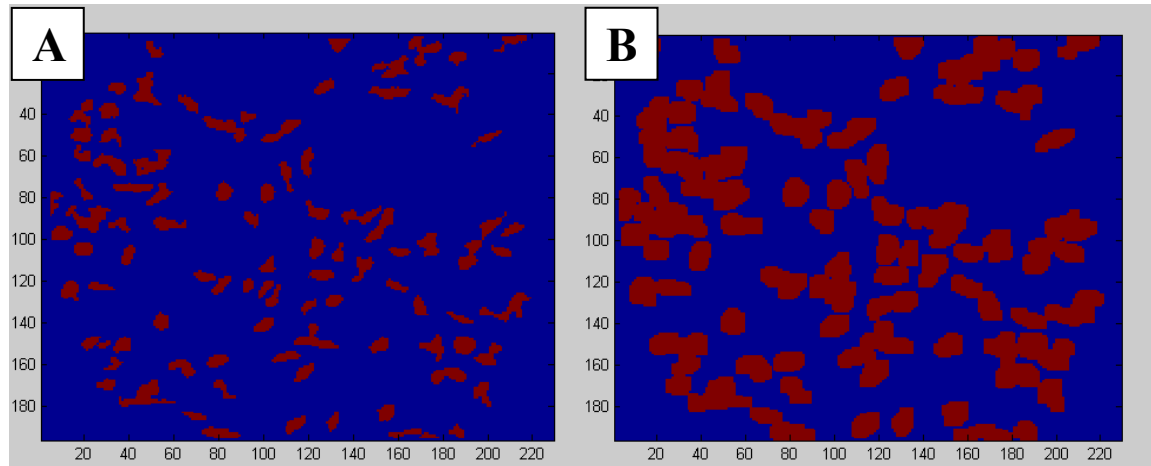


**Figure 6.9** Dilation of Nuclei to Define Cell Boundaries

(A) is the same binary image seen in Figure 6.9D, representing isolation of general nuclei from an image of H&E stained subcutaneous tissue. (B) is the map after dilation of the nuclei using the general proportion of fibroblast area to nucleus area. Such maps would be more useful in estimations of diffusion and consumption. The axes are labeled in pixels, at  $0.56\mu\text{m}/\text{pixel}$ .

in cross section, so most artifacts were removable by eccentricity filtering. The greater contrast of muscle in Giemsa required no eccentricity filters.

The binary image of the H&E stained muscle was full of holes due to removal of counterstained muscle nuclei and endothelial cell nuclei from adjacent capillaries. Giemsa images without counterstain produced clean fiber isolations.

Muscle fiber will be an important part of diffusion modeling for studies in the hamster window chamber, and other models including reticular muscles, due to potential differences in consumption as well as the effects of myoglobin on oxygen diffusion<sup>(91)</sup>.

NTSC color filters appear to be extremely helpful in muscle fiber isolation (Figures 6.10 and 6.11).

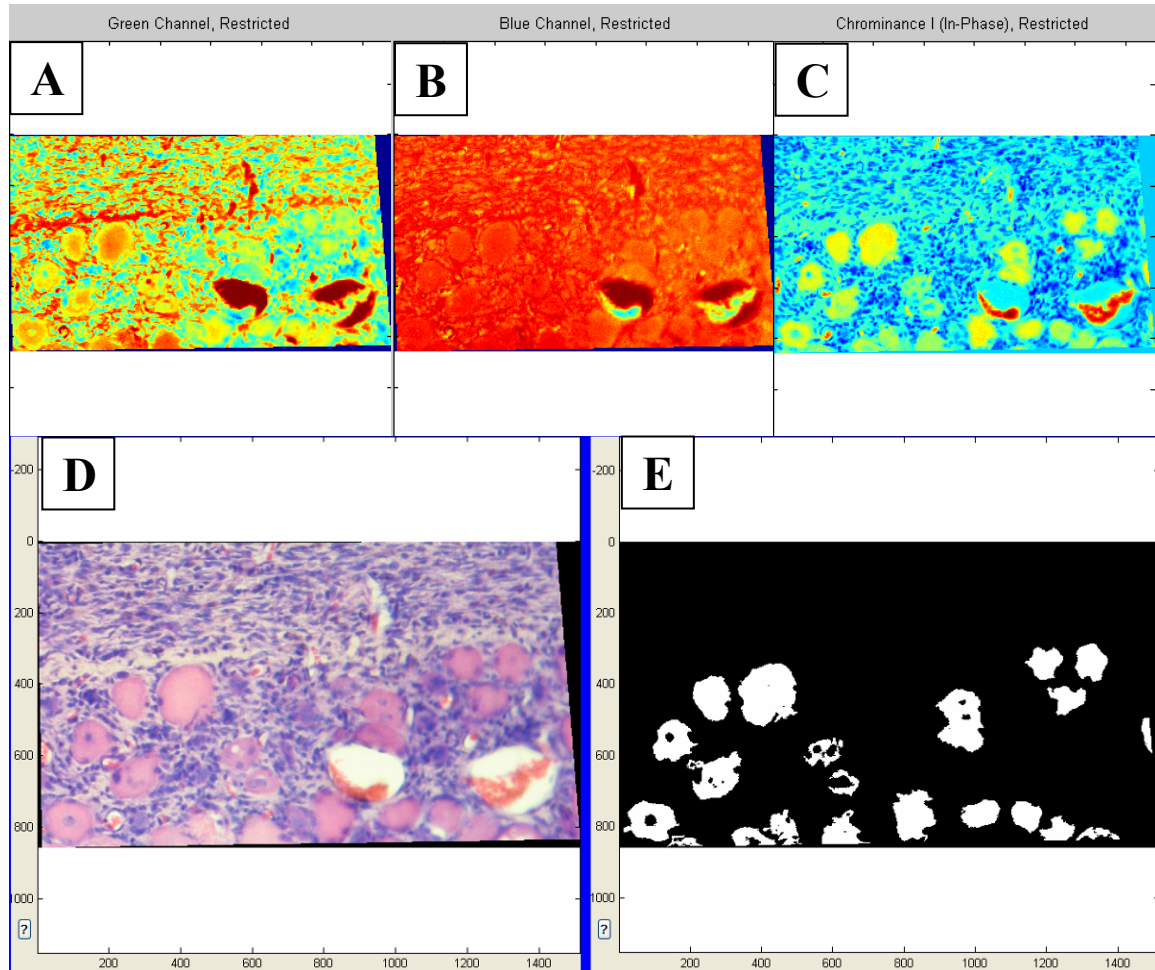


**Figure 6.10** Isolating Muscle Fibers in H&E Stained Subcutaneous Tissue Images  
Pseudo-color maps of the green (A), blue (B), and in-phase chrominance (C) channels are shown for an image of H&E stained subcutaneous tissue (D) (100x). The maps demonstrate the effectiveness of NTSC filters. The granulation tissue at the top of the image is defined by a white horizontal line in (D), also visible in (A) as a red line. Below this line are the muscle fibers and some large blood vessels. Green color (A) defines some muscle fibers but not others. Blue color (B) does not define the fibers, but does clearly distinguish the blood vessels. IPC banded filtering (C) clearly defines muscle fibers. The final binary image (E) on the right has been color filtered and filtered by a high pass for area and a low pass for eccentricity. The interference of muscle and endothelial cell nuclei, breaking up the muscle image, should be noted. The axes are labeled in pixels, at 1.04 μm/pixel.

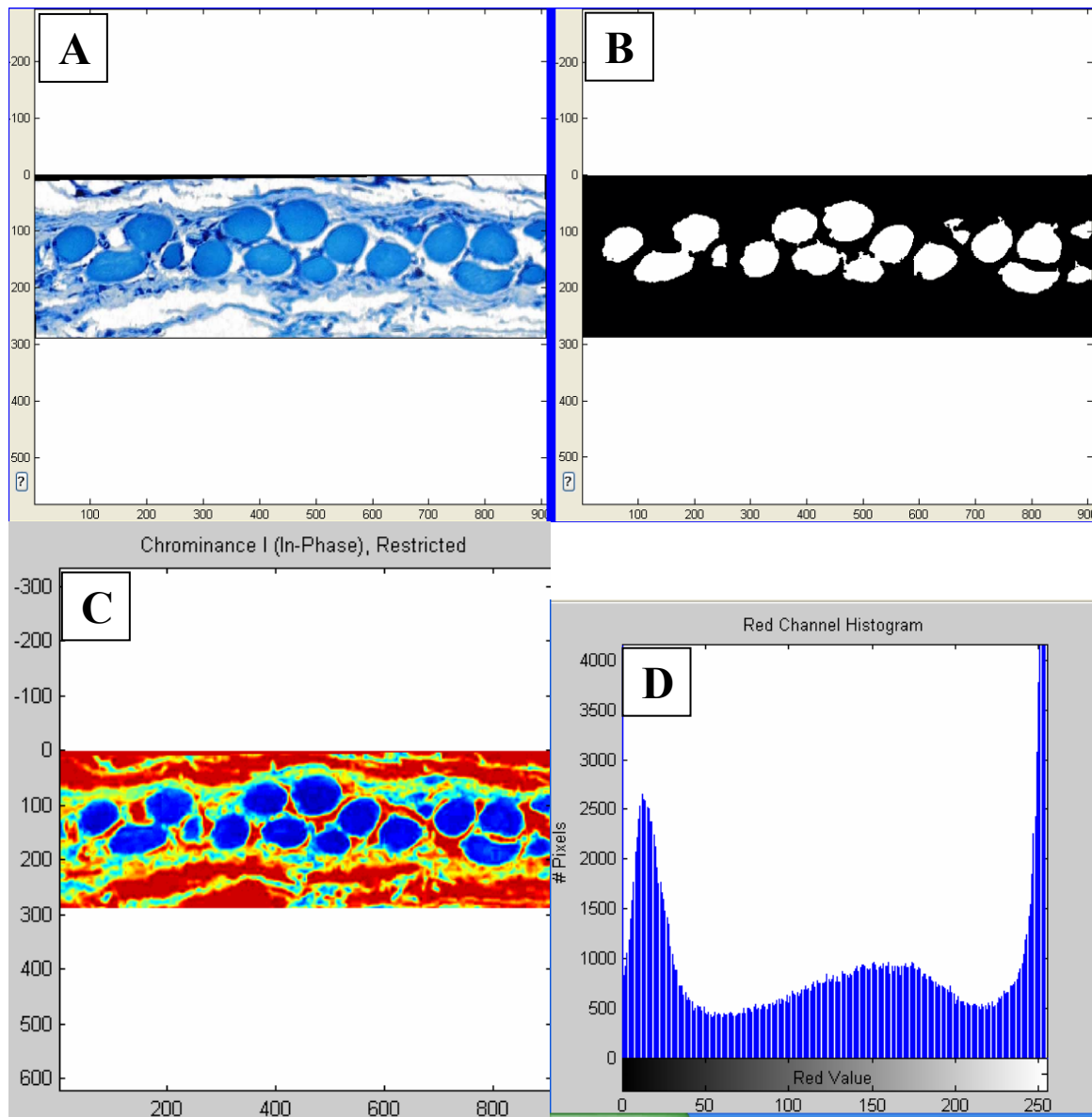


**Figure 6.11** Isolating Muscle Fibers in Giemsa Stained Subcutaneous Tissue Images (A) shows the original image of the subcutaneous tissue on the left (200x), and (B) shows the binary image of the retractor muscle fibers. The Giemsa stain required only a low pass IPC filter (C) and a high pass area filter for the clusters. (C) clearly shows the muscle as having very low IPC values, contrasting it against all background and local nuclei. Without the deep hematoxylin counterstain, it is visible in both (B) and (C) that the nuclei do not interfere with muscle detection, as with the H&E stain. The red channel histogram (D) is included to demonstrate that for a dense feature like muscle, a strong peak (at the left) will be present, aiding determination of color filter criteria. The axes are labeled in pixels, at  $0.52\mu\text{m}/\text{pixel}$ .

#### 6.4.2.5 Microvessels: Masson's Trichrome

Capillary detection in Trichrome stained samples was highly dependent on erythrocytes staining. For oxygen modeling purposes, only actively flowing capillaries would be desirable to include in the model, and the presence of an erythrocyte is a method of defining a capillary as active<sup>(52)</sup>.

Again, in-phase chrominance proved an effective filter (Figure 6.12). In Masson's Trichrome, many nuclei stained slightly reddish, complicating detection, so a low pass filter for blue was used to remove these artifacts (Figure 6.13). Color filters were highly effective in background and collagen removal, but retractor muscle removal required a band pass for area, and in some cases a high pass for solidity. A low pass for eccentricity cleanly removed almost all remaining artifact with respect to capillaries, but could not be used when larger vessels such as venules were present. Manual artifact removal was not generally required unless hemorrhage was present.

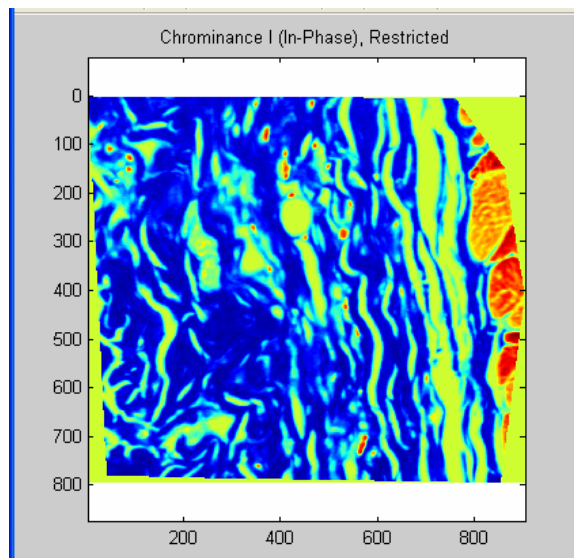


**Figure 6.12** In Phase Chrominance of Masson's Trichrome Stained Subcutaneous Tissue  
The figure shows a pseudo-color image of the in-phase chrominance channel. The erythrocytes appear very clearly as red spots in the tissue, where the retractor muscle at the right stains is colored as intensely, but less evenly. The axes are labeled in pixels, at  $0.52\mu\text{m}/\text{pixel}$ .

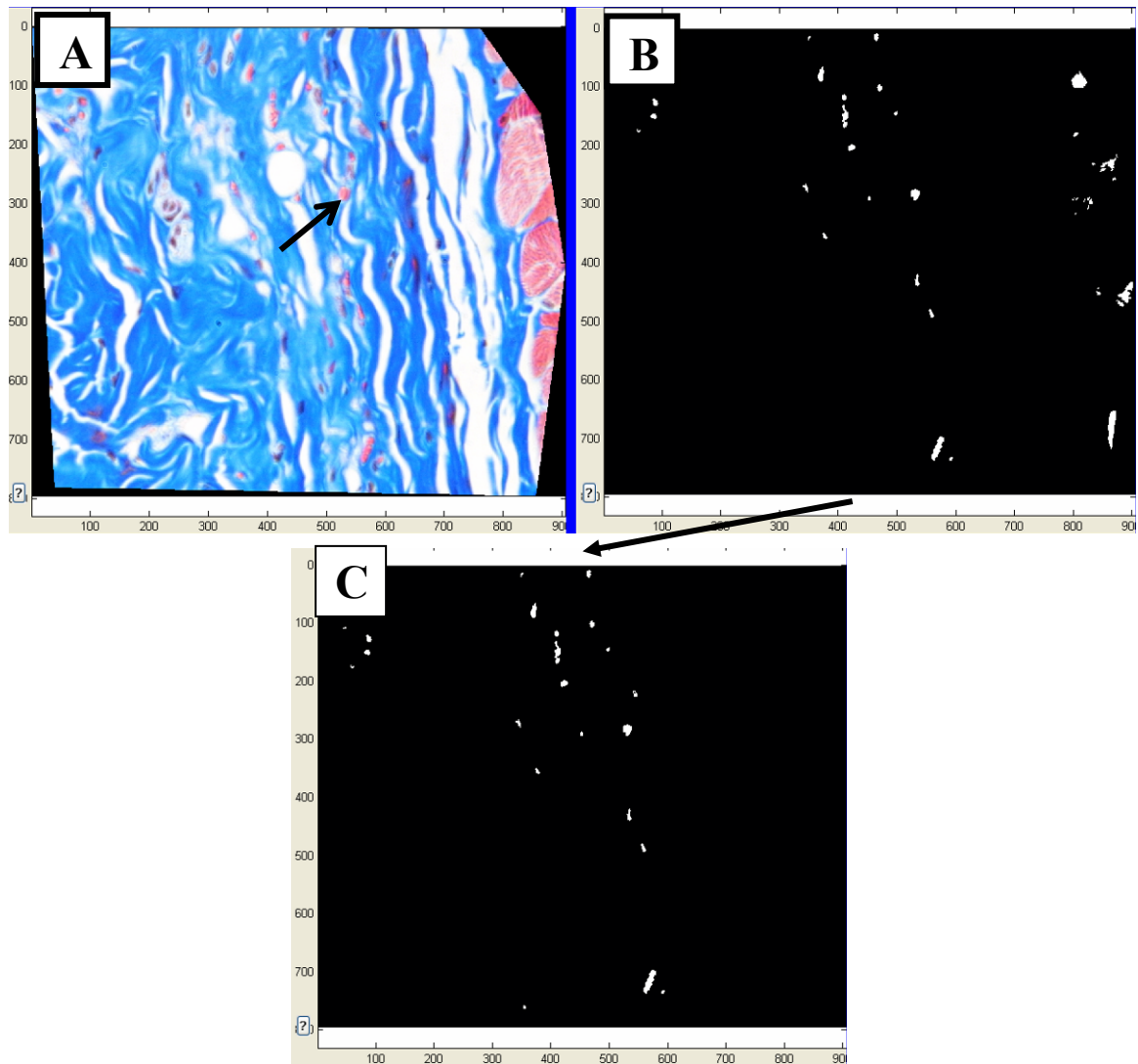


**Figure 6.13** Isolating Erythrocytes in Masson's Trichrome Stained Subcutaneous Tissue Images

(A) shows the original true color image of the stained tissue. An erythrocyte is labeled by the black arrow. The binary image (B) has been filtered using a low pass of the green and blue color channels, and most importantly a high pass of IPC. (C) shows the binary image after a banded area filter. The axes are labeled in pixels, at  $0.52\mu\text{m}/\text{pixel}$ .

The erythrocytes labeled using the determined criteria were  $5.14 \pm 1.77\mu\text{m}$  in diameter, approximately the expected size for erythrocytes constricted by capillary walls. Microscopic observation of the detected features confirmed thin walls around the erythrocytes, further indicating capillaries.

Several tissue samples had small venules where the erythrocytes contained in them were spread out enough to be distinct and were mistaken for capillaries. Clustered erythrocytes were distinguished easily by their size and eccentricity, but a refined algorithm would be needed to identify the walls of venules, perhaps using contrast with the white lumens.

#### **6.4.2.6 Microvessels and Immunohistochemical Stains**

CD-31 anti-endothelial cell labels in paraffin embedded sections of human tumors were used to provide a suitable example for microvascular isolation with the HistoQuant program. The deep brown characteristic to diaminobenzidine staining was partly isolated using a low pass for red coloration, and mostly isolated using an in-phase chrominance high pass filter (Figure 6.14). This isolated most vessels, with a low pass for area removing most artifacts. However, if the vessel perimeter was not solidly stained, the high pass area filter could not be stringent since the vessel wall was broken into smaller sections, and so a dilation and erosion technique was required to define vessel boundaries (Figure 6.14). A high pass for area before dilation and erosion just to remove loose pixels was used, followed by a more stringent area filter after dilation/erosion.

Immunohistochemical stains provide a versatile method of identifying specific cell types and thus are highly worth developing quantification methodology for. In combination with collagen stains to define thicker arterial walls, and with erythrocyte stains to verify vascular perfusion, an anti-hamster cd-31 stain would be an effective tool for characterizing the microvessel content of explanted tissues and applying them to the oxygen diffusion model.

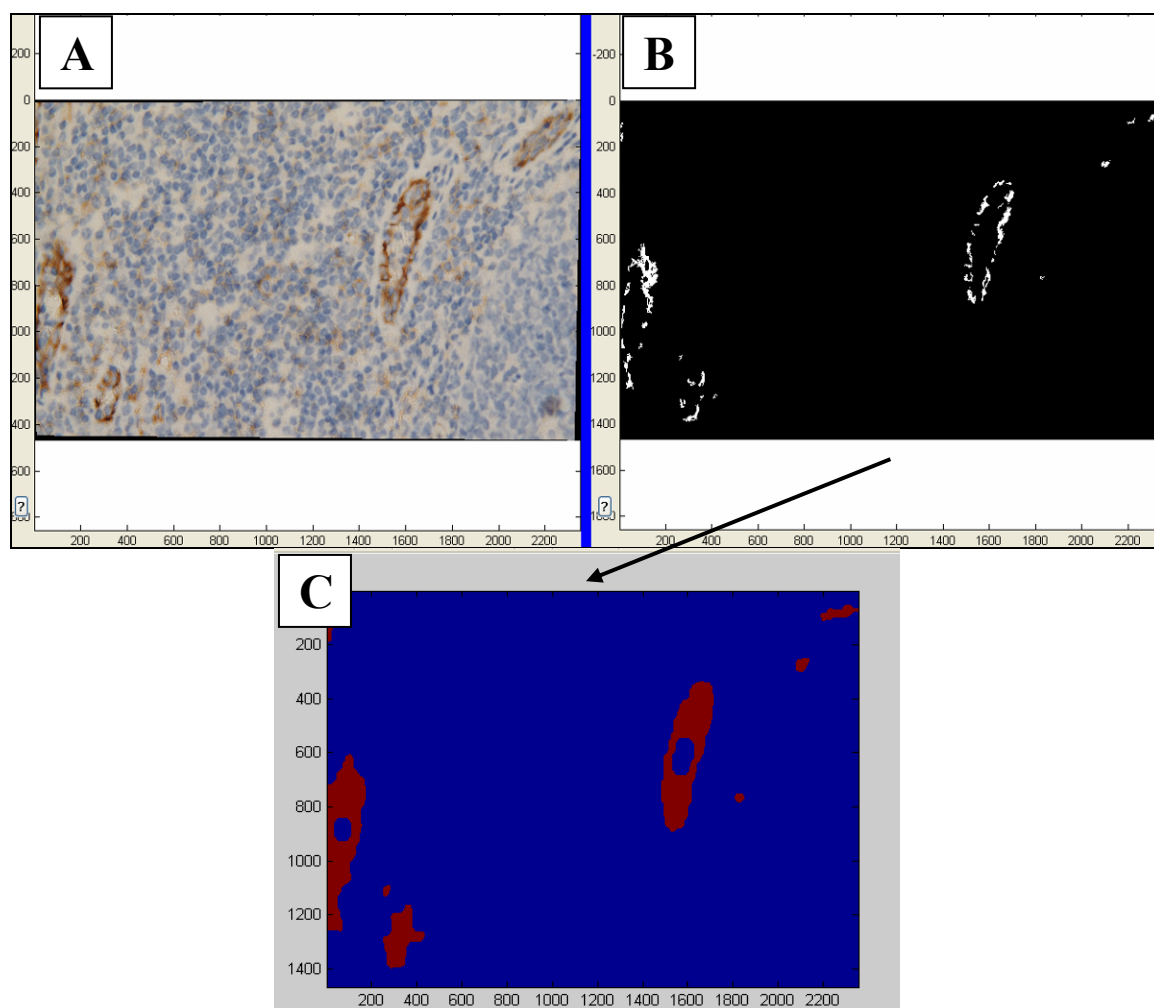


**Figure 6.14** Isolating Endothelial Cells in CD-31 Labeled Tumor Images

The figure shows the isolation of labeled CD-31 antigens on endothelial cells in a section of a human tumor (200x). The labeled cells in this image (B) did not create a solid outline of the vessel, sometimes a problem with IHC brown stains, so compensation was made. The binary isolation image (B) was dilated and then eroded, leaving the solid perimeters seen in (C). From this point the vessels could be filled or skeletonized, depending on whether the image is to be compared to similar section stained for collagen or erythrocytes. The axes are labeled in pixels, at  $0.28\mu\text{m}/\text{pixel}$ .

#### 6.4.2.7 Microvascular Labeling Issues

Larger microvessels and capillaries adjacent to muscle fibers were identifiable with H&E and Trichrome stains. However, for most samples of tissues from PDMS and cellulose implantations, capillaries were not observed in the tissue between the retractor

muscle layer and the biomaterials, potentially due to low contrast with the surrounding tissue. Control H&E stained samples of hamster cutaneous tissue from window-chamber-only implantations showed the presence of some vessels, indicating that neovascularization may not have occurred in the tissues adjacent to biomaterial implants. It has been previously observed that granulation tissue in muscular implants develops less close vascular structures than that in fatty tissues<sup>(97)</sup>. In addition, relatively avascular regions of the skinfold were chosen for the sensor implantations. Thus few large vessels were seen, and neovascularization may have been stunted in the chosen environment.

The immunohistochemical methods explored did not prove effective in labeling hamster microvessels, since anti-hamster labels were not readily available at the time of the experiment and cross-reactivity with available anti-rodent and human CD-31 antibodies was low. At the time of manuscript preparation, at least one company has announced commercial production of anti-hamster labels.

Despite multiple tries and adjustments, alkaline phosphatase staining did not effectively label the microvasculature, producing a yellow coloration in the granulation tissue, but not the red coloration expected to concentrate in endothelial cells. The age of samples may have been a factor, but even tissue sectioned within 2 hours of death did not appear to be properly labeled. PAS stain was likewise unsuccessful in labeling the glycogen concentrations in the vessel lumen. Both of these stains may have functioned poorly due to problems in tissue processing, specifically the use of TFE to stiffen the tissue, which may have caused ice crystal formation or other protein damage. Future samples should be fixed in formalin while still in stretched position and processed using paraffin technique. Cryosectioning, while offering many advantages, is skill intensive.

### **6.4.3 Limitations to Tissue Analysis in Animals with Active Sensors**

Tissue collected from the animals with active sensors experienced a freezing artifact, possibly due to the TFE, that reduced clarity of both the frozen and paraffin sections for those animals. While gross tissue structure and dimensions remain clear, collagen labeling and the other specialized stains studied appear to have been negatively affected. Nuclei were not consistently counterstained. Future work with improved tissue collection methods would circumvent this problem.

### **6.4.4 Variability of Histology**

The most common source of variability in the digitized histology was the staining process. Different batches of H&E stains varied in nuclei staining and the intensity of eosin, especially with respect to erythrocyte staining. Other stains were more consistent. The addition of variations in color intensity due to camera exposure, the lighting of the microscope, ambient light during imaging, and even variations in the color profiles of individual computers introduced small variations in color into the digital histology. Changes in focus during the raster scan of a slide, or due to folds or ripples in the tissue section, frequently altered nuclei and other feature dimensions, blurring the edges and increasing the apparent area of the feature. These many factors support the crucial nature of user input in the quantification process and validated the versatility of the programming.

### **6.4.5 Computational Limits**

Despite the advances in computational technology which allowed this project to be undertaken, there were limitations. The chief limitation was simply a limit to the number of pixels in an image that could be processed. Computers operating on 32-bit

processing systems are limited to 4Gb of virtual memory for access by Matlab and other programs. This means that a section of tissue consisting of 20-40 images taken at 100x magnification (10x objective) with 6 mega-pixel resolution cannot be processed all at once by the HistoQuant program, but rather must be broken up into sections, disproportionately increasing labor. The use of a 64-bit system with highly increased virtual memory vastly improved this consideration, but was insufficient to allow the program to process whole sections above 100x magnification.

Future improvements in random access memory, virtual memory, and processor parallelization would greatly improve HistoQuant's efficiency.

## **6.5 Conclusion**

The HistoQuant program proved to be an effective methodology for versatile analysis of digitized histology. High variations in the samples validated the user guided approach to isolating specific tissue features.

Features with potential impact on oxygen diffusion in the tissue, including capillaries, venules, muscle fibers, collagen, and cell nuclei, were successfully isolated from digital images using the HistoQuant program. These isolations effectively provided spatial maps of the tissue for potential use in an oxygen diffusion model. Combinations of RGB and NTSC color filters, and morphological analysis were utilized. Color filters in the NTSC color space proved particularly useful in isolating many features, including erythrocytes, muscle fibers, and loose connective tissue. However, color filters were insufficient by themselves, and the use of morphological filters, mostly those for feature area, but also those for eccentricity and solidity were capable of removing most artifacts from images. Two manual tools for the removal of artifacts proved necessary in some instances: a tool for selected removal of regions of artifact, and a knife tool which separated adjoining features. In particular, isolation of general nuclei required the knife

tool. Future work would benefit from thinner tissue sections for which nuclei overlap would be reduced.

In the subcutaneous tissues from sensor array implantations in the hamster window chamber, tissue adjacent to different biomaterials was observed to have a different average diffusion path between the biomaterial membrane and the vasculature or musculature, 17.9% higher for PDMS on average. No statistical significance was found for these differences. However, the vascular proximity for each animal was found to be applicable to sensor dynamics, as already discussed in Chapters 4 and 5. It was observed that cellulose membranes were completely penetrated by cellular ingrowth, but only 12.42% of the space around the cellulose fibers was occupied by tissue, mostly adjacent to the PDMS backing layer of the membrane. The process of tissue penetration into the cellulose may explain some of the effects seen in Chapter 2, 4, and 5 with respect to changes in cellulose encased sensor performance over the duration of the implantation.

The ability to quantify histology was validated. However, the quality of the quantification was still dependent on the quality of the histology and thus cannot substitute for good histological practices. Improvements in computational capacity and the expansion of immunohistochemical stains to non-traditional animals such as hamsters will expand future application of the programming techniques described here.

### **6.5.1 Future Programming Directions**

The first programming improvement to be implemented will be the use of feature templating. In templating, an individual feature of interest is chosen by hand, then analyzed for its general color and morphological properties. Each template the program is given helps it to learn what to look for in a feature, reducing the labor required to analyze new features or large images.

## **CHAPTER 7: Quantitative Biocompatibility: Acute Phase Response Protein Assays in Rodent Models**

### **7.1 Abstract**

Two Acute Phase Response proteins, C-Reactive Protein (CRP) and Haptoglobin (Hp), were explored as potential quantitative and specific measures of material biocompatibility in several rodent models. In two separate tests, Wistar rats implanted with cellulose or polytetrafluoroethylene membranes were tested over 7 days for serum levels of CRP and Hp, and Hamsters fitted with window chambers with or without biomaterial membranes were tested over 7 days for serum Hp only. Low volume blood collections were made regularly using a novel quantitative saphenous venipuncture method.

Sample measurements made using the low volume technique were shown to be highly consistent with one another and cardiac puncture samples, allowing for more frequent serum sampling. While, neither C-Reactive Protein or Hp levels showed any discernible pattern over the 7 days in the rat preparation, Hp levels in hamsters responded to microporous biomaterial implantation, showing a clear prolonged relative increase versus the control and window chamber only subjects.

### **7.2 Introduction**

Acute Phase Response (APR) proteins are liver proteins isolable from blood serum<sup>(47, 74, 87)</sup>. These proteins generally circulate at low levels<sup>(69)</sup>, but their presence is amplified dramatically in response to inflammation<sup>(133)</sup>, disease<sup>(73, 146)</sup>, or trauma to the system<sup>(75)</sup>. A commonly cited APR protein is C-Reactive protein, due to its use as a

marker for inflammation and cardiovascular risk assessment<sup>(1, 2, 70, 107-110)</sup>. Recent study has suggested that C-Reactive protein and other APR proteins are important indicators of inflammation in response to adjuvants, drugs, and potentially medical implants<sup>(42, 47)</sup>.

Acute Phase Proteins offer the potential of a quantitative method of measuring biomaterial compatibility over the life of an implant, with frequent sampling that does not require sacrificing the subject<sup>(35, 42, 47)</sup>. This greatly reduces the number of animals required for an experiment.

Even though the CRP structure in rats has been reported to be similar to that of humans<sup>(112)</sup>, reports that rodent CRP may not increase substantially after insult have led researchers to explore additional APRPs that are more responsive<sup>(27, 47, 95)</sup>. In particular, Haptoglobin (Hp), a molecule with high affinity for free hemoglobin, that is present in high amounts during hemolysis, has been suggested as a sensitive marker<sup>(137)</sup>. Hp is known to bind hemoglobin, creating a complex with robust peroxidase properties<sup>(90)</sup> that persist at low pH conditions that normally disable hemoglobin's peroxidase capabilities, thus allowing the presence of Hp to be linked to assays for peroxides. While CRP and other APRPs require immunoassay techniques, quantifying Hp through its enzymatic function offers the significant advantage of a non-species specific assay, allowing a wider range of animal study and a potentially higher correlatability between studies. In addition, enzymatic function testing is significantly faster than antibody methodology since multiple incubations of the testing solutions with the different antibodies is not required.

In this study, the cross reactivity of mouse, rat, hamster, and fat sand rat CRP with Human and Rat monoclonal antibody tests was observed. Serial collections of serum were performed using a novel method of quantitative saphenous serum collection. Using this method, CRP and Hp levels were measured for 1 week in rats following surgical implantation of several biomaterials. Hp levels were also measured in hamsters for 1

week following window chamber and biomaterial implantation. The latter test was intended to approach the question of whether surgical implantation methods or the implant itself has a greater effect on the subject's response to implantation.

### **7.2.1 Relevance to the Dissertation**

This work is relevant to the rest of the dissertation as another quantitative method of analyzing biomaterials with potential application to biosensors. Inflammation caused by material implantation may have an effect on oxygen transfer, especially with regards to vascular flow and extraction properties. Thus, understanding the systemic effects is also important to understanding the impact of biomaterials on oxygen transfer and implanted sensor performance.

## **7.3 Materials and Methods**

### **7.3.1 Animal Samples and Cross Reactivity of CRP Antibodies**

Blood samples were taken via cardiac puncture from white mice, Wistar rats, Gold Syrian hamsters, and fat sand rats 80:20 in heparinized saline (1000u/mL in 0.9% NaCl injectable). The blood samples were centrifuged at 2000rpm for 8 minutes and the serum was removed. Samples were tested for activity using two C-Reactive Protein (CRP) test kits: BioQuant's Human CRP measurement kit and Helica Biosystems Inc.'s Rat CRP measurement kit. Protocols from each of the kits' literature were adopted. The two kits utilize ELISA (Enzyme-Linked ImmunoSorbant Assay) measurement of CRP levels in diluted blood serum<sup>(118, 134)</sup>.

### **7.3.2 Immuno Assay for Human CRP**

Briefly, the sera were diluted 100 fold in the provided diluent, followed by mixture of the diluted serum with goat anti-human CRP antibody linked to horseradish

peroxidase in mouse anti-human CRP-antibody coated plate wells. The resulting complexes of CRP molecule bound between enzymes was washed, and then incubated with tetramethylbenzidine (TMB) development solution. After incubation, acid was used to stop color formation, and a spectrophotometer plate reader was used read the well absorption values at 450nm. Increase in the intensity of coloration is positively correlated to the quantity of C-Reactive Protein bound in the plate well by the CRP antibodies. Plate reader values were observed using an E-Max reader and saved using Soft Max Pro software. A non-linear calibration curve for CRP concentration was generated with the calibration solutions provided in the kit. Two known-concentration control samples from the provided calibrant solutions were run with each overall test to verify efficacy, as well as a negative control of pure diluent solution.

Following early negative test readings, a pure, undiluted serum from the hamster and rat samples were tested for activity.

### **7.3.3 Immunoassay for Rat CRP**

Samples prepared for use with Helica's Rat CRP measurement kit (Helica 951CRP01R) were diluted 4000 fold using the provided Tween 20 mixture. Use of the rat kit was similar to that of the human kit, including the measurement at 450nm. The mouse, rat, hamster, and fat sand rat serum samples were tested for activity along with a sample of the human CRP standard provided in BioQuant's CRP measurement kit. Serum samples diluted only 100 fold were also tested.

### **7.3.4 Quantitative Blood Collection from Saphenous Puncture:**

Saphenous puncture was performed on animal subjects every 2 days during blood serum experiments, using alternating legs. During collection, the animals were restrained, exposing their hind leg for shaving, sterilization and with betadine, and preparation with a thin coat of silicone grease to increase fluid beading. Tubes of

heparinized saline 1000u/mL and Pipetmen with heparin soaked wide mouth tips were prepared. Venipuncture was used to collect 10-50 $\mu$ L of blood, which was immediately injected into a tube with the proper amount of saline for an overall 100 fold dilution. Blood-air contact was avoided. Tubes of diluted blood were mixed by inversion and centrifuged for 8 minutes at 2000rpm with gentle acceleration and deceleration before collecting serum.

For several rats, samples were taken from the same animal on both legs and from cardiac puncture to verify the consistency of serum measurements. All other animals had samples collected by cardiac puncture just prior to sacrifice for comparison to the most recent saphenous sample.

### **7.3.5 Biomaterial Implantation: CRP and Haptoglobin in Rats**

A group of 4 sibling Wistar Rats weighing 358 $\pm$ 29g was obtained, separating one animal out as a control. The three experimental animals were anesthetized with 50mg/kg Ketamine HCl and 125 $\mu$ g/kg Medetomidine HCl intraperitoneally, then prepped for surgery by shaving and sterilizing two regions 2cm to either side of the spine and 1cm anterior to the scapula. Longitudinal incisions were made in the shaved regions and pockets were created against the skeletal muscle using blunt dissection. One animal had 12mm diameter circles of microporous PTFE (MilliPore, 10 $\mu$ m exclusion) implanted in each pocket, another had 12mm circles of porous cellulose (Whatman #2, 8 $\mu$ m exclusion) implanted, and the last animal had nothing implanted as a sham surgery. The incisions were sealed with Vetbond veterinary adhesive, treated with topical antibiotic, and the wound sites sealed inside a high adhesion bandaid.

Following surgery, all animals had blood drawn by saphenous venipuncture as described above. Buprenorphine HCl, 5 $\mu$ g/kg, was administered pre-recovery as an analgesic, while Atipamezole HCl, 0.5mg/Kg was given as a competitive antidote to the Medetomidine to aid recovery.

Saphenous draws were taken from all animals 3, 5 and 7 days following surgery, with 25% of the original surgical dosage of Ketamine/Medetomidine to briefly calm the animal. Venipuncture sites were alternated. Each sample was immediately diluted, centrifuged and tested using the rat CRP kit and a non-species specific haptoglobin test from Tridelta Diagnostics (Kildare, Ireland).

### **7.3.6 Haptoglobin Assay for Hemoglobin Peroxidase Activity**

The Hp measurements were made according to the instructions in TriDelta's product insert. Briefly, 7.5µL of serum from each sample was mixed with 100µL of Tridelta's hemoglobin/diluent solution in sterile 96-well-plate wells. Then, 140µL of stabilized hydrogen peroxide based chromogen solution was added. After exactly 5 minutes of incubation, measurements were made at 590 and 650nm on a plate reader. This differed from the suggested 630nm due to equipment limitations.

### **7.3.7 Biomaterial Implantation: Haptoglobin in Hamsters**

Four sibling Gold Syrian Hamsters weighing 208±6g were obtained, separating one animal out as a control. The experimental hamsters were anesthetized using 100mg/kg Ketamine HCl and 250µg/kg Medetomidine HCl intraperitoneally, then had window chambers implanted following the procedures of Makale et al<sup>(86)</sup> and Chapter 2. One animal was chambered with a 12mm circular PTFE implant inside the chamber, another with a cellulose implant and another with only the glass cover slip.

All four animals had blood drawn by saphenous venipuncture as described above. The total dilution ratio was 99:1 saline to whole blood. Buprenorphine HCl and Atipamezole HCl administered in the same dose as for rats.

Saphenous draws were taken from all animals 3, 5 and 7 days following surgery, with 25% of the original surgical dosage of Ketamine/Medetomidine. Venipuncture sites

were alternated. Each sample was immediately diluted, centrifuged and tested using Tridelta Diagnostic's Haptoglobin kit as described in the previous section.

## **7.4 Results and Discussion**

### **7.4.1 Methods Results**

#### **7.4.1.1 Cross Reactivity**

Cross reactivity of the rodent samples with the human CRP kit was seen to be negligible. Similarly, only the rat serum show activity with the rat CRP kit even when full strength serums from the hamster and fat sand rat were assayed. Since these early experiments, lack of cross-reactivity has been established in other studies.

#### **7.4.1.2 Rat CRP: Nonlinearity of Measurements and Dilution**

The normal rat serum samples, assayed 4000 fold diluted with the rat CRP kit, showed values inside the expected curve, with absorbance of 0.238-0.265 corresponding to 26.5-32.1 $\mu$ g/mL CRP as determined by the logarithmic control curve.

The 100 fold dilution serum showed absorbance of 0.338-0.388, corresponding to 53.9-77.0 $\mu$ g/mL. The relationship between the dilution of the samples and the measured concentrations was not consistent with the logarithmic control ladder, being off by a factor of 18. Increasing dilution two fold corresponded to an average decrease of only 28.9%. Serum was consistently observed to not follow the dilution curve, which was generated by a ladder of 6 separate standards, as opposed to serial dilution of a single standard.

#### **7.4.1.3 Quantitative Blood Collection from Saphenous Puncture**

Animals responded well to the serial blood collections, with saphenous veins recovering very well in each two day time frame. For measurements involving dilute serum, this method of pre-diluting whole blood prior to centrifugation allows more frequent collections of blood than previous more invasive methods like cardiac puncture and catheterization, and therefore a more complete picture of post procedure protein levels. Important elements of the methodology are the thin grease layer and clean post-puncture compression to preserve site integrity. Additionally, for haptoglobin, strong care was taken to avoid hemolysis in collected samples, since haptoglobin binds to free hemoglobin. Gentle treatment of blood samples, low shear in the pipette tip, early separation of the serum from the whole blood, and low air contact should all be observed.

Given the high sensitivity of CRP measurements to variations in dilutions, consistency in dilution amounts throughout an experiment is also highly suggested for all serum protein measurements

#### **7.4.1.4 Calibration Curves: Form and Sensitivity**

Both the CRP and Hp curves were strongly linear for a plot of optical density versus  $\text{Log}_{10}$  of protein concentration. The CRP curve had an  $R^2$  of 0.9994 over the range of the rat test samples, while that of the Hp had an  $R^2$  of 0.9979 in the range of the Hamster test samples. Minimum optical density for both tests was non-zero and thus both curves displayed an S-shaped change of inflection near zero concentration, which was more pronounced in the Hp test. This rat Hp samples, especially those under 0.25mg/mL, to have large variations in calculated protein for very small changes in absorbance. This region was approximated by a quartic curve found in Excel, and so protein concentrations were solved for using Mathematica (v5.0 Wolfram).

The calibration curve produced for Hp at 650nm had lower sensitivity than the curve for 590nm, due to lower overall optical densities. Though the curves were almost identical in shape, the 590nm curve was used for all calculations.

#### **7.4.1.5 Comparing Blood Collection Sites**

Samples taken by saphenous and cardiac puncture were shown to have consistent optical density readings for Hp ( $1.37 \pm 0.38\%$ ,  $n=3$ ), as did samples from different legs ( $3.55 \pm 2.75\%$ ,  $n=6$ ). Measurements for CRP were still reasonably consistent between cardiac and venipuncture samples ( $10.9 \pm 4.74\%$ ,  $n=3$ ) and between venipuncture samples from different legs ( $9.48 \pm 8.92$ ) (Table 7.1). These results compare well to pre-surgical variations between animals of 5.21% for CRP and 8.30% for Hp.

Due the S-shape in the calibration curve near zero concentration, especially for Hp, errors in the actual calculated serum concentrations become higher the lower the tested range. This was a greater issue for measurement of Hp in the rat preparation, which had lower serum concentrations than for hamsters. In particular, the difference between opposite leg venipuncture samples below 0.17mg/mL was 18.5% versus 3.97% for those above 0.17mg/mL (Table 7.1). Conversely, the standard deviation of calculated pre-surgical hamster Hp, all of which were above 0.25mg/mL, was lower than the standard deviation of the optical densities.

### **7.4.2 Biomaterial Implantations**

#### **7.4.2.1 Biomaterial Implantation: CRP in Wistar Rats**

As a whole, over the 7 days following surgery, the CRP levels of the animals were variable and did not follow a discernible pattern with respect to surgery or biomaterial implantation (Figure 7.1). Human CRP levels have been reported to rise significantly within 24 hours in cases of surgery and acute inflammation<sup>(58)</sup>. The current

preparation may not have approached this level of insult, the insult may not have been sufficiently greater than saphenous venipuncture, or alternately, rat CRP mechanisms may not respond to the same degree as human mechanisms as suggested by the previous literature.

**Table 7.1** Variation of Serum Measurements: Different Test Sites, Animal Populations  
(A): Differences, as a percent of averages, for optical densities and protein concentrations between samples taken from different sites. Pairs of samples from the same animal, opposite saphenous veins, and from the same animal, saphenous versus cardiac puncture, are shown.  
(B): Standard deviations, as a percent of average, for optical densities and protein concentrations in pre-surgical and control animal populations.

<b><u>Table 7.1: Comparison of CRP and Hp Measurements Between Test Sites and Within Populations</u></b>			
<b><u>A: Difference Between Comparison Samples as a Percent of Average</u></b>			
<b><u>Difference between comparison samples</u></b>	<b><u>N pairs</u></b>	<b><u>StDev in Optical Density</u></b>	<b><u>StDev in Calculated Concentration</u></b>
<b>Rat CRP</b>			
Same animal different Legs	6	10.8±4.74%	19.7±8.1%
Same animal, saphenous vs. cardiac puncture	3	9.48±8.92%	16.0±12.9%
<b>Rat Hp</b>			
Same animal different Legs	6	3.55±2.75%	13.7±12.8%
Leg-Leg below 0.17mg/mL	4	4.47±2.96%	18.5±13.4%
Leg-Leg above 0.17mg/mL	2	1.71±1.19%	3.97±2.61%
Same animal, saphenous vs. cardiac puncture	3	4.40±2.51%	22.0±9.7%
<b><u>B: Group Standard Deviation as a Percent of Average</u></b>			
<b><u>Standard Deviation Within Populations</u></b>	<b><u>N</u></b>	<b><u>StDev in Optical Density</u></b>	<b><u>StDev in Calculated Concentration</u></b>
<b>Rat CRP</b>			
All rats pre-surgery	5	5.21%	9.64%
Control samples throughout experiment	5	12.50%	23.40%
<b>Rat Hp</b>			
All rats pre-surgery	5	8.30%	41.90%
Control samples throughout experiment	5	2.10%	25.10%
<b>Hamster Hp</b>			
All hamsters pre-surgery	4	10.00%	6.76%

#### 7.4.2.2 Biomaterial Implantation: Haptoglobin in Wistar Rats

The day following surgery, Hp levels in the rats all increased. However, following this initial concerted increase, Hp levels in the rats over the remainder of the experiment did not follow a discernible pattern (Figure 7.2). Control Hp levels increased throughout the experiment, potentially indicating that Hp measurements, when the sample range is low, are sensitive to the hemolysis induced by venipuncture.

#### 7.4.2.3 Comparison of Rat CRP and Haptoglobin Levels

Pre-surgical magnitudes of CRP and Hp for each animal followed approximately the same rank and relative range, potentially indicating that baseline CRP and Hp levels are related. However, following surgery, the rank of each group's magnitude switched frequently and did not follow the same pattern for CRP and Hp.

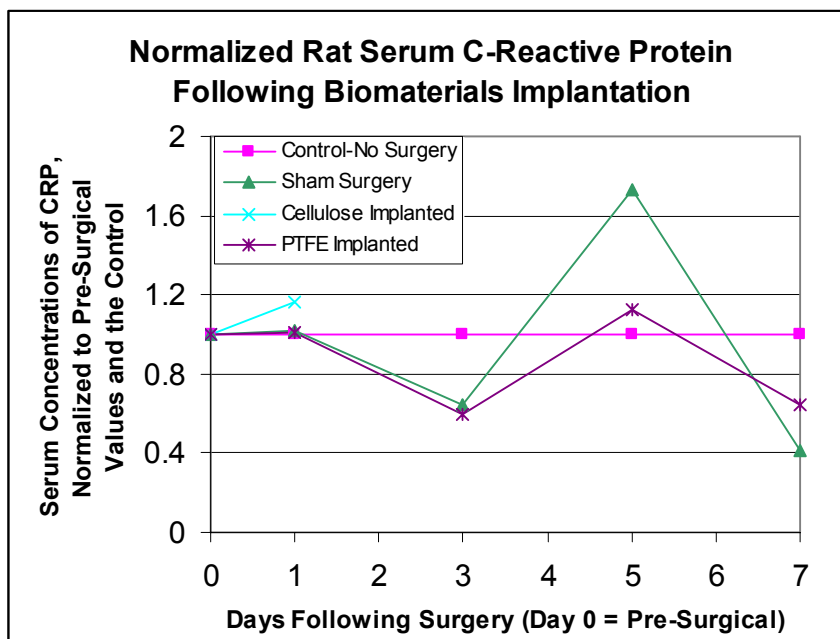


**Figure 7.1** Rat C-Reactive Protein Following Implantation of Biomaterials

The figure shows a plot of serum concentrations of C-Reactive Protein in rats for 7 days following biomaterial implantation, with each animal's values normalized to pre-surgical measurements (Day 0), and then to the control. No distinguishable pattern was observed. The cellulose animal was removed from the study after day 2 for unrelated reasons.

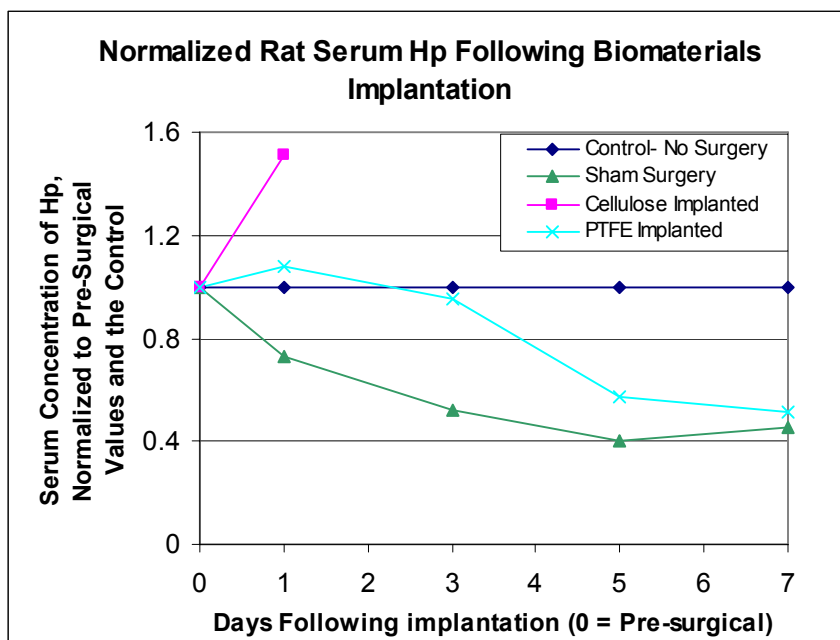


**Figure 7.2** Rat Haptoglobin Following Implantation of Biomaterials

The figure shows a plot of serum concentrations of Haptoglobin in rats for 7 days following biomaterial implantation, with each animal's values normalized to pre-surgical measurements (Day 0), and then to the control. No distinguishable pattern was observed. The cellulose animal was removed from the study after day 2 for unrelated reasons.

#### 7.4.2.4 Biomaterial Implantation: Haptoglobin Hamsters

The day following surgery, Hp increased for all hamster groups. The trend for the overall experiment was also an increase in Hp levels for all groups including the control. The trend of greater increases for the biomaterial implanted animals is discernible in the raw data. However, when Hp concentrations were normalized to each animals' pre-surgical values, and then to the control values for each day, the trend becomes obvious and significant (Figure 7.3). All window chambered animals showed significant and prolonged elevation of Hp relative to the control ( $P < 0.0094$ ). Microporous biomaterial implanted animals showed a further significant increase over the window chamber only group ( $P < 0.0038$ ), indicating greater inflammation or a prolonged hemolytic environment. There was no significant difference between the two microporous

biomaterials in the first 7 days, but future experiments over longer periods may demonstrate changes in the time course of Hp elevation for these and other materials.

Enzymatic function test results by nature are dependent on the time at which the samples are measured and can vary by environmental conditions. Thus, calibration samples should be run regularly, and values should be normalized for relative rather than absolute comparison. However, the benefit of plotting normalized profiles over time is that the error due to animal to animal variation in baseline values is reduced. Change in serum protein levels, rather than absolute values, are measured.

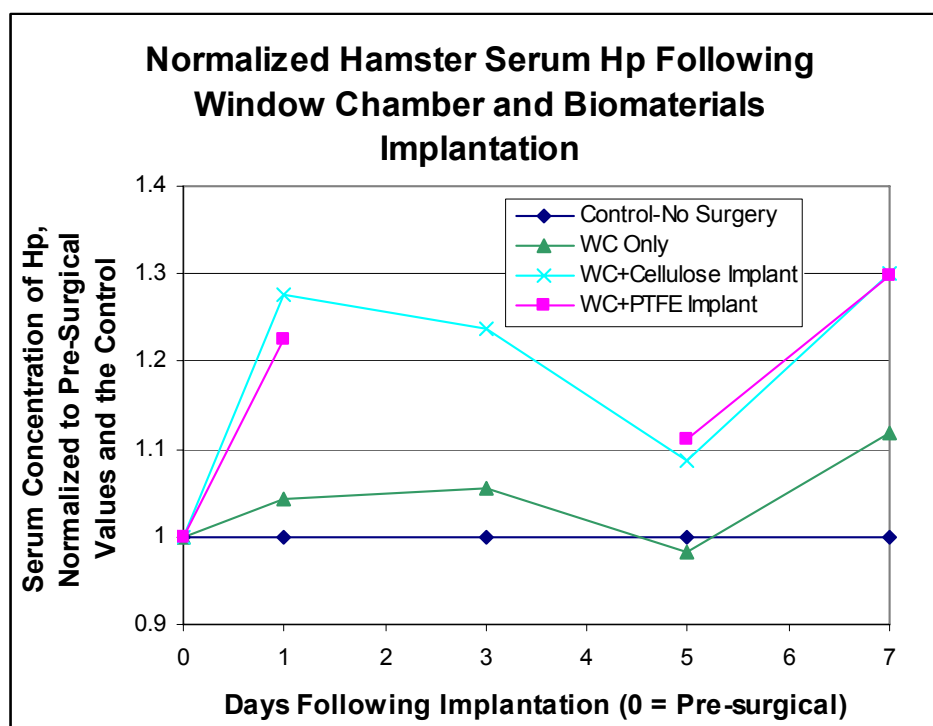


**Figure 7.3** Hamster Haptoglobin Following Window Chamber and Biomaterial Implantation

Normalized serum concentrations of Haptoglobin in hamsters are shown for 7 days following window chamber and biomaterial implantation, with each animal's values normalized to pre-surgical measurements (Day 0), and then to the control. The microporous biomaterials experience a rapid and prolonged elevation in concentration relative to the control and the window chamber only group. The window chamber only group had elevated levels relative to the control group.

## 7.5 Conclusions

C-Reactive Protein and Haptoglobin measurements were found to be highly consistent when taken from different veins or cardiac puncture, validating the saphenous methodology. However, CRP measurements were found to be highly sensitive to dilution ratios. Rat Hp levels were on the low end of the measurement method's sensitivity and were very sensitive to measurement timing. Measurements made in the non-linear portion of the calibration curve were more difficult to interpret, suggesting future experiments use consistent, lower dilution levels.

Neither C-Reactive Protein or Hp levels showed any discernible pattern over the 7 days in the rat preparation. However, Hp levels in hamsters responded to microporous biomaterial implantation, showing a clear prolonged relative increase versus the control and window chamber only subjects. In particular, the result that microporous biomaterials elicited an increased Hp response relative to the titanium and glass experienced by the window-chamber-only group warrants further investigation. Additionally, the elevated protein profiles had not settled by the end of 7 days, suggesting longer time frames for future studies. Longer studies may also help to define differences between biomaterials that elicit similar acute responses such as the microporous membranes observed here.

Serum protein measurements were validated in this study as a quantitative marker of biomaterial compatibility, though CRP measurements did not appear to be as effective in rodents. Future experiments with other markers, such as fibronectin, larger animal groups, and a wider variety of biomaterial implants are a natural progression of this work, potentially leading to more specific definitions of compatibility based on application. Since the different serum proteins each respond to a slightly different element of tissue inflammation, such as Hp to free hemoglobin, multi-protein profiles may be an effective way to understand how different biomaterials specifically affect their tissue environment.

## **CHAPTER 8: Conclusions of the Dissertation**

### **8.1 Conclusions**

The performance of implanted oxygen sensors was affected by the presence of biomaterials. This was most clearly evidenced by higher signal magnitude for sensors encased in PDMS than those encased in cellulose for the first 7 days of implantation, with the greatest differences observed to occur between days 4-7. Following day 7 until day 14, the differences between the magnitudes of the differently encased sensors diminished, though PDMS sensors retained systematically higher values. The increase in cellulose encased sensor magnitude may have been due to tissue ingrowth into the cellulose that was observed histologically to be complete by day 14. The majority of the disparity between PDMS and cellulose encased sensor signals appeared following implantation and following day 4, suggesting a connection to changes in the tissue following the same timeline. In addition, all sensor signals were higher on day 14 than day 7, implying either better contact with the tissue or improved convective transfer of oxygen to the implant site for both materials.

The disparity in signal magnitude for PDMS and cellulose encased sensors was observed to be disproportionately lesser in during hypoxic exposure, where the advantage of PDMS to signal magnitude was lessened. Overall, the sensitivity of sensors to exogenous oxygen was more linear than expected at lower oxygen concentrations. Cellulose encased sensor were observed to have higher signal noise, which is not advantageous, but at lower exogenous oxygen concentrations, though noise increased for sensors encased in both biomaterials, the noise for PDMS encased sensors became relatively greater. Thus, the projected oxygen levels in the implant site are worth taking into consideration when making choices in sensor materials.

Comparison of sensor array function *in vitro* before and after implantation in the hamsters validated that implantation had not significantly affected the sensitivity of the sensors. However, changes in the variance of the sensitivity suggest that there were issues with sensor hydration that may need to be addressed for future application of sensors utilizing hydrogel media.

Sensor dynamics and challenges proved to be a potentially useful tool in studying oxygen diffusion characteristics *in vivo*. Curve fittings methods were effective and the resulting time constant calculations allowed comparisons of sensor dynamics for sensors encased in different biomaterials. The results showed that while materials significantly affected sensor dynamics *in vitro*, the effect diminishes *in vivo*. Cellulose still had lower time constants during the implantation, but a stronger correlation between vascular access and time constants was found than between biomaterials and time constants, implying tissue to be dominant over materials in limiting diffusion to the sensor. Vascular proximity was correlated to a lesser extent to the delay in sensor response to challenges, but also interestingly to the shift-directional ratio, an indication of the relative resistance to oxygen increases versus decreases in the tissue. The SDR was not affected by biomaterials *in vitro*. Larger SDR larger values in thinner tissue implied that mechanisms restricting oxygen loss in the tissue are largely vascular.

Oxygen diffusion constants estimations for the diffusion path to the sensor arrays were found to be on the expected order of magnitude, as were estimates of diffusion in the PDMS. The cellulose membranes were determined to have almost two orders of magnitude higher resistance to diffusion *in vitro*. Determination of tissue diffusion constants was complicated by possible changes in membrane diffusion *in vivo*.

Observations of serial oxygen challenges indicated that dissolved oxygen in both the biomaterials and the tissue may contribute to the sensor signal, and that following depletion of dissolved oxygen, temporary flux imbalance may reduce the sensor signal

magnitude. *In vitro* the effect was seen to be proportional to the size of the step reduction in oxygen, and reversible with exposure to elevated oxygen. *In vivo*, sensor signal magnitudes were reduced significantly following exposure of the animals to hypoxic condition, with continued loss of magnitude on repeated challenges. *In vitro* this loss of magnitude was seen to be greater for cellulose encased sensors, but *in vivo*, on days 7 and 14, there were no difference seen due to biomaterial encasement. Time constants for the sensor response were increased by hypoxic exposure and rose dramatically during multiple cycles of oxygen challenge. This implied a potential active reaction of the tissue to hypoxia such as increased vascular activity. These results demonstrated path rather than just state dependency of sensor signal and dynamic performance.

Quantification of tissue features with color and morphological feature identification and filtration proved to be highly effective and versatile. The HistoQuant programming was used to successfully create spatial maps of vasculature, general cells, inflammatory mast cells, muscle fibers, and collagen. Color and morphological parameters for isolating these features were established for future studies.

Observations of the tissue from biomaterial membranes with HistoQuant demonstrated thicker granulation tissue adjacent to PDMS as well as lower numbers of mast cells relative to cellulose tissues. The other major observation was the total penetration, but not occupation of the cellulose membranes by loose connective tissues, which accumulated at the interface between the cellulose and the PDMS backing. Limitations in the explanted histology from animals with active sensors, due to tissue processing errors, prevented further comment on tissue characteristics, excepting structural ones, such as measurements of the distance from the membrane to the nearest vasculature, generally designated by the distance to the retractor muscle.

Serum measurements in hamsters implanted with microporous membranes demonstrated elevated haptoglobin levels relative to the control and to window chamber

implanted animals over 7 days. The serial quantitative blood collection method was validated as consistent, comparable to past methods, and effective in acquiring samples. The observations that rat CRP and haptoglobin did not follow a specific pattern may indicate the need for larger numbers of subjects or a more reproducible surgical preparation.

Overall, oxygen transfer in the implant environment was studied through the use of implanted sensors, dynamic challenges, and quantitative histology. The methods were validated and showed several clear differences between the performance of sensors encased in different biomaterials and helped to characterize some of the mass transfer properties of the tissue environment. Sensor dynamics, especially the time constant and the shift-directional ratio were also shown to be potential methods of estimating the vascular access of implanted devices and the solubility and diffusion constants for the tissue surrounding the device.

## **8.2 Future Directions**

This work suggests that the sensor implantations should be studied in their more acute state, taking histological samples at 7 days with more frequent data points for sensor acquisitions. In addition, experiments with deeper hypoxia, vasoactive compounds or compressive ischemia would provide further insight into the origins of the differences seen in diffusion around different biomaterials. Expansion of the experiment to larger animals with thicker skin is suggested to reduce the impact of diffusion through the skinfold. Finally, the use of the sensor to drive local hypoxia, its effect on tissue, and the modulation of that effect by biomaterials is a potential future direction.

Studies of other biomaterials such as smooth versus expanded PTFE, and studies of other analytes such as glucose and lactate are a logical progression of this work.

## APPENDIX A: Step Shift Curve Form Derivation

The original derivation of this equation was performed by Lucas Kumosa<sup>(72)</sup> (UC San Diego Bioengineering, PhD Student).

### The Model and Initial Conditions

The equation was originally derived for step shifts in concentrations of gases mixing in a fixed volume space, with a specific inlet and outlet, such as the flask used in sensor calibrations. The gas concentration at the outlet is a function of the concentration at the inlet and of the flow of gas through the chamber, assuming fixed pressure. This outlet concentration represents the mixed gas of the chamber and thus the current state of chamber concentration. The mass balance, where  $C_E$  is the concentration at the inlet and  $C_S$  is the concentration at the outlet, is...

$$C_E U - C_S U = \left( \frac{\partial C_S}{\partial t} \right) V$$

$U$  represents flow through the openings and  $V$  the volume of the fixed space, while  $t$  is time.

For a diffusion limited situation, the diffusion represents flow. The far more rapid convective events are dominated and thus no longer contribute to the curve form. Such a situation is diffusion of oxygen through the tissue to the sensor, following extraction from the microvasculature. In this case,  $C_E$  becomes the extracted oxygen concentration or that at the external surface of the vasculature.  $C_S$  is the concentration at the sensor. Volume becomes that of the diffusion path, while flow, as suggested, is diffusion. For a two dimensional model, thickness can be factored out, leaving  $\tau c$  as the ratio of the diffusion rate and the area of diffusion.

Derivation of the curve form now involves solving the mass balance equation for  $C_S$ . The first step of which is to factor out  $U$ , and to rearrange the scalar values.

$$\frac{U}{V} = \left( \frac{1}{C_E - C_S} \right) \frac{\partial C_S}{\partial t}$$

Variables are then separated.

$$\frac{U}{V} \partial t = \left( \frac{1}{C_E - C_S} \right) \partial C_S$$

Both sides are prepared for integration, with respect to time and concentration.

$$\int_{t_o}^t \frac{U}{V} \partial t = \int_{C_{S_o}}^{C_S} \left( \frac{1}{C_E - C_S} \right) \partial C_S$$

$C_{S_o}$  is the original value of oxygen at the sensor.

The equations are then integrated. The left hand side is simple, but the right hand side uses an identity for the integral of a denominator with a scalar addition<sup>(37)</sup>.

$$\frac{U}{V} (t - t_o) = \ln \left( \frac{C_E}{C_E - C_S} \right) - \ln \left( \frac{C_E}{C_E - C_{S_o}} \right) = \ln \left( \frac{C_E - C_{S_o}}{C_E - C_S} \right)$$

Solution of the equation for  $C_S$  yields the following equation.

$$C_S = \exp^{\frac{-tU}{V}} (C_E * \exp^{\frac{tU}{V}} + -C_E * \exp^{\frac{t_o U}{V}} + C_{So} * \exp^{\frac{t_o U}{V}}$$

This can be simplified by multiplying out the first exponential term, and then factoring. The final form is a simple exponential equation.

$$C_S = C_E - C_E * \exp^{\frac{(-t+t_o)U}{V}} + C_{So} * \exp^{\frac{(-t+t_o)U}{V}} = C_E - (C_E - C_{So}) * \exp^{\frac{(-t+t_o)U}{V}}$$

We then find that the time constant is equal to  $U/V$  and acts to modify  $-\Delta t$  in the exponent, accelerating curve resolution as it increases in magnitude.

$$C_S = C_E - (C_E - C_{So}) * \exp^{(-t+t_o)\tau_c}$$

The final curve form has a maximum value of  $C_E$ , but in the tissue,  $C_E$  is theoretically never achieved due to cellular consumption and other factors. So ultimately,  $C_S$  approaches some steady state maximum below that of the local microvasculature, and  $C_{Smax} = C_E - C_X$ , where  $C_X$  represents tissue factors that limit maximum oxygen concentration. This assumption does not, however, change the shape of the function.

Another potentially complicating factor is that  $U$  may be affected by vascular factors such as flow rate, functional capillary density and the rate of extraction of oxygen from hemoglobin. While none of these alter the pure diffusion rate, they may create an increase in the amount of oxygen passing through the tissue, increasing the apparent flow rate.

# **APPENDIX B: Time Constants from Discretely Sampled and Incomplete Curves, Application to Algorithms**

## **B.1 Introduction**

An additional factor that may limit the use of dynamic information in diagnostic or predictive algorithms involves the accuracy of curve fitting. For the sake of practical application, this study will explore the effect of curve extent, sampling frequency, and specification of endpoint values, on time constant calculation.

Curve extent defines the amount of the beginning and end of each curve that is included in calculations. Greater curve extent indicates that fewer points are being overlooked.

Sampling frequency is a concern of computational cost. More samples require more energy for collection and computation. In implanted applications, lower sampling frequencies allow longer battery life and thus less potential for battery replacement surgery. Thus, it is optimal to find the lowest sampling frequency which allows curve fitting to real world data.

Specification of endpoint values is partly an issue specific to the use of nonlinear regression methods. For curve fitting, a curve form or function can be suggested which the regression fits to the raw data using least squared methods. The curve fit is more rapidly achieved and less likely to blow up if the first and last point of the function are specified. However, due to the uncertainty inherent to real world situations, the endpoints of a curve may be difficult to identify, especially when curves overlap or fail to completely resolve.

While the concepts discussed so far are not novel to algorithm design and have been theoretically explored, this study provides a methodical analysis of actual sensor data and will hopefully offer insight to more in-depth studies or a starting point for future algorithm design.

## **B.2 Materials and Methods**

### **B.2.1 Comparing Specified and Calculated Initial Signal Magnitudes (Voltages), and the Effects of Curve Length**

To determine the magnitude of artifact due to curve extents,  $\tau_c$  was calculated during incremental removal of points from each end of several calibration curves. In addition,  $\tau_c$  was calculated for several curves with specified initial magnitudes,  $V_o$  values, and compared to  $\tau_c$  values calculated by nonlinear regression without specified initial signal magnitudes.

### **B.2.2 Determining the Effect of Sampling Frequency on Curve Fitting**

The time constants for sixteen electrode calibration curves sampled every 4.375 seconds were calculated in Mathematica, without specified initial signal magnitudes. Sum of the least squared error between the raw data and the fit curve was also calculated with each  $\tau_c$ , and normalized to the number of samples taken for the curve. The

sampling frequency was then iteratively reduced by a factor of 2, repeating the time constant and error calculations each time, until only 3 points were taken. Both normalized error per sample and time constants were separately plotted as a function of the number of samples taken per curve (Figures B.1 and B.2).

### **B.3 Results and Discussion**

#### **B.3.1 Comparing Specified and Calculated Initial Voltages, and the Effects of Curve Length**

For 16 calibration curves consisting of 100 points, removal of points at the beginning of the curve slope exhibited a stronger effect on error and time constant values than removal of points near the end of the slope. This is logical given that the raw data fit exponential curves, where the initial slope is by nature far greater than that near the end. Removal of 5 and 10 points from the beginning of the curve respectively caused systematic  $41.3 \pm 7.6\%$  and  $91.5 \pm 16.7\%$  increases in the time constant, making the curves appear to resolve much more quickly. However, removal of up to 25 points from the end of the curve resulted in a decrease of calculated time constants of less than  $0.01 \pm 0.02\%$ . Once the curve began to resolve, if a final signal magnitude was specified, time constant calculations were fairly consistent regardless of how many points remained.

Failure to specify the final signal magnitudes,  $V_1$  values, increased error and reduced consistency of time constant calculations. To the contrary, using Mathematica to determine initial signal magnitudes ( $V_0$ 's) rather than specifying them, resulted in relatively small change in the time constant calculations, and more robust calculations for the removal of early points on the curve. Time constant calculations increased by only  $14.5 \pm 6.0\%$  and  $14.7 \pm 12.0\%$  respectively, for removal of the same 5 and 10 points if initial signal magnitudes were unspecified. These results are encouraging, given that the initial values of actual data curves can be mathematically difficult to identify, or inconsistent between electrodes on an array. Thus, while some accuracy may be sacrificed by failure to specify the initial values, more robust algorithms are desirable.

The use of calculated initial magnitudes rather than specified also decreased average squared error by roughly 500 fold. However, it is unknown whether the time constants derived from specified or calculated end voltage values are more accurate. During the *in vivo* experiments, curves were rarely allowed to complete resolution for the sake of time, instead using a definition of technical resolution based on rate-of-change criteria. So it is possible that specification of initial magnitudes may have introduced more artifact than it prevented. Many questionable values were run both ways in the main experiment to verify the accuracy of the curve fit.

#### **B.3.2 Determining the Effect of Sampling Frequency on Curve Fitting**

Error due to sampling rates was observed to be lower for a large or very small number of samples per curve. Error was actually lower for 3-5 points per curve (Figure B.1), due to the greater ease of finding a tight fit, but time constant calculations at lower sampling rates were less stable, blowing up at less than 5 points. Excluding the lowest sampling value, the standard deviation of time constants calculated at different sampling rates was on average only  $6.04 \pm 6.45\%$ , and deviation between the three highest sampling groups was  $2.62 \pm 1.44\%$  as a percent of average. These results indicate that if efficiency

of calculations is desired for an implanted sensor, assuming a non-overlap of events, only a very few samples per curve, need be taken to calculate the time constant (Figure B.2).

## B.4 Conclusions

Curve fitting to real sensor response curves provide more in-depth insight into the needs and limitations of predictive algorithms. This study demonstrated that relatively few points are needed, preferably in the early portion of the curve, for the robust and consistent determination of time constants. Time constants may be a more computationally efficient method of making control and predictive decisions. These results are applicable to biosensors, but also to other applications requiring efficient characterization of exponential curves such as *in vivo* thermistors and drug delivery models.

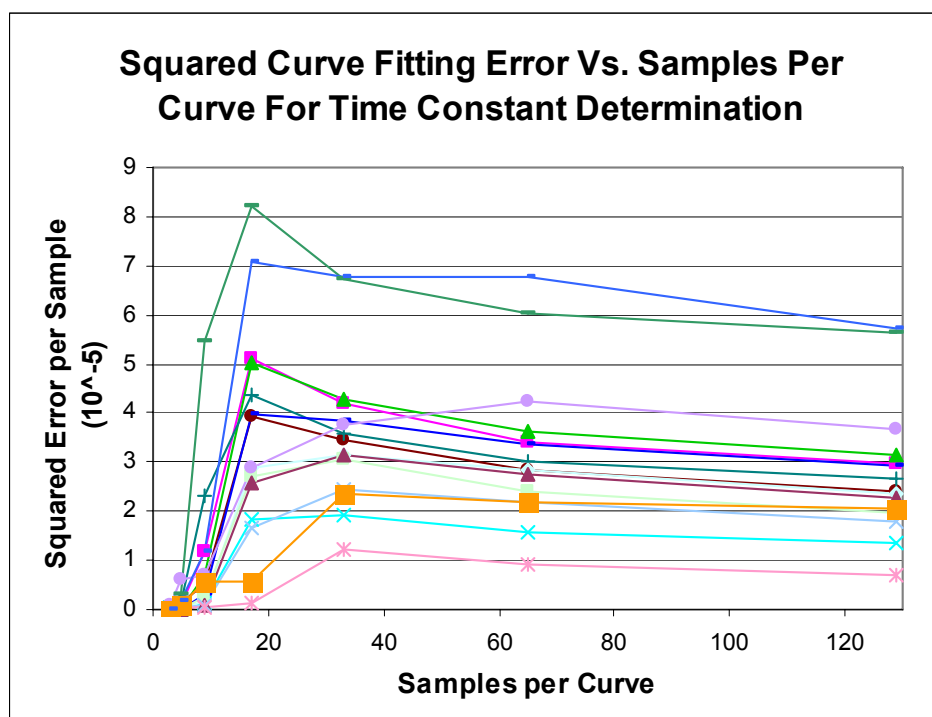


**Figure B.1** Curve Fitting Error and Sampling Frequency

Squared error for a nonlinear regression curve fit, normalized to the number of samples, is shown plotted against the sampling rate for 16 electrodes. Sensor calibration data was sampled at increasing frequency to determine the optimal sampling rate for algorithm design and practical diagnostic use. Error at low sampling rates was artificially low since the curve fitting was simplified by the need to encompass fewer points. Increasing sampling frequency after 32 samples appeared to begin a slow decrease in error, making 32 samples the sweet spot of efficiency.

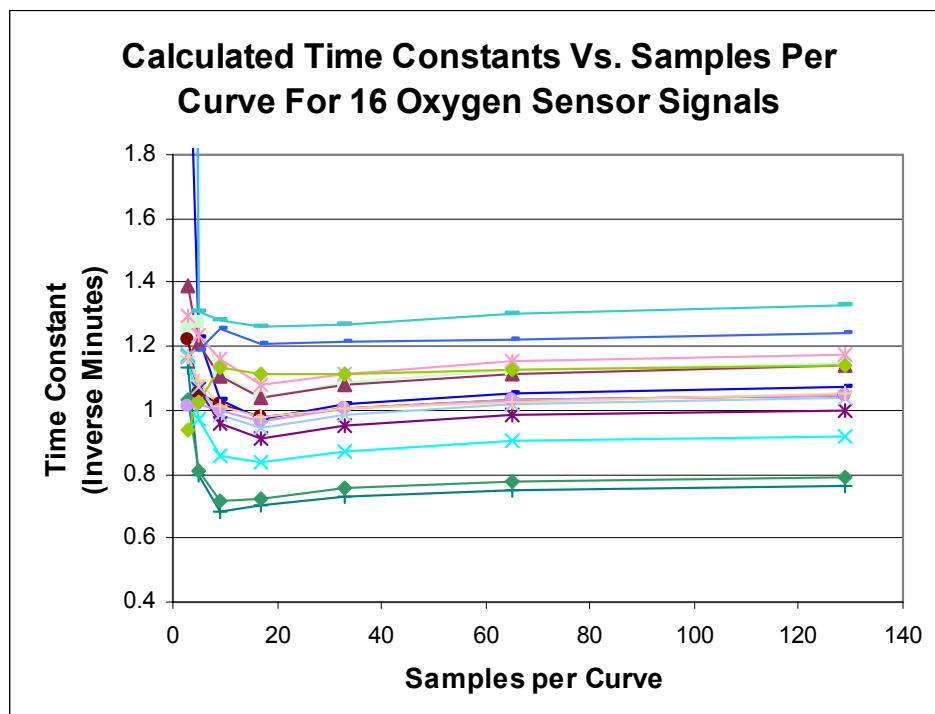


**Figure B.2** Time Constant Calculation and Sampling Frequency

The calculated time constants for 16 electrodes are shown plotted against sampling frequency. The time constants were found to be fairly consistent at higher sampling rates, while at lower sampling rates, variance increased and finally blew up for less than 5 samples per curve.

# **APPENDIX C: 2-Dimensional Oxygen Diffusion Model of the Subcutaneous Tissue Surrounding a Sensor Array**

## **C.1 Abstract**

The development of a model of oxygen diffusion in subcutaneous tissue cross sections is detailed in this Appendix. Digitized histology is used to create spatial maps of tissue features that produce or consume analytes, or that alter analyte diffusion. The spatial maps are modified for use in either a superimposition of steady state solutions or a mesh-based partial differential equation solution of the diffusion equation. The end result is a spatial map of oxygen in the tissue.

The model was designed modularly to allow multiple methods of solving the diffusion equation. Recent software advances may allow the model to implement dynamic boundary conditions that represent vascular flow, the activity of an implanted sensor, or heat gradients and changes in the tissue.

The model may potentially be used to validate observations of oxygen transfer differences seen in the tissue with implanted sensors or optical methods. Calibration of the model with empirical measurements from sensors and other tools could refine it to allow high throughput determination of how tissue interventions like biomaterial implantation may affect oxygen diffusion.

## **C.2 Introduction**

Existing oxygen diffusion models are largely based on the radial diffusion methods posited by Krogh<sup>(71)</sup> in his seminal work on muscle capillary physiology. Establishing a robust model of oxygen transfer in the vascular network and tissue has been a focal goal of many groups, using tools such as finite element and Greens Function methods<sup>(57, 101, 103, 119)</sup>. Aided by an improved understanding of the role of the microvasculature in oxygen transfer and delivery<sup>(63, 129, 130)</sup>, these models offer great value to oncology, cardiovascular research, and implant design. However, many of these models treat tissue as a homogenous mass, and do are not concerned with what happens to the oxygen once it has left the vasculature.

Modeling oxygen transfer is important to understanding how the tissue environment and changes to that environment affect the performance of biosensors. Models should be empirically based<sup>(57, 101, 103, 119)</sup>, drawing on real world spatial and diffusion properties of the tissue. Oxygen measurement tools<sup>(34)</sup> such as implantable sensors<sup>(21, 22)</sup> and optical methods such as phosphorylation quenching and decay<sup>(55, 64, 127)</sup> and hemoglobin saturation<sup>(99, 100)</sup>, can be used to calibrate the models, eventually allowing them to be useful in a predictive capacity.

In the model, digital images of the histology are used to create spatial maps of the vasculature and potentially consumptive elements (cells) (Chapter 6). Implanted sensor experiments and values mined from existing literature are used to estimate diffusion variables and vascular oxygen levels. The spatial maps are then combined and analyzed by steady state approximation of the diffusion equation, using field superimposition

similar in application to Green's Function methods<sup>(119)</sup>, or Partial Differential Equation (PDE) solving tools. The result will be a spatial map of oxygen concentration in the tissue, which can then be compared to measured readings, such as those from an oxygen sensor array, for calibration. While the early model is limited in capability, it is designed in a modular fashion, so that improved computational methods or updates to our understanding of oxygen diffusion in the tissue will be easily applicable.

An empirical oxygen model offers great value to research in both diffusion and biomaterials, establishing predicted diffusion properties of the tissue response to biomaterials as a quantitative measure of their compatibility.

## **C.3 Materials, Methods and Discussion**

### **C.3.1 Programming and Design**

A user interface (Figure C.1) was designed in Matlab (v6.5.1, Mathworks) to allow the import of and combination of spatial maps of the microvasculature and other tissue features, followed by the solution of the diffusion equation, ultimately resulting in a map of tissue oxygenation. The imported spatial maps are to be largely generated by the HistoQuant program from cross-sections of subcutaneous tissue, as described in Chapter 6. However, the program designed for this study also allows importation of non-quantified images, which the user then analyzes by hand.

Three types of spatial maps, each introducing different boundary conditions, will be discussed in this work. The first is maps of the vasculature: capillaries, venules, and arterioles. These maps will be used by the program to define sources of oxygen. The second type of spatial map is a map of consumptive elements in the tissue, such as cells, or an active sensor. In the current study, these maps are used to determine relative differences in consumption between different tissues based on the ratio of their cell density. The relative differences are used to adjust the steady state solution to the diffusion equation. However, programming currently underway will allow these maps to be imported into the model with intact spatial relationships, rather than lumped parameters. The last type of spatial map is one that defines regions of altered diffusion, such as retractor muscle with unsaturated myoglobin. Only the vascular maps will be described in detail in this work.

Once the spatial maps are combined and their respective boundary conditions are applied, the image undergoes one of two methods of solving for diffusion. The first is by superimposition of steady state solutions. In the second, partial differential equation (PDE) software is applied. The final result is a spatial map of oxygen concentration in the tissue. The latter approach, PDE solvers, can also be applied to dynamic states of the tissue, such as changes in vascular perfusion or oxygenation.

### **C.3.2 Diffusion Constants**

Default diffusion variables were obtained from the literature. Many studies found similar values for the diffusion constant ( $DO_2$ ), from  $1.15\text{-}2.59 \times 10^{-5} \text{ cm}^2/\text{s}$  in the rat mesentery<sup>(145)</sup> and several hamster muscle types<sup>(16, 39)</sup>. However, there was a wide variety in the reported consumption rates, potentially reflecting differences in the preparation and tissue types. Work by Tsai, which detailed the combination all three

diffusion variables, including  $\text{DO}_2$  and consumption rate  $m$ , as well as solubility  $\alpha$ , is utilized for this model's default values<sup>(129)</sup>. Tsai used phosphorylation decay techniques to determine radial oxygen profiles around several vessels *in vivo*. Profiles were fit to the steady state diffusion equation solution to find the diffusion variables. Figure C.1 shows the default values and units used.

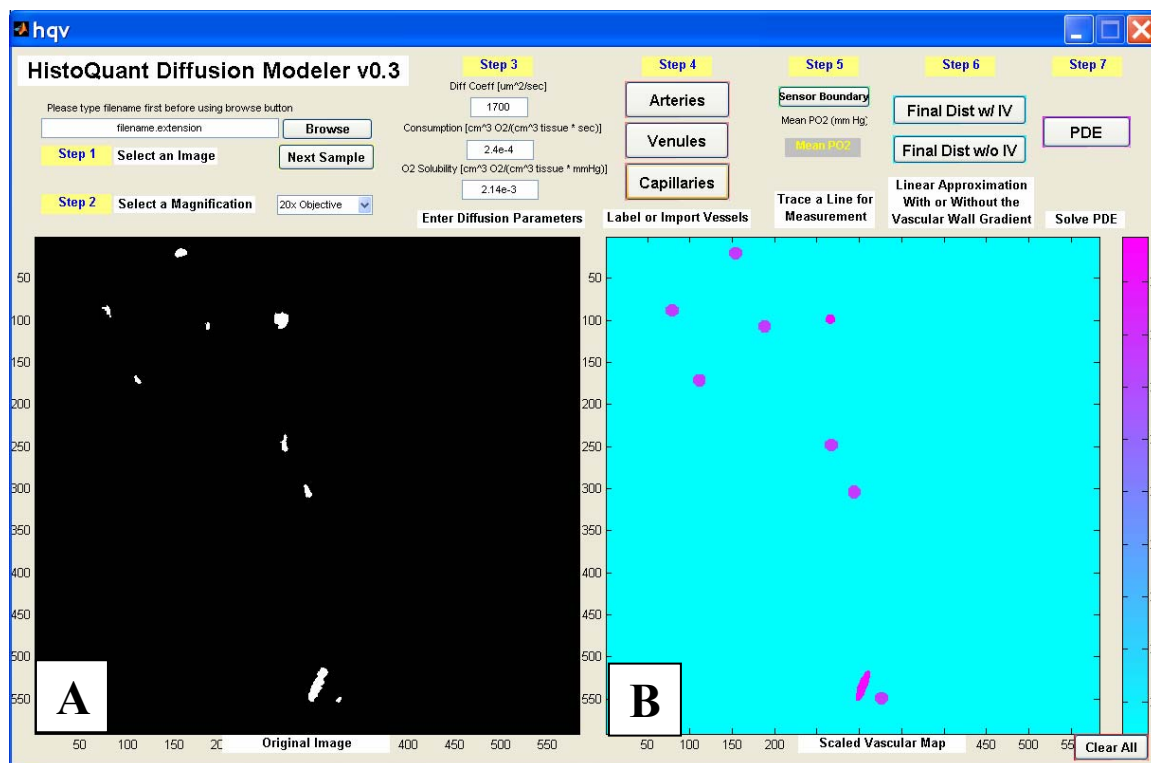


**Figure C.1** The Oxygen Diffusion Model User Interface: Spatial Vascular Map

The HistoQuant diffusion modeler is shown, with the original spatial map of vasculature generated by HistoQuant (A) for the Trichrome erythrocyte isolation shown in Figure 6.13. (B) shows the map after comparison to the vessel oxygenation curves. The color bar on the right shows vascular oxygenation (extravascular levels only) as  $\text{PO}_2$  in mmHg. The purple colored circles are capillaries, which are dilated for visibility, and the two pink colored objects are veins.

True pixel size is designated in Step 2 using calibrations with a slide micrometer (See Chapter 6 Methods), so that the solutions to the diffusion equation are spatially accurate. Diffusion constants are shown at their default values in Step 3 with appropriate units. These values can be altered by the user based on parameter estimation from cell density counts and analysis of sensor signal dynamics.

This dissertation also demonstrated in Chapter 4, that the oxygen diffusion constant in the tissue could potentially be calculated using the signal curves for implanted oxygen sensors. Future work will potentially employ this method to specialize the diffusion constant to each tissue sample. Likewise, it was discussed in Chapter 5, that

solubility of tissue may potentially be estimable using the loss of sensor signal magnitude following hypoxic exposure in proportion to exogenous oxygen changes.

### **C.3.3 Generating Spatial Vascular Maps**

The first step in generation of spatial maps in HistoQuant is simply the process of isolating tissue features and removing artifacts, as discussed in Chapter 6. Once a binary image is produced by HistoQuant, it must sometimes be processed for use in the diffusion model, as with dilating nuclei maps to represent cells (Figure 6.9).

#### **C.3.3.1 Vascular Maps from HistoQuant**

Identification of the vasculature for HistoQuant requires a suitable staining method. One approach is to label erythrocytes, but a more effective approach is immunohistochemical staining of vascular endothelial cells. Such labels are easily color segmented and allow simpler determination of the vascular type.

Each microvessel type should have its own spatial map for the model. Different vessel types are differently oxygenated, and separating their maps simplifies estimation of vascular oxygenation. In the separate maps, pixel clusters are measured for their minor axis, the assumed diameter of the vessel. This causes some error with veins, but is highly effective for both capillaries and arterioles. The diameter is compared to empirical vascular oxygenation curves to determine its projected oxygen content. It is this later value that will be used to define the radial diffusion profile emanating from each vessel.

#### **C.3.3.2 User Generated Maps**

When vascular maps are not available from HistoQuant, but the user can identify microvessels in the sample image by eye, vascular maps can be user generated. A mouse cursor is used to select the center of capillaries, which are treated as circles. Venules and arterioles are treated as ellipses, and the cursor is used to define the major and minor axes of each. Separate maps are generated of each vessel type. The minor axis of each vessel is then compared to empirical vascular oxygenation curves.

### **C.3.4 Vascular Oxygenation Curves**

Curves of microvessel oxygen content were constructed from the literature. Studies by Kerger and Torres Filho utilized optical methods to measure microvascular oxygen levels in the hamster window chamber<sup>(66, 128)</sup>. The results for the oxygen content of each vessel type as a function of outer diameter were plotted and curve fitted in Excel (v2003, Microsoft). The curve form for arterioles proved to be a diminishing exponential curve, while that for venules was more s-shaped, curving up from post-capillary values, then changing inflection to a diminishing exponential with larger values. Capillary diameter was assumed to vary little, and so oxygen content was averaged. All measurements of vascular oxygenation had high variation, but future application of a stochastic model or a refined understanding of oxygenation in vascular networks could be applied without disrupting the model.

Mathematically, the spatial maps of the vasculature are modified to account for their vascular content by multiplying the perimeter of each vessel by its extravascular (just outside the vessel walls) oxygen concentration calculated from the oxygenation curves. The lumen of each vessel is multiplied by its intravascular oxygen content. The

previously binary maps become maps of oxygen values inside vessels. The right hand side of Figure C.1 demonstrates a very simple example of such a map.

### C.3.5 Minimum Oxygen Values and Diffusion through the Skin

Research has suggested that most tissues do not have regions of zero oxygenation, even during hypoxia<sup>(144, 145)</sup>. It has also been previously observed by Stucker that subcutaneous tissue 0.25-0.40mm beneath the surface may be highly dependent on diffusion of exogenous oxygen through the skin surface, which would present a constant oxygen supply.<sup>(124)</sup> Thus, the model was designed to allow designation of a minimum non-zero oxygen level.

### C.3.6 The Wall Gradient

There is a great deal of debate regarding the disparity between intravascular and extravascular oxygen content. An excellent discussion of this debate has been made by Tsai et al<sup>(130)</sup>. In brief, there are two camps, which respectively contend that the either the cells of the vascular wall are responsible for significant consumption of oxygen, thus causing the large drop in oxygenation from inside to outside the vessel known as the wall gradient, or that other consumptive sources or systematic measurement errors are responsible. In the past, the wall gradient had been regarded as an indication that larger blood vessels were differentially permeable to oxygen, though this is no longer a widely held belief. Regardless of the cause of the wall gradient, its presence is accounted for in the model and may become of some importance when dynamics are applied to the model in the future. Figure C.2 shows the impact of the wall gradient.

### C.3.7 Solving the Diffusion Equation

Spatial oxygen maps depend on the solution of the diffusion equation. The most common form of the equation is differential.

$$\text{Equation C.1} \quad \frac{\partial PO_2}{\partial t} = DO_2 \times \frac{\partial^2 \alpha PO_2}{\partial x^2} - m$$

$PO_2$  is the pressure of oxygen in the tissue, while  $DO_2$  is the diffusion constant for oxygen in tissue. The variables  $\alpha$  and  $m$  respectively represent solubility of oxygen in the tissue and consumption of oxygen by the tissue (units of  $\alpha = (\text{Vol } O_2)/(\text{Vol tissue} * \text{Pressure})$  (Units of  $m = ((\text{Vol } O_2)/(\text{Vol tissue} * \text{time}))$  (Units of  $DO_2 = \text{flux, or (area/time)}$ ). The equation can be solved for the steady state, where the time dependent term is equal to zero, as in Equation C.2. Consumption is assumed to be constant, and it is assumed that there are no oxygen gradients perpendicular to the tissue slice.

$$\text{Equation C.2} \quad m = DO_2 \times \frac{\partial^2 \alpha PO_2}{\partial x^2}$$

If time dependent components exist, a numerical approximation must be made for the transient state using equation solver software. With the user of a PDE solver, dynamic boundary conditions can even be applied, such as pulsatile vascular flow or intermittent function of an implanted sensor.

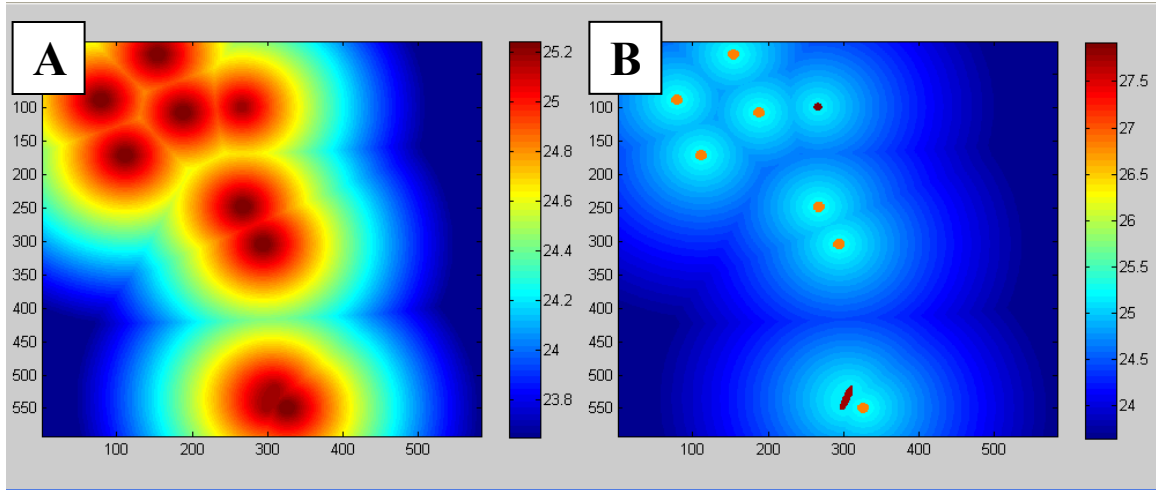


**Figure C.2** 2-Dimensional Tissue Oxygen Maps

(A) shows a pseudo-color map of oxygenation in the vascular map from Figure C.1. Values are  $PO_2$  in mmHg as per the color bar. The radial distribution of oxygen is clearly visible. (B) shows the same map with the intravascular oxygenation included. This is reflected in the greater range of the colorbar and demonstrates the significant wall gradient in even small microvessels.

### C.3.7.1 Diffusion Equation Solution Approach 1: Superimposition

The superimposition approach to spatial mapping of oxygen in the tissue uses individually calculated “masks” for of the radial oxygen profile for each vessel, which are superimposed. It is computationally very inexpensive in two dimensions and does not require the complexity of assigning boundary conditions to the tissue perimeter. It allows the solution of much larger models that would exhaust computational capacity using PDE solvers.

The superimposition approach assumes steady state conditions and thus parabolic radial oxygen gradients. The value of oxygen,  $PO_2$ , decreases as the distance from the vessel ‘x’ increases, following the parabolic form of Equation C.3, which is the solution of Equation C.2 for  $PO_2$ .

$$\text{Equation C.3} \quad PO_2 = \frac{m}{2\alpha DO_2} * x^2 - \sqrt{\frac{2mPO_{2o}}{\alpha DO_2}}x + PO_{2o}, \quad 0 \geq x \leq \delta$$

At the vessel wall,  $x = 0$ . The range of the equation is for  $x$  from 0 to  $\delta$ , where  $\delta$  is the theoretical oxygen penetration distance of the vessel (Equation C.4), with units of distance.  $PO_{2o}$  is the oxygen pressure at the vessel wall, assumed to be constant with constant flux from the vessel wall.

$$\text{Equation C.4} \quad \delta = \sqrt{\frac{2\alpha DO_2 PO_{2o}}{m}}$$

To apply the superimposition approach, each vessel in the spatial map is given its own digital mask the size of its penetration capability, a matrix with dimensions of  $2\delta$

plus the vessel diameter on each side, with all pixels valued at unity. The distance of each pixel in the mask from the vessel wall is calculated, and using Equation C.3 and the empirical oxygen constants already discussed, the oxygen value of each pixel is solved for and replaces the pixel value. It is not supposed that measurements will be taken between the vessels and thus error from this approach is not expected to be large under stable conditions.

### **C.3.7.2 Ellipse Estimation in the Superimposition Approach**

For circular vessels, radial symmetry is assumed. However, for elliptical vessels, the distance 'x' which is plugged into Equations C.3 and C.5, is actually the average distance from the two foci with the distance from the foci to the vessel wall subtracted. This method was shown produce almost negligible error (<1%) compared to PDE solutions of a single ellipse, estimated by the average percent difference between each pixel's oxygen value in the vessel masks. More eccentric ellipses had higher error, but error dropped off rapidly as x increased.

Figure C.2A shows the 2-Dimensional results of superimposition of the steady state solution of radial diffusion for several venules and capillaries, without intravascular values. A venule with high eccentricity was chosen to illustrate the ellipse estimation.

### **C.3.7.3 Diffusion Equation Solution Approach 2: PDE Solvers**

As has been stated, this model was designed to be highly modular, allowing improvements in computation to be incorporated. One such improvement is the application of increasingly powerful PDE solver software. This project employed Matlab's PDE Tool (v2006a, Mathworks) as a second approach to solving the diffusion equation of small models. Application of the vascular spatial maps to the PDE solver simply requires that the shape and oxygen content of each vessel be conveyed. First, a rectangular model size of the tissue sample is established in the solver with an empirically determined minimum value and semi-infinite boundary conditions<sup>(119)</sup>. Then, each vessel's center, its major and minor axes, and the orientation of the major axis, determined by HistoQuant, are used to draw the vessel geometries into the solver. The vessels are given boundary conditions of fixed concentrations based on those calculated from oxygenation curves. The program then establishes a triangular mesh using the methods of George<sup>(46)</sup>, which can be refined for greater accuracy and resolution, but at a higher computational cost. The mesh is then solved for a parabolic equation with diffusion constants provided to the solver by the modeling program, ultimately producing a spatial map of oxygen levels in the tissue.

Future implementation of Comsol Multiphysics (Comsol, formerly Femlab) will allow the use of dynamic boundary conditions and the application of heat gradients, which are a significant consideration for subcutaneous implants<sup>(15, 16)</sup>.

Figure C.3 shows the same vascular map as Figure C.1B, after transfer to Matlab's PDE Tool (v2006a, Mathworks), a PDE solver program. This program was found to communicate effectively with Matlab, but had some problems with specific capillary geometries, and single capillaries were often moved or left out of the mesh creation. These problems were not seen in preliminary tests with Comsol (v3.2a Comsol), a more advanced PDE solver program.

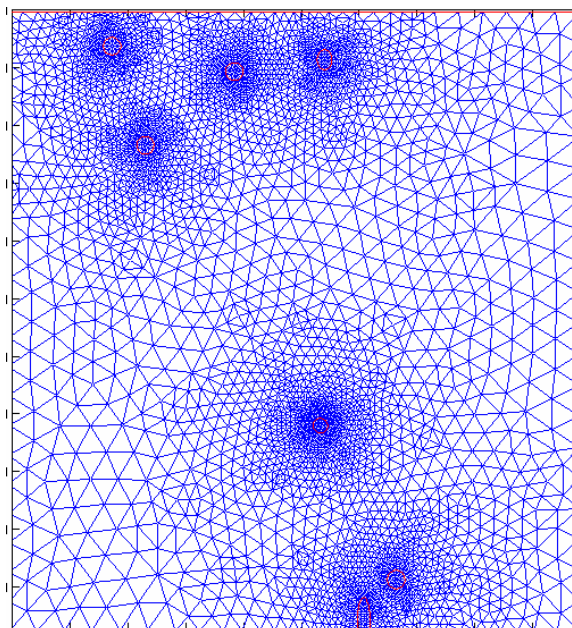


**Figure C.3** Mesh Solution for a Spatial Vascular Map

The vascular map from Figures C.1 and C.2 is shown in the Matlab PDE solver. A triangular mesh grid has been established for solution of the equation. The grid shown is at the second level of refinement, offering greater resolution at higher computational cost. Several capillaries were slightly displaced by the solver, a common error in the communication between the model program and Matlab's PDE solver.

### **C.3.8 Oxygen Measurements at the Sensor Boundary**

Once the final spatial map of oxygen has been produced, oxygen levels can be measured by querying the map pixel by pixel. Alternately, a line can be traced on the image, and a profile of oxygen values along that line can be created (Figure C.4). This is beneficial to sensor studies where an oxygen profile at the sensor membrane is desirable.

### **C.3.9 Consumptive and Altered-Diffusion Maps: Potential Application of the Model to Other Analytes**

Spatial maps of consumptive elements like cells are not easily applied to the superimposition approach. In superimposition, consumption maps are used to estimate the average consumption rate of the tissue and alter the steady state solution accordingly. However, using PDE solvers, these maps can be applied to the model in the same fashion as the vascular maps. In the PDE solver, the consumptive elements are drawn as ellipses with a boundary condition of fixed consumption. An understanding of individual cell consumption is necessary for this approach, as most calculations of tissue consumption are calculated by tissue volume.

In the same manner, maps of features which alter diffusion cannot be applied by superimposition. However, importation of these spatial maps into PDE solvers is simply a matter of transferring their geometries to the PDE tool, and assigning different  $\text{DO}_2$  values within the geometries. Models utilizing these maps would be useful in applications with layered or mixed tissue environments or in situations where impermeable objects such as implanted materials may be affecting diffusion through the

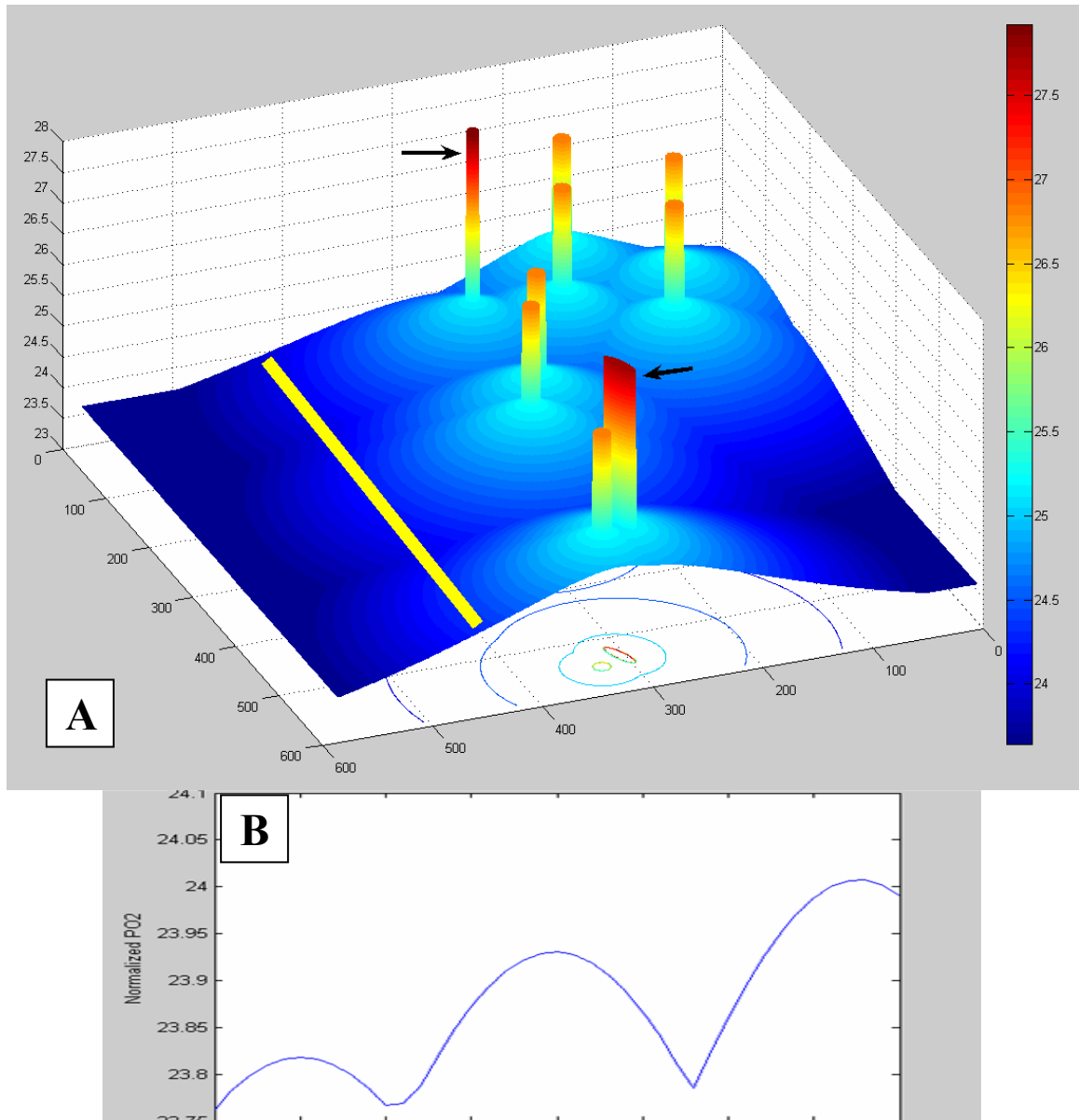


**Figure C.4** Topographical Tissue Oxygenation Map: Profile of Oxygen at the Sensor

(A) shows a contour map of tissue oxygenation for the vascular map of Figure C.1, with oxygen as PO<sub>2</sub> in mmHg per the colorbar at the right. The Y-axis has been flipped due to Matlab internal programming (Matlab utilizes reversed axes, so Y is left-right and X is up-down). The two black arrows designate veins, while the remaining columns are capillaries. The columns are a result of including intravascular values and the wall gradient in the model, while the cone shapes at their bases are the actual extravascular radial oxygen profiles for the vessels. The outlines of vessel boundary conditions, appearing as rings, are visible on the XY plane in the background.

The yellow band indicates the projected location of the sensor, along which an oxygen profile is taken. The profile is displayed in (B) as a function of oxygen tension PO<sub>2</sub>.

tissue. In particular, application of the model to new analytes such as glucose would require that the selective permeability of cell membranes be accounted for. Previous models of glucose diffusion in the tissue have discussed this issue<sup>(41)</sup>.

### **C.3.10 Observations of the Model**

The superposition approach was used to model several interesting phenomena. The first was the dominant role of arterioles in tissue oxygenation at a resting state. In a field with several capillaries, the addition of even a small arteriole -8 to 10 $\mu$ m in diameter- overpowered the contribution of any capillaries or veins within a hundred microns. This agreed with previous observations<sup>(38, 59, 102, 126, 130)</sup>. This observation was predictable from the large extra-vascular oxygen pressures of arterioles.

Secondly, with respect to capillaries, proximity was observed to be key. A row of 20 capillaries modeled in the retractor muscle 100 microns or more from the sensor contributed less to the sensor oxygen content than a single capillary modeled 50 microns distant from the sensor, at default values for the diffusion variables. When consumption rates were lowered, the penetration of capillary oxygenation increased, and this relationship softened. The opposite was seen for increases in solubility.

### **C.3.11 Requirements and Limitations of the Model**

This study was limited by problems in the histological processing of tissue from sensor implantations. Thus, empirical models could not be created for these specific tissues. The future goal is to model the tissue surrounding a sensor and compare actual sensor readings to the predicted tissue oxygenation at the sensor location. In order to accomplish this, better histology will be needed. Additionally, tightly sequential sections will be needed so that different stains for vasculature, cell nuclei etc. can be applied to very similar cross-sections, allowing combination in the model. Lastly, better methods of spatial relationships between the sensor array electrodes and the tissue are desirable, so that rather than an average, the oxygenation for individual sensors can be predicted and calibrated to the sensor signals.

Computationally, the limits of the program were mostly errors in transferring the spatial map geometries into the PDE solvers. There were many problems with the PDE solvers rejecting certain configurations which may be lessened by more advanced solvers. The superimposition approach worked well when static conditions were assumed, but requires lumping of parameters for consumption and solubility, which limits the potential usefulness of the model and prevent application of the model to glucose or other analytes.

Finally, regarding our understanding of tissue oxygen diffusion, the effect of individual tissue features is still poorly defined. Features like collagen are likely to affect diffusion at higher concentrations, but the relationship between collagen density and solubility or diffusion rates in the tissue are unclear. Additionally, the oxygen consumption behavior of cells is not well understood, especially with respect to wound healing and oxygen dynamics.

Fortunately, the modular design of the model will allow implementation of solutions for these concerns as they become available.

### **C.3.12 Future Computing Directions**

Implementation of advanced PDE solvers is the first stage in improving the capabilities of the model. Increased computational capacity may also allow the preparation of 3-Dimensional models from confocal z-stacks<sup>(18, 98)</sup> or by stacking regularly spaced sections from the tissue<sup>(56)</sup>. Finally, multiphysics solvers like Comsol (Comsol), would allow the implementation of chemical or heat gradients that affect diffusion, the latter of which has a significant effect on  $\text{DO}_2$  in subcutaneous tissue<sup>(15, 16)</sup>.

To either the PDE solvers or the superimposition approach, stochastic determination of vascular oxygenation would improve the randomness of larger samples.

## **APPENDIX D:     Matlab and Mathematica Code for the Dissertation**

The working HistoQuant histological quantification program and Mathematica time constant estimation code can be downloaded from [http://be-web.ucsd.edu/faculty/area/biosens/public\\_html/programming.htm](http://be-web.ucsd.edu/faculty/area/biosens/public_html/programming.htm) or can be requested by contacting the dissertation author [jbg4e@alumni.virginia.edu](mailto:jbg4e@alumni.virginia.edu).

Mathematica code was co-authored by the dissertation author and Lucas Kumosa (UCSD Bioengineering, Ph.D. Student).

Matlab code for the HistoQuant histological quantification program was written by the dissertation author.

Matlab code for the diffusion model was co-authored by the dissertation author and Alex Hsiao (UCSD Bioengineering, Ph.D. Student).

## REFERENCES

1. **Albert MA, Danielson E, Rifai N, and Ridker PM.** Effect of statin therapy on C-reactive protein levels: the pravastatin inflammation/CRP evaluation (PRINCE): a randomized trial and cohort study. *Jama* 286: 64-70, 2001.
2. **Albert MA, Glynn RJ, and Ridker PM.** Plasma concentration of C-reactive protein and the calculated Framingham Coronary Heart Disease Risk Score. *Circulation* 108: 161-165, 2003.
3. **Algire G.** An adaptation of the transparent-chamber technique to the mouse. *Journal of the National Cancer Institute* 4: 1-11, 1943.
4. **Algire GH.** Summary of studies of transplantation of homologous tissues. *Fed Proc* 16: 601-602, 1957.
5. **Algire GH and Legallais FY.** Recent developments in the transparent-chamber technique as adapted to the mouse. *J Natl Cancer Inst* 10: 225-253, incl 228 pl, 1949.
6. **Anderson JM.** Inflammation, Wound Healing, and the Foreign Body Response. In: *Biomaterials Science*, edited by Ratner BD: Academic Press, 1996, p. 165-173.
7. **Anderson JM.** Multinucleated giant cells. *Curr Opin Hematol* 7: 40-47, 2000.
8. **Anderson JM, Niven H, Pelagalli J, Olanoff LS, and Jones RD.** The role of the fibrous capsule in the function of implanted drug-polymer sustained release systems. *J Biomed Mater Res* 15: 889-902, 1981.
9. **Armour JC, Lucisano JY, McKean BD, and Gough DA.** Application of chronic intravascular blood glucose sensor in dogs. *Diabetes* 39: 1519-1526, 1990.
10. **Ausprunk DH and Folkman J.** Migration and proliferation of endothelial cells in preformed and newly formed blood vessels during tumor angiogenesis. *Microvasc Res* 14: 53-65, 1977.

11. **Baker DA and Gough DA.** A Continuous, Implantable Lactate Sensor. *Anal Chem* 67: 1536-1540, 1995.
12. **Bates DM and Watts DG.** *Nonlinear regression analysis and its applications.* New York: Wiley, 1988.
13. **Behling CA and Spector M.** Quantitative characterization of cells at the interface of long-term implants of selected polymers. *J Biomed Mater Res* 20: 653-666, 1986.
14. **Belanger MC and Marois Y.** Hemocompatibility, biocompatibility, inflammatory and in vivo studies of primary reference materials low-density polyethylene and polydimethylsiloxane: a review. *J Biomed Mater Res* 58: 467-477, 2001.
15. **Bentley TB, Meng H, and Pittman RN.** Temperature dependence of oxygen diffusion and consumption in mammalian striated muscle. *Am J Physiol* 264: H1825-1830, 1993.
16. **Bentley TB and Pittman RN.** Influence of temperature on oxygen diffusion in hamster retractor muscle. *Am J Physiol* 272: H1106-1112, 1997.
17. **Blanco E, Qian F, Weinberg B, Stowe N, Anderson JM, and Gao J.** Effect of fibrous capsule formation on doxorubicin distribution in radiofrequency ablated rat livers. *J Biomed Mater Res A* 69: 398-406, 2004.
18. **Botvinick EL.** *A Confocal Microscope for Nondestructive Quantification of Microvascular Flow.* San Diego: UC San Diego, 2001.
19. **Brauker JH, Carr-Brendel VE, Martinson LA, Crudele J, Johnston WD, and Johnson RC.** Neovascularization of synthetic membranes directed by membrane microarchitecture. *Journal of Biomedical Materials Research* 29: 1517-1524, 1995.
20. **Brem H, Kader A, Epstein JI, Tamargo RJ, Domb A, Langer R, and Leong KW.** Biocompatibility of a biodegradable controlled-release polymer in the rabbit brain. *Selective Cancer Therapeutics* 5: 55-66, 1989.
21. **Buerk DG, Tsai AG, Intaglietta M, and Johnson PC.** Comparing tissue PO<sub>2</sub> measurements by recessed microelectrode and phosphorescence quenching. *Adv Exp Med Biol* 454: 367-374, 1998.

22. **Buerk DG, Tsai AG, Intaglietta M, and Johnson PC.** In vivo tissue pO<sub>2</sub> measurements in hamster skinfold by recessed pO<sub>2</sub> microelectrodes and phosphorescence quenching are in agreement. *Microcirculation* 5: 219-225, 1998.
23. **Burstone MS.** Histochemical demonstration of phosphatases in frozen sections with naphthol AS-phosphates. *J Histochem Cytochem* 9: 146-153, 1961.
24. **Clark ER K-SH, Rex RO, Williams RG.** Recent modifications in the method of studying living cells and tissues in transparent chambers inserted in the rabbit's ear. *Anat Rec* 47, 1930.
25. **Colantuoni A, Bertuglia S, and Intaglietta M.** Quantitation of rhythmic diameter changes in arterial microcirculation. *Am J Physiol* 246: H508-517, 1984.
26. **Colton CK.** Engineering challenges in cell-encapsulation technology. *Trends Biotechnol* 14: 158-162, 1996.
27. **Connolly KM, Stecher VJ, and Kent L.** Examination of interleukin-1 activity, the acute phase response, and leukocyte subpopulations in rats with adjuvant-induced arthritis. *J Lab Clin Med* 111: 341-347, 1988.
28. **Cox ME.** Oxygen Diffusion in Poly(dimethyl Siloxane) using Fluorescence Quenching. I. Measurement Technique and Analysis. *Journal of Polymer Science: Part A Polymer Chemistry* 24: 621-636, 1986.
29. **Cramer T, Yamanishi Y, Clausen BE, Forster I, Pawlinski R, Mackman N, Haase VH, Jaenisch R, Corr M, Nizet V, Firestein GS, Gerber HP, Ferrara N, and Johnson RS.** HIF-1 $\alpha$  is essential for myeloid cell-mediated inflammation. *Cell* 112: 645-657, 2003.
30. **Curtis A and Wilkinson C.** Topographical control of cells. *Biomaterials* 18: 1573-1583, 1997.
31. **den Braber ET, de Ruijter JE, and Jansen JA.** The effect of a subcutaneous silicone rubber implant with shallow surface microgrooves on the surrounding tissues in rabbits. *J Biomed Mater Res* 37: 539-547, 1997.
32. **Detmar M, Brown LF, Schon MP, Elicker BM, Velasco P, Richard L, Fukumura D, Monsky W, Claffey KP, and Jain RK.** Increased microvascular density

and enhanced leukocyte rolling and adhesion in the skin of VEGF transgenic mice. *J Invest Dermatol* 111: 1-6, 1998.

33. **Deutsch J, Motlagh D, Russell B, and Desai TA.** Fabrication of microtextured membranes for cardiac myocyte attachment and orientation. *J Biomed Mater Res* 53: 267-275, 2000.
34. **Dewhirst MW, Klitzman B, Braun RD, Brizel DM, Haroon ZA, and Secomb TW.** Review of methods used to study oxygen transport at the microcirculatory level. *Int J Cancer* 90: 237-255, 2000.
35. **Dixon JS, Bird HA, Sitton NG, Pickup ME, and Wright V.** C-reactive protein in the serial assessment of disease activity in rheumatoid arthritis. *Scand J Rheumatol* 13: 39-44, 1984.
36. **Ebert RH FH, Pullinger BD.** A modification of a Sandison-Clark chamber for observations of transparent tissue in the rabbit's ear. *J Path & Bact* 48: 79-94, 1939.
37. **Edwards CH and Penney DE.** *Differential equations : computing and modeling.* Upper Saddle River, NJ: Prentice Hall, 2000.
38. **Ellsworth ML and Pittman RN.** Arterioles supply oxygen to capillaries by diffusion as well as by convection. *Am J Physiol* 258: H1240-1243, 1990.
39. **Ellsworth ML and Pittman RN.** Heterogeneity of oxygen diffusion through hamster striated muscles. *Am J Physiol* 246: H161-167, 1984.
40. **Endrich B, Asaishi K, Gotz A, and Messmer K.** Technical report--a new chamber technique for microvascular studies in unanesthetized hamsters. *Res Exp Med (Berl)* 177: 125-134, 1980.
41. **Ertefai S.** *Glucose and oxygen sensors implanted in the subcutaneous tissue : experimental and theoretical studies* (Thesis Ph D --University of California San Diego Department of Applied Mechanics Engineering Sciences 1989), 1989.
42. **Folsom AR, Pankow JS, Tracy RP, Arnett DK, Peacock JM, Hong Y, Djousse L, and Eckfeldt JH.** Association of C-reactive protein with markers of prevalent atherosclerotic disease. *American Journal of Cardiology* 88: 112-117, 2001.

43. **Freinkel RK and Woodley D.** *The biology of the skin*. New York: Parthenon Pub. Group, 2001.
  
44. **Garcia JH and Kamijyo Y.** Cerebral infarction. Evolution of histopathological changes after occlusion of a middle cerebral artery in primates. *J Neuropathol Exp Neurol* 33: 408-421, 1974.
  
45. **Geller RL, Loudovaris T, Neuenfeldt S, Johnson RC, and Brauker JH.** Use of an immunoisolation device for cell transplantation and tumor immunotherapy. *Ann N Y Acad Sci* 831: 438-451, 1997.
  
46. **George PL.** *Automatic mesh generation : application to finite element methods*. Chichester ; New York  
Paris: J. Wiley ;  
Masson, 1991.
  
47. **Giffen PS, Turton J, Andrews CM, Barrett P, Clarke CJ, Fung KW, Munday MR, Roman IF, Smyth R, Walshe K, and York MJ.** Markers of experimental acute inflammation in the Wistar Han rat with particular reference to haptoglobin and C-reactive protein. *Arch Toxicol* 77: 392-402, 2003.
  
48. **Glantz SA.** *Primer of biostatistics*. New York: McGraw-Hill, Medical Pub. Div., 2002.
  
49. **Goluch ED, Nam JM, Georganopoulou DG, Chiesl TN, Shaikh KA, Ryu KS, Barron AE, Mirkin CA, and Liu C.** A bio-barcode assay for on-chip attomolar-sensitivity protein detection. *Lab Chip* 6: 1293-1299, 2006.
  
50. **Gough DA, Leyboldt JK, and Armour JC.** Progress toward a potentially implantable, enzyme-based glucose sensor. *Diabetes Care* 5: 190-198, 1982.
  
51. **Grim M and Carlson BM.** Alkaline phosphatase and dipeptidylpeptidase IV staining of tissue components of skeletal muscle: a comparative study. *J Histochem Cytochem* 38: 1907-1912, 1990.
  
52. **Groebe K.** A versatile model of steady state O<sub>2</sub> supply to tissue. Application to skeletal muscle. *Biophys J* 57: 485-498, 1990.

53. **Hangai-Hoger N, Tsai AG, Friesenecker B, Cabrales P, and Intaglietta M.** Microvascular oxygen delivery and consumption following treatment with verapamil. *Am J Physiol Heart Circ Physiol* 288: H1515-1520, 2005.
54. **Haralick RM and Shapiro LG.** *Computer and robot vision*. Reading, Mass.: Addison-Wesley Pub. Co., 1992.
55. **Helmlinger G, Yuan F, Dellian M, and Jain RK.** Interstitial pH and pO<sub>2</sub> gradients in solid tumors in vivo: high-resolution measurements reveal a lack of correlation. *Nat Med* 3: 177-182, 1997.
56. **Hoofd L.** Calculation of oxygen pressures in tissue with anisotropic capillary orientation. II. Coupling of two-dimensional planes. *Math Biosci* 129: 25-39, 1995.
57. **Hsu R and Secomb TW.** A Green's function method for analysis of oxygen delivery to tissue by microvascular networks. *Math Biosci* 96: 61-78, 1989.
58. **Iizuka T and Lindqvist C.** Changes in C-reactive protein associated with surgical treatment of mandibular fractures. *J Oral Maxillofac Surg* 49: 464-467, 1991.
59. **Intaglietta M, Johnson PC, and Winslow RM.** Microvascular and tissue oxygen distribution. *Cardiovasc Res* 32: 632-643, 1996.
60. **Intaglietta M, Silverman NR, and Tompkins WR.** Capillary flow velocity measurements in vivo and in situ by television methods. *Microvasc Res* 10: 165-179, 1975.
61. **Jacob JT, Gebhardt BM, and Lewando J.** Synthetic scleral reinforcement materials. II. Collagen types in the fibrous capsule. *J Biomed Mater Res* 32: 181-186, 1996.
62. **Jacobs TL and Segal SS.** Attenuation of vasodilatation with skeletal muscle fatigue in hamster retractor. *Journal of Physiology (Cambridge)* 524: 929-941, 2000.
63. **Johnson PC, Vandegriff K, Tsai AG, and Intaglietta M.** Effect of acute hypoxia on microcirculatory and tissue oxygen levels in rat cremaster muscle. *J Appl Physiol* 98: 1177-1184, 2005.

64. **Kerger H, Groth G, Kalenka A, Vajkoczy P, Tsai AG, and Intaglietta M.** pO<sub>2</sub> measurements by phosphorescence quenching: characteristics and applications of an automated system. *Microvasc Res* 65: 32-38, 2003.
65. **Kerger H, Saltzman DJ, Menger MD, Messmer K, and Intaglietta M.** Systemic and subcutaneous microvascular Po<sub>2</sub> dissociation during 4-h hemorrhagic shock in conscious hamsters. *Am J Physiol* 270: H827-836, 1996.
66. **Kerger H, Torres Filho IP, Rivas M, Winslow RM, and Intaglietta M.** Systemic and subcutaneous microvascular oxygen tension in conscious Syrian golden hamsters. *Am J Physiol* 268: H802-810, 1995.
67. **Kidd KR, Dal Ponte DB, Kellar RS, and Williams SK.** A comparative evaluation of the tissue responses associated with polymeric implants in the rat and mouse. *Journal of Biomedical Materials Research* 59: 682-689, 2002.
68. **Kidd KR, Nagle RB, and Williams SK.** Angiogenesis and neovascularization associated with extracellular matrix-modified porous implants. *Journal of Biomedical Materials Research* 59: 366-377, 2002.
69. **Kindmark CO.** The concentration of c reactive protein in sera from healthy individuals. *Scandinavian Journal of Clinical & Laboratory Investigation* 29: 407-411, 1972.
70. **Koenig W, Sund M, Frohlich M, Fischer HG, Lowel H, Doring A, Hutchinson WL, and Pepys MB.** C-Reactive protein, a sensitive marker of inflammation, predicts future risk of coronary heart disease in initially healthy middle-aged men: results from the MONICA (Monitoring Trends and Determinants in Cardiovascular Disease) Augsburg Cohort Study, 1984 to 1992. *Circulation* 99: 237-242, 1999.
71. **Krogh A.** The number and distribution of capillaries in muscles with calculations of the oxygen pressure head necessary for supplying the tissue. *J Physiol* 52: 409-415, 1919.
72. **Kumosa L AD, Benedikt B, Kumosa M.** An Investigation of Moisture and Leakage Currents in GRP Composite Hollow Cylinders. *IEEE Transactions on Dielectrics and Electrical Insulation* 12: 1043-1059, 2005.

73. **Kushner I.** C-reactive protein in rheumatology. *Arthritis Rheum* 34: 1065-1068, 1991.
74. **Kushner I and Rzewnicki DL.** The acute phase response: General aspects. *Bailliere's Clinical Rheumatology* 8: 513-530, 1994.
75. **Kushner I, Volanakis JE, Gewurz H, and New York Academy of Sciences.** *C-reactive protein and the plasma protein response to tissue injury*. New York, N.Y.: New York Academy of Sciences, 1982.
76. **Langer R, Brem H, and Tapper D.** Bio compatibility of polymeric delivery systems for macro molecules. *Journal of Biomedical Materials Research* 15: 267-278, 1981.
77. **Larcher F, Murillas R, Bolontrade M, Conti CJ, and Jorcano JL.** VEGF/VPF overexpression in skin of transgenic mice induces angiogenesis, vascular hyperpermeability and accelerated tumor development. *Oncogene* 17: 303-311, 1998.
78. **Li J, Zhang YP, and Kirsner RS.** Angiogenesis in wound repair: angiogenic growth factors and the extracellular matrix. *Microsc Res Tech* 60: 107-114, 2003.
79. **Lo A, Fuglevand AJ, and Secomb TW.** Oxygen delivery to skeletal muscle fibers: effects of microvascular unit structure and control mechanisms. *Am J Physiol Heart Circ Physiol* 285: H955-963, 2003.
80. **Loudovaris T, Jacobs S, Young S, Maryanov D, Brauker J, and Johnson RC.** Correction of diabetic nod mice with insulinomas implanted within Baxter immunoisolation devices. *J Mol Med* 77: 219-222, 1999.
81. **Lucisano JY, Armour JC, and Gough DA.** In vitro stability of an oxygen sensor. *Anal Chem* 59: 736-739, 1987.
82. **Lucisano JY and Gough DA.** Transient response of the two-dimensional glucose sensor. *Anal Chem* 60: 1272-1281, 1988.
83. **Maddox PH and Jenkins D.** 3-Aminopropyltriethoxysilane (APES): a new advance in section adhesion. *J Clin Pathol* 40: 1256-1257, 1987.

84. **Makale MT, Chen PC, and Gough DA.** Variants of the tissue-sensor array window chamber. *Am J Physiol Heart Circ Physiol* 289: H57-65, 2005.
85. **Makale MT, Jablecki MC, and Gough DA.** Mass transfer and gas-phase calibration of implanted oxygen sensors. *Anal Chem* 76: 1773-1777, 2004.
86. **Makale MT, Lin JT, Calou RE, Tsai AG, Chen PC, and Gough DA.** Tissue window chamber system for validation of implanted oxygen sensors. *Am J Physiol Heart Circ Physiol* 284: H2288-2294, 2003.
87. **Manoonkitiwongsa PS, Jackson-Friedman C, McMillan PJ, Schultz RL, and Lyden PD.** Angiogenesis after stroke is correlated with increased numbers of macrophages: the clean-up hypothesis. *J Cereb Blood Flow Metab* 21: 1223-1231, 2001.
88. **Marchant R, Hiltner A, Hamlin C, Rabinovitch A, Slobodkin R, and Anderson JM.** In vivo biocompatibility studies. I. The cage implant system and a biodegradable hydrogel. *J Biomed Mater Res* 17: 301-325, 1983.
89. **Marchant RE.** The cage implant system for determining in vivo biocompatibility of medical device materials. *Fundam Appl Toxicol* 13: 217-227, 1989.
90. **Melamed-Frank M, Lache O, Enav BI, Szafrank T, Levy NS, Ricklis RM, and Levy AP.** Structure-function analysis of the antioxidant properties of haptoglobin. *Blood* 98: 3693-3698, 2001.
91. **Meng H, Bentley TB, and Pittman RN.** Myoglobin content of hamster skeletal muscles. *J Appl Physiol* 74: 2194-2197, 1993.
92. **Metcalfe DD, Baram D, and Mekori YA.** Mast cells. *Physiol Rev* 77: 1033-1079, 1997.
93. **Meyle J, Wolburg H, and von Recum AF.** Surface micromorphology and cellular interactions. *J Biomater Appl* 7: 362-374, 1993.
94. **Morff RJ.** Contribution of capillary recruitment to regulation of tissue oxygenation in rat cremaster muscle. *Microvasc Res* 36: 150-161, 1988.

95. **Myers MA and Fleck A.** Observations on the delay in onset of the acute phase protein response. *Br J Exp Pathol* 69: 169-176, 1988.
96. **Ohyanagi M NH, Suenage K, Tsuchida E.** Oxygen-permselectivity in new type polyorgonosiloxanes with carboxyl group on the side chain. *Polymer Bulletin* 23: 637-642, 1990.
97. **Padera RF and Colton CK.** Time course of membrane microarchitecture-driven neovascularization. *Biomaterials* 17: 277-284, 1996.
98. **Pawley JB.** *Handbook of biological confocal microscopy*. New York: Plenum Press, 1995.
99. **Pittman RN.** In vivo photometric analysis of hemoglobin. *Ann Biomed Eng* 14: 119-137, 1986.
100. **Pittman RN and Duling BR.** Measurement of percent oxyhemoglobin in the microvasculature. *J Appl Physiol* 38: 321-327, 1975.
101. **Popel AS.** Theory of oxygen transport to tissue. *Crit Rev Biomed Eng* 17: 257-321, 1989.
102. **Popel AS, Pittman RN, and Ellsworth ML.** Rate of oxygen loss from arterioles is an order of magnitude higher than expected. *Am J Physiol* 256: H921-924, 1989.
103. **Pries AR and Secomb TW.** Microvascular adaptation--regulation, coordination and function. *Z Kardiol* 89 Suppl 9: IX/117-120, 2000.
104. **Ratner BD.** Reducing capsular thickness and enhancing angiogenesis around implant drug release systems. *Journal of Controlled Release* 78: 211-218, 2002.
105. **Ratner BD.** Surface modification of polymers: chemical, biological and surface analytical challenges. *Biosens Bioelectron* 10: 797-804, 1995.
106. **Reinhold HS and van den Berg-Blok A.** Factors influencing the neovascularization of experimental tumours. *Biorheology* 21: 493-501, 1984.

107. **Ridker PM, Buring JE, Shih J, Matias M, and Hennekens CH.** Prospective study of C-reactive protein and the risk of future cardiovascular events among apparently healthy women. *Circulation* 98: 731-733, 1998.
  
108. **Ridker PM, Cushman M, Stampfer MJ, Tracy RP, and Hennekens CH.** Inflammation, aspirin, and the risk of cardiovascular disease in apparently healthy men. *N Engl J Med* 336: 973-979, 1997.
  
109. **Ridker PM, Cushman M, Stampfer MJ, Tracy RP, and Hennekens CH.** Plasma concentration of C-reactive protein and risk of developing peripheral vascular disease. *Circulation* 97: 425-428, 1998.
  
110. **Ridker PM, Rifai N, Pfeffer MA, Sacks FM, Moye LA, Goldman S, Flaker GC, and Braunwald E.** Inflammation, pravastatin, and the risk of coronary events after myocardial infarction in patients with average cholesterol levels. Cholesterol and Recurrent Events (CARE) Investigators. *Circulation* 98: 839-844, 1998.
  
111. **Roitt IM and Delves PJ.** *Roitt's essential immunology*. Oxford, UK ; Malden, MA: Blackwell Science, 2001.
  
112. **Rowe IF, Soutar AK, Trayner IM, Baltz ML, de Beer FC, Walker L, Bowyer D, Herbert J, Feinstein A, and Pepys MB.** Rabbit and rat C-reactive proteins bind apolipoprotein B-containing lipoproteins. *J Exp Med* 159: 604-616, 1984.
  
113. **Ryan DM.** Implanted tissue-cages: a critical evaluation of their relevance in measuring tissue concentrations of antibiotics. *Scand J Infect Dis Suppl*: 58-62, 1978.
  
114. **Ryan DM and Mason U.** Antibiotic tissue levels: are tissue cages relevant for their measurement? *J Antimicrob Chemother* 5: 116-118, 1979.
  
115. **Saldivar E, Cabrales P, Tsai AG, and Intaglietta M.** Microcirculatory changes during chronic adaptation to hypoxia. *Am J Physiol Heart Circ Physiol* 285: H2064-2071, 2003.
  
116. **Sandison JC.** A new method for the study of living growing tissues by the introduction of a transparent chamber in the rabbit's ear. *Anat Rec* 28: 281-287, 1924.
  
117. **Schmidt JA and von Recum AF.** Texturing of polymer surfaces at the cellular level. *Biomaterials* 12: 385-389, 1991.

118. **Schuurs AH and van Weemen BK.** Enzyme-immunoassay: a powerful analytical tool. *J Immunoassay* 1: 229-249, 1980.
  
119. **Secomb TW, Hsu R, Park EY, and Dewhirst MW.** Green's function methods for analysis of oxygen delivery to tissue by microvascular networks. *Ann Biomed Eng* 32: 1519-1529, 2004.
  
120. **Semenza GL.** Regulation of mammalian O<sub>2</sub> homeostasis by hypoxia-inducible factor 1. *Annu Rev Cell Dev Biol* 15: 551-578, 1999.
  
121. **Sharkawy AA, Klitzman B, Truskey GA, and Reichert WM.** Engineering the tissue which encapsulates subcutaneous implants. I. Diffusion properties. *J Biomed Mater Res* 37: 401-412, 1997.
  
122. **Sharkawy AA, Klitzman B, Truskey GA, and Reichert WM.** Engineering the tissue which encapsulates subcutaneous implants. II. Plasma-tissue exchange properties. *J Biomed Mater Res* 40: 586-597, 1998.
  
123. **Sharkawy AA, Klitzman B, Truskey GA, and Reichert WM.** Engineering the tissue which encapsulates subcutaneous implants. III. Effective tissue response times. *J Biomed Mater Res* 40: 598-605, 1998.
  
124. **Stucker M, Struk A, Altmeyer P, Herde M, Baumgartl H, and Lubbers DW.** The cutaneous uptake of atmospheric oxygen contributes significantly to the oxygen supply of human dermis and epidermis. *J Physiol* 538: 985-994, 2002.
  
125. **Sullivan SM and Pittman RN.** In vitro O<sub>2</sub> uptake and histochemical fiber type of resting hamster muscles. *J Appl Physiol* 57: 246-253, 1984.
  
126. **Swain DP and Pittman RN.** Oxygen exchange in the microcirculation of hamster retractor muscle. *Am J Physiol* 256: H247-255, 1989.
  
127. **Torres Filho IP and Intaglietta M.** Microvessel PO<sub>2</sub> measurements by phosphorescence decay method. *Am J Physiol* 265: H1434-1438, 1993.
  
128. **Torres Filho IP, Kerger H, and Intaglietta M.** pO<sub>2</sub> measurements in arteriolar networks. *Microvasc Res* 51: 202-212, 1996.

129. **Tsai AG, Friesenecker B, Mazzoni MC, Kerger H, Buerk DG, Johnson PC, and Intaglietta M.** Microvascular and tissue oxygen gradients in the rat mesentery. *Proc Natl Acad Sci U S A* 95: 6590-6595, 1998.
130. **Tsai AG, Johnson PC, and Intaglietta M.** Oxygen gradients in the microcirculation. *Physiol Rev* 83: 933-963, 2003.
131. **Tse PH and Gough DA.** Transient response of an enzyme electrode sensor for glucose. *Anal Chem* 59: 2339-2344, 1987.
132. **Tyml K.** Capillary recruitment and heterogeneity of microvascular flow in skeletal muscle before and after contraction. *Microvasc Res* 32: 84-98, 1986.
133. **van Leeuwen MA and van Rijswijk MH.** Acute phase proteins in the monitoring of inflammatory disorders. *Baillieres Clin Rheumatol* 8: 531-552, 1994.
134. **Van Weemen BK and Schuurs AH.** Immunoassay using antigen-enzyme conjugates. *FEBS Lett* 15: 232-236, 1971.
135. **von Recum AF, Opitz H, and Wu E.** Collagen types I and III at the implant/tissue interface. *J Biomed Mater Res* 27: 757-761, 1993.
136. **Ward WK, Slobodzian EP, Tiekotter KL, and Wood MD.** The effect of microgeometry, implant thickness and polyurethane chemistry on the foreign body response to subcutaneous implants. *Biomaterials* 23: 4185-4192, 2002.
137. **Whicher JT and Evans SW.** *Biochemistry of inflammation*. Dordrecht ; Boston: Kluwer Academic Publishers, 1992.
138. **Williams R.** An adaptation of the transparent chamber technique to the skin of the body. *Anat Rec* 60: 493-499, 1934.
139. **Williams SK, Berman SS, and Kleinert LB.** Differential healing and neovascularization of ePTFE implants in subcutaneous versus adipose tissue. *J Biomed Mater Res* 35: 473-481, 1997.

140. **Wisniewski N, Klitzman B, Miller B, and Reichert WM.** Decreased analyte transport through implanted membranes: Differentiation of biofouling from tissue effects. *Journal of Biomedical Materials Research* 57: 513-521, 2001.
141. **Wisniewski N, Moussy F, and Reichert WM.** Characterization of implantable biosensor membrane biofouling. *Fresenius J Anal Chem* 366: 611-621, 2000.
142. **Wisniewski N and Reichert M.** Methods for reducing biosensor membrane biofouling. *Colloids Surf B Biointerfaces* 18: 197-219, 2000.
143. **Wojciak-Stothard B, Madeja Z, Korohoda W, Curtis A, and Wilkinson C.** Activation of macrophage-like cells by multiple grooved substrata. Topographical control of cell behaviour. *Cell Biol Int* 19: 485-490, 1995.
144. **Yaegashi K, Itoh T, Kosaka T, Fukushima H, and Morimoto T.** Changes in tissue oxygen distribution during acute hypoxia observed by an oxygen-sensitive membrane. *Japanese Journal of Physiology* 45: S51, 1995.
145. **Yaegashi K, Itoh T, Kosaka T, Fukushima H, and Morimoto T.** Diffusivity of oxygen in microvascular beds as determined from P-O<sub>2</sub> distribution maps. *American Journal of Physiology* 270: H1390-H1397, 1996.
146. **Yudkin JS, Stehouwer CDA, Emeis JJ, and Coppack SW.** C-reactive protein in healthy subjects: Associations with obesity, insulin resistance, and endothelial dysfunction: A potential role for cytokines originating from adipose tissue? *Arteriosclerosis Thrombosis & Vascular Biology* 19: 972-978, 1999.